A multi-reflection time-of-flight mass spectrograph for high-precision mass measurements of short-lived nuclei

Yuta Ito

February 2014

A multi-reflection time-of-flight mass spectrograph for high-precision mass measurements of short-lived nuclei

Yuta Ito

Submitted to the Graduate School of
Pure and Applied Sciences
in Partial Fulfillment of the Requirements
for the Degree of Doctor of Philosophy in
Science

at the
University of Tsukuba

Contents

List of Tables

List of Figures

Abstract

Mass measurements of unstable nuclei, providing direct measure of the nuclear binding energy, are invaluable for nuclear structure and nuclear astrophysics. For highly neutron-rich nuclei from Co to Xe, of importance for understanding both the astrophysical r-process and evolution of shell structure, and for trans-Uranium nuclei, of importance for understanding the limit of nuclear existence, the shell effect against the strong coulomb force and the unique identification during new elements search, the mass measurements require fast measurement time, small dependence between mass and the measurement time and high efficiency, due to their typically short life-times ($T_{1/2} < 100$ ms), heavier masses and low production yields.

So far, high-precision mass measurements, typically defined as the order of $\delta m/m = 10^{-6}$ or less, have been performed with various techniques. Indirect mass measurements using nuclear reactions or decays, however, may not be so accurate. On the other hand, direct mass measurements using storage rings, in-flight spectrometers or Penning traps are providing high-precision masses with high accuracy. It has been sufficient for stable, relatively long-lived and high-yield nuclei, but getting shorter life-times and lower yields, the mass precisions achieved become poorer in general or even the measurements are impossible. Therefore, for a lot of important nuclei mentioned above there is no choice but to depend on theoretical mass predictions.

For such nuclei, a multi-reflection time-of-flight mass spectrograph (MRTOF) has been developed. By using a pair of electrostatic mirrors which create an energy isochronous condition, the flight path for a pulse of ions, e.g., from an ion trap, could be extended indefinitely and it's possible to achieve reasonably large resolving powers faster than could be achieved by other techniques, i.e., achieve higher resolving powers for sufficiently short-lived nuclei. In 1990 the idea of a MRTOF system was first proposed by H. Wollnik *et al.* About 10 years ago the first offline experiments were performed by Y. Ishida *et al.* in our group. Based on such efforts, the current MRTOF setup was designed with online experiments in mind.

In online experiments, as the radioactive nuclei are produced at high energies, they must be thermalized in a helium-filled gas cell to convert them to a low-energy ion beam amenable to such mass measurements. An already existent gas cell, designed by M. Wada *et al.*, for use in ion trap laser spectroscopy of Be isotopes was used to thermalize ^{8}Li ions as an initial online test of the MRTOF.

The low-energy ion beam from the gas cell is provided as continuous beam, while pulsed ion beam is essential for time-of-flight measurements with the MRTOF. For this purpose, a preparation trap system which consists of the flat trap and taper trap was developed. The trap system requires reasonably high efficiency, making sufficiently small emittance and short cooling time. The sufficiently small emittance which was confirmed by no intensity drop during reflections in the MRTOF and the short cooling time of 2 ms were achieved only with the flat tarp, while the sufficiently high efficiencies of ≈5.1% for $^{7}Li^{+}$ and ≈27% for Na^{+} were achieved with the taper trap as an auxiliary trap. In addition, the dual-trap scheme allowed an operational duty cycle of ≈100%.

In ToF measurement, reference ions are necessary to deduce the mass from the ToF. Basically, highly-accurate mass measurements can be performed using isobaric reference ions which have the same number of laps as the ion of interest. To provide such ions, an electrospray ionization (ESI) ion source combined with an rf-carpet was developed. By using the ESI, isobaric molecular ions could be provided over a wide variety of mass numbers and the system can be connected efficiently between the atmosphere and the vacuum with small gas-flow conductance by rf-carpet. The ESI ion source can be a powerful reference source, especially for mass measurements of trans-Uranium nuclei which have no stable elements. By combining with the MRTOF, molecular ions up to 245 u were identified and most of them have isobaric molecules.

Conventionally, it is considered that at least two known reference ions are necessary to deduce the

mass of unknown species, due to the existence of unknown ToF offset. In online experiments, however, by measuring the ToF offset directly from the trap ejection noise, the masses were deduced by the single-reference method. Actually, the masses of ^{8}Li and stable species of ^{7}Li and ^{9}Be were deduced using only ^{12}C as a reference. Taking into account the ToF drift due to the voltage fluctuations and the titanium expansion, the mass excess of ^{8}Li was found to be $\Delta = 20945.8(27)(34)$ keV with the deviation from the literature value $\Delta m = -0.04(267)(341)$ keV, corresponding to a $\delta m/m_{\rm stat} = 3.6 \times 10^{-7}$.

The obtained mass precision is competitive with Penning traps and better than storage rings and in-flight spectrometers, and scaling to heavier mass, the MRTOF could achieve similar mass precision with an order of magnitude less measurement time. The achieved measurement time on the order of 10 ms can cover a large fraction of nuclei related to r-process, pronounced nuclear shell effect and trans-Uranium elements.

Based on these developments and the success of online experiments, two MRTOF projects are now ongoing at RIKEN: mass measurements of trans-Uranium nuclei and of r-process nuclei. We hope that with mass measurements with the MRTOF over the wide region from light to superheavy, one can drastically extend the mass information, and understand nuclear structures and astrophysical process in detail.

1 Introduction

Precision mass measurements of short-lived, radioactive nuclei have an impact on various branches of nuclear physics, such as nuclear structure studies, the study of astrophysical nucleosynthesis, and the test of fundamental interactions.

The required mass precision for various field[1] is described in Table 1.1. Typically, for studies related to nuclear structures such as shell structures, deformations and so on, a mass precision on the order of $10^{-6} - 10^{-8}$ is required, while for studies related to astrophysics such as r-process and rp-process path, a mass precision of $10^{-6} - 10^{-7}$ is required. Nuclei associated with such fields are mostly short-lived, relatively heavy and have low production yields.

Table 1.1: Required mass precision for various fields

Category	$\delta m/m$
Chemistry: Identification of molecules	$10^{-5} - 10^{-6}$
Nuclear structure: shell, pairing	10^{-6}
Astrophysics : r-process, rp-process	$10^{-6} - 10^{-7}$
Nuclear fine structure: deformation, halo	$10^{-7} - 10^{-8}$
Nuclear mass model	10^{-6}

Possibly one of the most important recent developments in mass spectrometry of such exotic nuclei is a multi-reflection time-of-flight mass spectrograph (MRTOF). For long-lived and light nuclei, the MRTOF can provide mass resolving power better than that of a storage ring, but worse than the venerable Penning trap. However, for short-lived nuclei – typically $T_{1/2} < 100$ ms – the MRTOF provides much better mass resolving power than even the Penning trap. In this way, the MRTOF represents the future of mass spectroscopy in nuclear physics, where next generation facilities will provide ever greater access to the short-lived, neutron-rich, and superheavy portions of the nuclear chart.

1.1 Production and separation of radioactive ions

Mass spectroscopy of importance to nuclear physics, for the most part, involves measurement of radioactive nuclei. In recent years, as the properties of near-stable nuclei have been heavily studied, interest has naturally shifted towards nuclear species further from stability. The nuclei which can be produced, as well as the spectroscopic methods that can be employed, are strongly related to the production method. There are several production methods for exotic nuclei; they each possess their own specific advantages and complement one another.

For nuclear physics experiments, production and separation techniques of radioactive ions are essential. So far, several complementary techniques have been developed, each technique having unique sets of drawbacks and advantages. Up to now, more than 3000 nuclides have been produced at the various radioactive ion beam facilities worldwide, and studied at energies ranging from a ∼10 keV up to relativistic energies.

Production techniques are largely defined by the kinetic energy of the resultant nuclei, as well as the region of the table of isotopes which can be accessed. Light and medium-mass nuclei can be produced by fission induced by photons, neutrons, energetic-protons or heavy-ions and typically provided with an energy of a ∼10 keV. The facilities ISOLDE in Geneva [2] and TRIUMF in Vancouver [3] amoung others are using this production technique. For the production of heavy, superheavy, and neutron-deficient medium-mass nuclides, heavy-ion reactions near the energy of the Coulomb barrier are often

used, with resultant beam energies up to ∼10 MeV. This technique is exploited, for example, at ANL in the USA [4], GSI in Germany [5], JINR in Russia [6], LBNL in the USA [7] and RIKEN in Japan [8]. Nuclei throughout the entire range of the table of isotopes can be produced at high energies ($\gtrsim$100 MeV/A) by in-flight fragmentation and induced fission of heavy nuclei. Such a production method is employed at GSI [9] in Germany, NSCL in the USA [10], and RIKEN [11] in Japan.

In order to be useful, radioactive nuclei must be separated and supplied to experiments with reasonably high purity. Two techniques are generally used for separating the reaction products: isotope separation on-line (ISOL) [12] and in-flight separation [13].

1.1.1 ISOL

The isotope separation online (ISOL) technique uses a high-energy primary beam of protons or heavy ions at energies of 100-1000 MeV/u to bombard a thick target (up to a sim100 of g/cm^2) of heavier elements, producing large amount exotic nuclei via spallation, fission, and fragmentation [14, 15]. For the targets, different chemical compositions, such as oxides (for example CaO and MgO), carbides (for example UC_x and ThC_x), and metals (for example Ti) are used depending on the desired radioactive species. Because of the thickness, the reaction products are stopped in a target matrix or a solid catcher which is thick with respect to their range in matter.

The targets are generally maintained at high temperatures (sometimes up to 2000 K) so that the reaction products can, relatively quickly, diffuse out and pass into an ion source, where they are ionized by surface ionization, plasma ionization, or by laser ionization. The different methods employed for the ionization of the reaction products take advantage of physical or chemical properties of the different species to efficiently release and ionize the desired nuclide and heavily suppress unwanted contaminants [16].

Afterwards, the ions are accelerated to an energy of a ∼10 keV, a beam energy well-suited for low-energy experiments, such as Penning trap mass spectrometry or collinear laser spectroscopy. The accelerated beam is then focused and mass separated using a dipole magnet, typically allowing very high purity radioactive nuclear beams. Behind the mass separator, a beam line distributes the radioactive ion beam to various experiments located in an experimental hall. Very intense beams with excellent beam properties for certain elements are available, but chemical properties and decay losses in the target ultimately limit the range of secondary beams available [17] and a huge amount of isobaric contaminants are often contained which could be a serious problem for precision experiments.

Examples of ISOL-type facilities where mass measurements with ion traps have been or will be performed include ISOLDE [2, 18], TRIUMF [3], and ANL. At JYFLTRAP at Jyväskylä, Finland, such ion beams are produced by use of the ion guide ISOL system IGISOL [19]. The IGISOL technique, a forerunner of the gas cell technique to be discussed later, uses thin targets and thus avoids the release problems mentioned above; refractory elements are accessible.

1.1.2 Fusion-evaporation

Exotic nuclei can also be produced by fusion or fusion-evaporation by bombarding a thin target (∼1 mg/cm^2) with a low-to-medium energy primary beam, typically with energies of a $\sim A$ MeV. The heaviest elements are produced by fusion reactions. SHIP [5] at GSI, BGS at LBNL and GARIS at RIKEN utilize such thin targets of heavy metal – Lead, Bismuth or actinoids, such as Uranium and Americium – to produce heavy elements by fusion of the target and projectile.

A primary beam, typically neutron-rich Calcium, Argon or Neon, impinges the target. Upon colliding, a projectile and target nucleus fuse into a compound nucleus which passes through the target, exiting the far side at a ∼100 A keV. These compound nuclei are highly excited and de-excite by evaporation of some number of neutrons.

The technique can also be used to study nuclei of elements lighter than Uranium. This is done, for example, at the ATLAS facility at ANL. Light rare isotope beams are produced by fusion-evaporation using lighter projectile-target combinations, although the mechanism is unchanged.

In contrast to the ISOL technique, where ion sources and a dipole magnet are utilized for separation, recoil-separation techniques using the ionic charge and momentum of the recoiling fusion product obtained in the reaction process provide beam separation in fusion-evaporation systems. Spatial separation of the projectile and reaction products is achieved by combined electric and magnetic fields. The separation times are determined by the recoil velocities and the lengths of the separators. They are typically in the range of 1-2 microseconds. Two types of recoil separators have been developed: gas-filled separators and Wien-filter or energy separators. The gas-filled separators are employed by TASCA at GSI [20], BGS at LBNL and GARIS at RIKEN, while Wien-filter or energy separators are employed by SHIP at GSI, VASSILISSA at Dubna [21] and FMA at Argonne [4].

1.1.3 Fragmentation and in-flight fission

In the early 1970's, the process of projectile fragmentation via high-energy heavy-ion collisions, which is presently utilized in many modern radioactive beam facilities to produce secondary beams of unstable nuclei, was discovered. The projectile fragmentation process is well described by the participant-spectator model [22]. In the case of the peripheral collisions of heavy ions at collisional energies of more than several tens A MeV, only an overlapping region (participant) participates in the the inter-nucleus collision and the remaining part of the incident nucleus (spectator/fragments) passes with a velocity almost the same as the incident velocity. The momentum distribution of the fragments, both in their longitudinal and transverse components along the incident velocity, are of nearly spherically symmetric Gaussian shape with a narrow width in the projectile rest frame. The narrow velocity distribution allows magnetic analysis to separate the unstable isotopes easily.

Thus projectile fragmentation is a powerful and fast method of rare isotope production, wherein heavy-ion beams impinge on a light, thin target with a thickness of $\sim$1 g/cm^2. Upon striking the target, projectile nuclei shatter in a semi-combinatorial fashion. In this way, nuclei can be produced with any numbers of neutrons and protons less than those of the projectile nucleus. Similarly, if a Uranium primary beam is used, the Uranium nucleus can become excited by passing near to a nucleus in the target, inducing a fission event. The resulting fission products tend toward the neutron-rich nuclei.

Due to the kinematics of the reaction, the fragments are mainly emitted in the forward direction and can be time-tagged. After a suitable drift time, they can be identified by their time-of-flight as well as via standard energy-loss techniques, since the energy loss of atomic ions passing through matter, ΔE, depends on Z^2, while the total energy (derived from time of flight) is a function of A.

Typically, in-flight fragmentation and fission facilities employ not just identification, but also purification. This is accomplished by use of dipole magnets and wedged degraders. The magnetic rigidity, $B\rho$, of an ion is a function of the product of its forward kinetic energy and A/q. After passing through a dipole magnet, ions with higher $B\rho$ will undergo less bending than those with lower $B\rho$, providing some spatial separation. Using a wedge-shaped degrader between subsequent dipole magnets amplifies the spatial separation as it can provide energy loss $\Delta E(B\rho)$. By inserting a slit after the second dipole, most unwanted nuclei can be rejected. The flight time between the production target and the exit of the separator is only on the order of microseconds, enabling rough mass measurements of extremely short-lived nuclides. Facilities employing this technique include, for example, FRS at GSI [9] in Germany, A1900 at NSCL [10] in the USA, and RIPS and BigRIPS at RIKEN [23] in Japan. Among these, only BigRIPS is a next-generation separator with upgraded features, characterized by larger acceptance and a two-stage separator scheme.

The benefits of the fragmentation or in-flight fission with in-flight separation method are manyfold: it produces fragments lighter than the projectile with no dependence on chemical properties; there are no delay times associated with diffusion out of a target, making even the shortest-lived nuclei available. However, the resulting fragmentation beam still possesses a majority of the energy of the original primary beam. Such high-energy beams are good for nuclear excitation and reaction studies, but not so well-suited for precision mass measurements.

In-flight fragmentation and fission is the primary method employed at RIKEN. As such, techniques to convert the energetic beam to a low-energy beam, amenable to ion trap techniques, have been

developed in the recent past.

1.2 Gas catchers

Gas catchers, variously referred to as gas cells or gas-filled ion guides, were first used in the IGISOL method at JYFL [24] to produce exotic nuclei using a light primary beam to bombard a thin target located within a small gas cell. The reaction products exit the target and are thermalized in the helium buffer gas and extracted with gas flow. While it overcame the problems associated with diffusion and re-ionization, problems, were encountered with space-charge effects by the intense primary beam injected into the gas cell.

A hybrid concept which combines in-flight separator and fragmentation techniques solves these concerns. While the desired species are transported after identification, the primary beam is eliminated by the separator; the space charge effect can thereby be minimized. The method is the centerpiece technology for converting fragmentation beams for use in ion trap-based experiments. Radioactive ions produced and separated by the in-flight techniques as described above are decelerated and thermalized in a gas catcher filled by a noble gas, typically Helium. Helium gas is often chosen as the buffer gas because it has the highest first ionization potential among chemical elements. Thus, the thermalized ions avoid neutralization due to the high ionization potential. To have a fast and efficient extraction, DC or DC+RF electric fields are used inside the gas cell to transport thermalized ions towards the exit region. The extracted low-energy beam is then sent to the high-vacuum region to perform experiments. Such systems are universal and efficient as well as fast, which is favorable for systematic measurements of rare and short-lived species.

1.3 Ion manipulation techniques for low-energy RI beam

For low-energy experiments, ion manipulation techniques (transport, accumulation, storing, and cooling) play an important role. Especially for radioactive ions, it is important to efficiently manipulate ions, since the yields are generally not so high. To manipulate low-energy ions, two- or three-dimensional spatial confinement is required. In order to achieve such spatial confinement, a potential minimum is necessary. In many cases, it is most desirable to have a confining force that causes simple harmonic motion of the confined particle, *i.e.*, one that is proportional to the distance of the particle from the center of confinement. Since Earnshaw's theorem forbids the existence of a potential minimum in free-space by electrostatic potentials, two- or three-dimensional confinement is achieved only by the superposition of a homogeneous magnetic field and an electrostatic quadrupole field or a oscillatory inhomogeneous electric fields. In general, the former is called a Penning trap, while the latter is called a Paul trap.

In our experimental setup, radiofrequency trapping techniques are used for ion manipulation.

1.3.1 RF-carpet

Ions in a buffer gas of sufficient pressure will move along the electrical flux lines, due to frequent collisions with the gas, and finally strike the cathode and be lost unless special precautions are implemented. To avoid such ion loss, we use a cathode which consists of many ring electrodes between which rf voltages are applied in addition to dc potentials. The idea is that the average force due to the rf gradient field drives the ions away from the electrodes. The technique has been named the "rf carpet". Figure 1.1 shows a typical ion trajectory calculated by a microscopic collisional model using a Monte Carlo simulation for ^{8}Li ions in 146 mbar Helium gas. The rf voltage applied between neighboring electrode rings is 100 V_{0p} at 16 MHz and the superimposed dc field at the surface is 12 V/cm. The figure indicates the manner in which low energy ions are transported across the rf carpet towards the exit nozzle. In the following, we describe the properties of the rf carpet in detail, presenting two models to explain the physics of the rf-carpet.

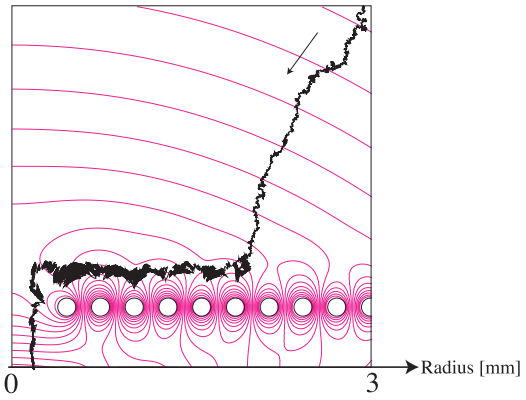

Figure 1.1: Simulated trajectory of a $^8Li^+$ ion near the rf-carpet using a Monte Carlo simulation with a microscopic collisional model [25]. The rf voltage was 190 V_{pp} at 16 MHz in 146 mbar helium gas at 300 K.

a) Analysis of the Stability Region by the Mathieu Equation

A singly charged ion with mass m in a gas moves as

$$m\ddot{\boldsymbol{r}} + \frac{e}{\mu}\dot{\boldsymbol{r}} = -e\nabla\Phi(\boldsymbol{r}, t) \tag{1.1}$$

where $\mu = \mu_0 P_0/P$ is the mobility of the ion, P_0 is the atmospheric pressure (101.325 kPa), μ_0 is the ion mobility at a pressure of P_0, and Φ is the electric potential. In Eq. 1.1, $e\dot{\boldsymbol{r}}/\mu$ represents a velocity and $-e\nabla\Phi(\boldsymbol{r}, t)$ is the driving term. Using the velocity relaxation time $\tau_v = \mu m/e$, Eq. (1.1) can be written as

$$\ddot{\boldsymbol{r}} + \frac{1}{\tau_v}\dot{\boldsymbol{r}} + \frac{e}{m}\nabla\Phi(\boldsymbol{r}, t) = 0. \tag{1.2}$$

The inhomogeneous electric field produced by electrodes of an rf carpet can be approximated to be a quadrupole field by introducing imaginary electrodes [26]. This approximation allows us to perform analytical calculations because only the regions near the rf carpet are concerned. Here the quadrupole potential Φ can be asymptotically expressed as

$$\Phi(x, y, z, t) = \Phi_0(t)\phi(x, y, z) = \Phi_0(t)\frac{x^2 - y^2}{2r_0^2} \tag{1.3}$$

where $\Phi_0(t) = U - V\cos\Omega t$. In such a field, Eq. 1.2 is given by

$$\begin{pmatrix}\ddot{x}\\ \ddot{y}\\ \ddot{z}\end{pmatrix} + \frac{1}{\tau_v}\begin{pmatrix}\dot{x}\\ \dot{y}\\ \dot{z}\end{pmatrix} + \frac{e}{mr_0^2}(U - V\cos\Omega t)\begin{pmatrix}x\\ -y\\ 0\end{pmatrix} = 0 \tag{1.4}$$

If we substitute

$$\tau = \frac{\Omega t}{2}, \qquad p = \frac{1}{\tau_v\Omega}, \qquad a_x = -a_y = \frac{4eU}{mr_0^2\Omega^2}, \qquad q_x = -q_y = \frac{2eV}{mr_0^2\Omega^2} \tag{1.5}$$

Eq. (1.4) becomes

$$\frac{\mathrm{d}^2u}{\mathrm{d}\tau^2} + 2p\frac{\mathrm{d}u}{\mathrm{d}\tau} + (a_u - 2q_u\cos 2\tau)u = 0 \tag{1.6}$$

where u indicates x or y. Substituting $w\exp(-p\tau)$ for u leads to

$$\frac{\mathrm{d}w}{\mathrm{d}\tau} + \left[(a - p^2) - 2q\cos 2\tau\right] w = 0. \tag{1.7}$$

The only change between Eq. (1.7) and the standard Mathieu's differential equation is that a is replaced with $a - p^2$ to include the buffer gas damping. It is well known that solutions of the Mathieu equations are stable only for certain regions of the a-q plane (or alternatively $(a - p^2)$-q plane for Eq. (1.7)) [27]. The stable solutions describe orbits for which the ions do not strike the carpet.

b) Pseudo-potential Analysis

Using the pseud-opotential approach, the time averaged effective force of the inhomogeneous rf electric fields shall be estimated. Here we consider only the rf electric fields. The motion of the ion is replaced by a sum of the secular motion $\bar{\boldsymbol{r}}$ and the micromotion ρ as follow:

$$\boldsymbol{r} = \bar{\boldsymbol{r}} + \rho(t) = \bar{\boldsymbol{r}} + C\boldsymbol{E}_{\mathrm{rf}}(\boldsymbol{r})\cos(\Omega t + \beta) \tag{1.8}$$

where $\bar{\boldsymbol{r}}$ is assumed to be constant over a period of the rf oscillation of the high frequency Ω. Substituting Eq. (1.8) into Eq. (1.2), where $-\nabla\Phi = -\nabla\Phi\cos\Omega t = \boldsymbol{E}_{\mathrm{rf}}(\boldsymbol{r})\cos\Omega t$ and C is the constant defined bt

$$\boldsymbol{\rho}(t) = -\frac{e}{m\Omega^2}\sqrt{1 + 1/\tau^2\Omega^2}\boldsymbol{E}_{\mathrm{rf}}(\boldsymbol{r})\cos(\Omega t + \beta), \qquad \tan\beta = \frac{1}{\tau_v\beta} \tag{1.9}$$

yields the time averaged force $\bar{\boldsymbol{F}}$ due to the rf electric fields as

$$\bar{\boldsymbol{F}}(\bar{\boldsymbol{r}}) = e\langle \boldsymbol{E}_{\mathrm{rf}}(\bar{\boldsymbol{r}})\cos\Omega t + [\nabla\cdot\boldsymbol{E}_{\mathrm{rf}}(\boldsymbol{r})]\,\|_{\boldsymbol{r}=\bar{\boldsymbol{r}}}(\cos\Omega t)\boldsymbol{\rho}(t)\rangle_{\text{time average}} \tag{1.10}$$

$$= -\nabla\boldsymbol{E}^2_{\mathrm{rf}}(\bar{\boldsymbol{r}})\frac{e^2}{4m\Omega^2(1 + 1/\tau_v^2\Omega^2)} \tag{1.11}$$

In the cases of vacuum and high pressure limits Eq. (1.11) becomes

$$\bar{\boldsymbol{F}}(\bar{\boldsymbol{r}}) = -\nabla\boldsymbol{E}^2_{\mathrm{rf}}(\bar{\boldsymbol{r}})\frac{e^2}{4m}\frac{1}{\Omega^2} \qquad \Omega\tau_v \gg 1 \text{ (vacuum)} \tag{1.12}$$

$$\bar{\boldsymbol{F}}(\bar{\boldsymbol{r}}) = -\nabla\boldsymbol{E}^2_{\mathrm{rf}}(\bar{\boldsymbol{r}})\frac{e^2}{4m}\tau_v^2 \qquad \Omega\tau_v \ll 1 \text{ (high pressure)} \tag{1.13}$$

When ϕ is a two-dimensional quadrupole potential, the time averaged force can be written as

$$\bar{\boldsymbol{F}}_{\mathrm{hp}}(\bar{\boldsymbol{r}}) = -\frac{V^2_{\mathrm{rf}}}{r_0^3}\frac{r}{r_0}\frac{e^2}{4m}\tau_v^2 = -\frac{m\mu^2}{4}\frac{V^2_{\mathrm{rf}}}{r_0^3}\frac{r}{r_0} \tag{1.14}$$

using

$$\phi = V_{\mathrm{rf}}\frac{x^2 - y^2}{2r_0^2}, \qquad \boldsymbol{E}^2_{\mathrm{rf}} = V^2_{\mathrm{rf}}\frac{r^2}{r_0^2}. \tag{1.15}$$

It is straightforward from Eq. (1.14) to see that as an ion comes closer to the electrodes (i.e. larger r) it is subjected to larger opposing forces from the electrodes; the forces are larger for heavier ions and at lower pressures. The narrow space between adjacent electrodes is very effective because $\bar{\boldsymbol{F}}_{\mathrm{hp}}(\bar{\boldsymbol{r}}) \approx 1/r_0^2$.[1] That is why we use the printed circuit board shown in Fig. 2.4 as an rf carpet.

[1] r is normalized by r_0

1.3.2 RF multi-pole ion guide

The RF multi-pole ion guide technique is frequently used for ion transport, ion trapping or mass separation. The rounded rods placed at concyclic positions at equal spaces are generally used as the electrodes, while especially for quadrupole mass separator hyperbolic shaped electrodes are sometimes used. By using RF voltage alternating in phase by π between adjacent electrodes, ions are confined within the ion guide and the ion motion is expressed as the oscillation in the pseudo-potential.

The higher multipole rf potential provides a deeper pseudo-potential and a larger capacity of ions [28], while the quadrupole rf potential is harmonic and the ion motion therefore has a characteristic frequency which is a function of the mass-to-charge ratio of the ion and the field parameters for the same given field condition; the features of mass selectivity and the finer confinement are only obtained in the quadrupole field.

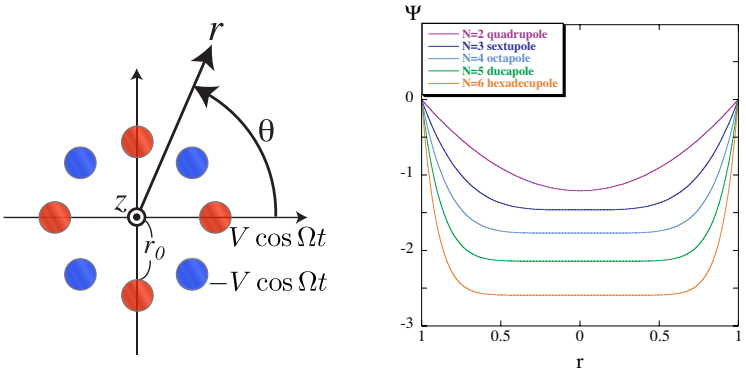

Figure 1.2: (left) Cross section of an OPIG. Definitions in the cylindrical coordinate system is also shown. (right) Pseudo-potentials of multipole fields. The higher multipole potential is deeper and more rectangular. The potential lines are plotted as a function of the relative distance from the center and the surface of the electrode is set to 0 V. The same voltage and frequency of the rf are assumed for all cases.

In the following, the properties of the mutltipole rf electric fields are briefly reviewed. The potential for a two-dimensional $2N$-pole (N is integer and $N \geq 2$) field which is formed by circular rods, uniformly distributed on a circle of radius r_0 around z-axis with an applied rf voltage $2V\cos\Omega t$ between the adjacent rods (Fig. 1.2(left)) is approximately written as

$$\Phi(r,\theta,z) = \phi\cos\Omega t \tag{1.16}$$

$$= \left(\frac{r}{r_0}\right)^N \cos(N\theta)V\cos\Omega t \tag{1.17}$$

The ions move with the pseudo-potential written as

$$\Psi_{\text{pseudo}} = \frac{eN^2}{4m\Omega^2}\left(\frac{V}{r_0}\right)^2\left(\frac{r}{r_0}\right)^{2(N-1)} \tag{1.18}$$

The shape of the pseudo potential for $N = 2$ - 6 can be plotted as shown in Fig. 1.2(right). The potential lines are plotted as a function of the relative distance from the center to the surface of the electrode set to 0 V. The same voltage and frequency of the rf electric field are assumed.

The advantage of the quadrupole rf electric field is that the potential is harmonic and that the ion motion therefore has a characteristic frequency which is a function of the mass-to-charge ratio of the ion and the field parameters. In more practical terms, the features of mass selectivity and the finer confinement are only obtained in the quadrupole field. Compared to this, higher multipole fields provide a deeper potential and a larger capacity of ions for the same given field conditions.

1.3.3 RF quadrupole ion trap and mass separator

Because the potential can be expressed by

$$\Phi(x, y, z, t) = \Phi_0(t) = (U - V\cos\omega t)\frac{x^2 - y^2}{2r_0^2} \tag{1.19}$$

the equation of motion of an ion with mass m and charge ze in the trap can be expressed by the Mathieu's equation

$$\frac{\mathrm{d}^2 u}{\mathrm{d}\tau^2} + (a_u - q_u\cos 2\tau)u = 0 \tag{1.20}$$

where u indicates x or y and

$$\tau = \frac{\Omega t}{2}, \qquad a_x = -a_y = \frac{4zeU}{mr_0^2\Omega^2}, \qquad q_x = -q_y = \frac{2zeV}{mr_0^2\Omega^2}\,. \tag{1.21}$$

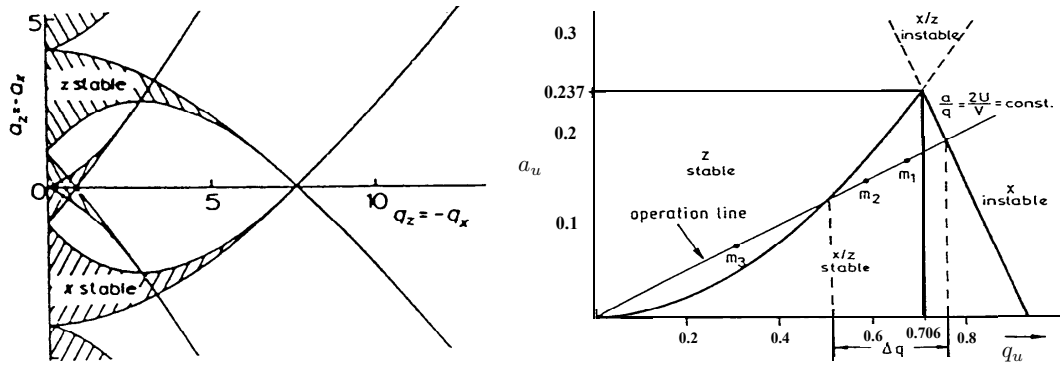

Figure 1.3: (left) The overall stability diagram for the two-dimensional quadrupole field. (right) The lowest region for simultaneous stability in x- and z-direction.

From the solution of Eq. (1.20) [27], the stable condition of the ion motion characterized by a_u and q_u are described on a_u-q_u plane as shown in Fig. 1.3(left). The stable region that contains the points $(a_u, q_u) = (0, 0)$ is often called the lowest stability region. The traps relevant for the experiments discussed here work inside this lowest stable region with $a_u \approx 0$, while when used as a quadrupole mass separator (QMS), the parameter a_u is set near the tip of the stability diagram $(a_u, q_u) = (0.237, 0.706)$. A mass range which satisfies the stable condition corresponding to m_1 and m_2 in Fig. 1.3 can pass through the QMS, otherwise the motion becomes unstable and hitting to the rods corresponding to m_1 and m_2 in Fig. 1.3.

1.4 Mass measurement techniques for exotic nuclei

Masses are one of the most important static properties of nuclei. Since the earliest measurements of Aston, it has been known that ratios of atomic masses among the various nuclei deviate slightly from integer ratios. Today, by application of Einstein's famous equation $E = mc^2$, we know this is due to the binding energy required to hold the nucleus together. Thus, by measuring atomic masses we can infer nuclear binding energies. In general, we divide the various methods used to determine atomic masses in two categories: direct measurements and indirect measurements as shown in Fig. 1.4.

1.4.1 Indirect mass measurement

Indirect mass measurements involve the determination of Q-values of nuclear reactions or radioactive decays as shown in Fig. 1.4. Various types of reactions have been used to determine masses both near

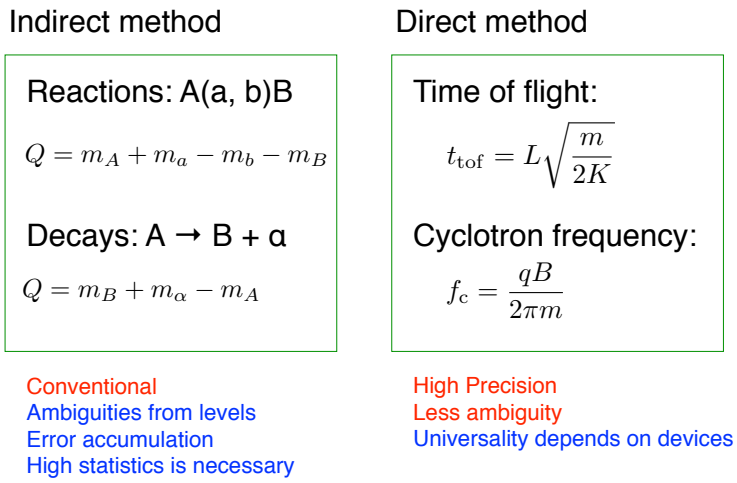

Figure 1.4: Comparison between indirect and direct mass measurements

and far from stability. With respect to the latter, reaction Q-value measurements allow for the masses of unbound nuclei to be determined.

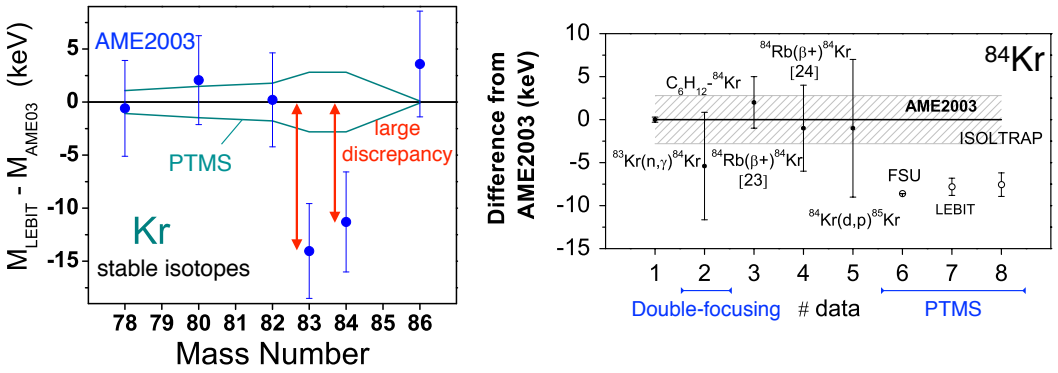

Figure 1.5: (left) Discrepancies between AME2003 [29] evaluated from indirect measurements and masses measured with the LEBIT Penning trap mass spectrometer for Kr isotopes [30]. (right) Differences from AME2003 for various mass measurements for ^{84}Kr [31]. The value of AME2003 was dominantly determined by an indirect measurements of No. 1.

The Q-value of nuclear decays provide mass differences between parent and daughter nuclei. In order to arrive at a final mass value from a decay, the unstable species must be linked to a known mass. For isotopes far from stability, the final mass determination may involve long chains of decays which can lead to the accumulation of error in the final mass value. This is particularly so in *e.g.* β-decay of nuclei with odd numbers of neutrons or protons, which often requires careful attention be paid to decays into excited states.

Similarly for using nuclear reactions, it often happens that masses determined from spectroscopy have mistaken the ground state for an excited (isomeric) state. An example of Kr isotopes is shown in Fig. 1.5. Figure 1.5(left) shows discrepancies between AME2003 [29] evaluated from indirect measurements and masses measured with the LEBIT Penning trap mass spectrometer for Kr isotopes [30]. There are large discrepancies for stable isotopes ^{83,84}Kr which are evaluated only from indirect measurements. Figure 1.5(right) shows differences from AME2003 for various mass measurements for ^{84}Kr. All indirect measurements overestimated the mass of ^{84}Kr and the mass from (n, γ) reaction has large weight for AME2003 mass evaluation. It is assumed that the excited states of ^{84}Kr were missing, therefore the mass was determined to be larger than the one measured with Penning trap mass spectrometers. As such, whenever possible, direct measurements are preferable.

1.4.2 Direct mass measurement

In the 1910's, the first direct mass measurements of atomic nuclei were performed using a spectrograph with aligned magnetic and electric fields, having ions of the same species focused on a photographic plate along parabolas, developed by Thomson. Despite the poor mass resolving power, $R \sim 20$, Neon isotopes, $A = 20$ and 22 were identified; the discovery of "isotopism" from direct observation of two different nuclides for the same element [32]. Following the discovery of isotopism, the "mass defect" was discovered by his student, Aston. For the experiments, the first mass spectrometer was developed and a mass resolving power $R = 600$ was reached. The ensemble of masses obtained by Aston were determinant in the discovery of nuclear closed shells [33].

Then, a long series of improvements followed which increased the mass resolving power (precision), mass accuracy and the sensitivity of the mass spectrographs and spectrometers. In the early 1970's R. Klapisch and C. Thibault coupled, for the first time, a classical mass spectrometer to an accelerator, the PS at CERN, to measure the masses of unstable species [34, 35]. They discovered that the magicity at $N = 20$ disappeared for Na isotopes. Around 1980, J. Kluge had the great idea to exploit the fantastic resolving power of Penning traps in order to perform atomic mass measurements. Before the end of that decade, he and his group effectively obtained masses of unstable nuclear species with unprecedented precisions [36].

In 1996 the last facility with a rare-isotope mass measurement program based on deflection-voltage measurements, Chalk River, was closed. Today, all direct mass measurements are made by employing some combination of time of flight, frequency determination, and magnetic rigidity. Several spectrographs and spectrometers exist around the world for making mass measurements of exotic nuclei at various precisions. SPEG [37], at GANIL, uses time of flight and magnetic rigidity measurements to achieve a mass resolution of $\approx 10^4$. The time-of-flight is on the order of 1 μs, and although the resolving power is relatively low, SPEG's high sensitivity has allowed it to perform measurements far from the valley of stability. TOFI [38] at LANL was designed to measure the masses of light, neutron-rich nuclei. The S800 spectrograph [39] at the NSCL also uses time of flight and magnetic rigidity for making mass measurements in a similar manner, and regime, as SPEG. For a given time resolution the overall mass resolution is limited by the total time of flight of the ions.

In an effort to improve the mass resolving power two approaches have been made. The first is to use cyclotrons to prolong the time of flight. In the case of the CSS2 [40] cyclotron, at GANIL, projectile fragments are injected into the cyclotron and radiofrequency fields are applied to accelerate species with a certain mass-over-charge value. The arrival time of the ion at a detector inside of the cyclotron is measured as a function of the phase of the radiofrequency, allowing a mass determination to be made. A similar approach [41] was used with SARA at Grenoble.

The second approach is to use a storage ring, such as the Experimental Storage Ring (ESR) at GSI. By operating in isochronous mode [42] the revolution times of ions are recorded as they travel around the ESR, using a thin-foil detection technique for the time-of-flight detection. Ions of different mass create different time-of-flight spectra which can be compared to reference mass spectra to determine a mass value. Mass resolving powers on the order of 10^5 can be achieved and the method has been employed to measure the masses of many short-lived, neutron-rich nuclides [42]. Even greater mass resolving powers can be obtained through frequency determination. Using the ESR it is possible to use cold electrons to cool the exotic nuclei as they travel around the ESR and employ the Schottky method to detect the revolution frequency of the ions [43]. This method increases the resolving power to $\approx 10^6$ and requires a few thousand ions, yet the lengthy cooling times limit the half lives to $T_{1/2} > 5$ s.

The RF spectrometer MISTRAL [44], at ISOLDE, accepts the 60 keV ISOLDE beam, imposing a two-turn helicoidal trajectory through a homogenous magnetic field. Using MISTRAL one determines the cyclotron frequency, $\nu_c = qB/(2\pi m)$, of the nuclide of interest by the application of a radiofrequency signal applied to electrodes located at the one-half and three-half turn position within the magnetic field. If the phase difference in the applied RF signals is correct then ions experience an equal but opposite deflection when passing through the second electrode structure. An incorrect phase difference will result in a net deflection and the ions will not pass through an exit slit, which allows resolving powers of greater than 10^5 to be reached.

Today, Penning trap mass spectrometry is the most precise method available for measuring stable and unstable nuclides. Relative mass precisions of $\delta m/m < 10^{-10}$ for stable species [45] and $\delta m/m < 10^{-9}$ for unstable species [46] have been observed. Penning trap mass spectrometry of unstable nuclides with half lives down to 100 ms are considered to be possible, and for instance the short-lived isotope studied so far is ^{11}Li [47] which has a half life of $T_{1/2} = 8.8$ ms.

Penning trap mass spectrometers have been installed at radioactive beam facilities around the world. The first Penning trap mass spectrometer for rare isotopes, ISOLTRAP [48], was installed at the ISOLDE facility at CERN. The low-energy, low-emittance ISOL beams are ideal for precision experiments, such as Penning trap mass spectrometry. Following ISOLTRAP's success, several Penning trap spectrometers were installed at other facilities: JYFLTRAP [49] at Jyväskylä, CPT [50] at Argonne National Lab, and SHIPTRAP [51] at GSI. Although CPT, SHIPTRAP and LEBIT [52] are installed at facilities which produce low-to-mid energy rare isotope beams, an additional step is required to thermalize the beam before it can be used for Penning trap mass spectrometry. Thermalization of the rare isotope beam is accomplished by stopping the beam in a gas cell and extracting it at low energies.

1.4.3 MRTOF

In recent years, a new type of ToF-MS, based on an electrostatic trap [53, 54, 55, 56, 57], has been pioneered. This multi-reflection time-of-flight mass spectrograph (MRTOF-MS or just MRTOF) makes use of low-energy ions, relying on a pair of electrostatic mirrors between which ions reflect, thus allowing an extremely long flight path. Thus far, such devices have been used to store ions [58], as isobar separators and for mass measurements [55, 56, 59, 57]. They are capable of achieving mass resolving powers of $R_{\mathrm{m}} > 100,000$, allowing mass precision on the order of $\delta m/m \approx 10^{-7} - 10^{-8}$ with flight times of a few milliseconds [60, 57]. They avoid the problem of microsecond isomers while enhancing the achievable resolution without requiring an excessive measurement time. As such, they represent an excellent compromise between energetic ToF-MS and PTMS.

In recent years, direct mass measurements using an MRTOF have been performed at GSI-FRS, CERN-ISOLDE and RIKEN-RIPS. These systems are in principle similar, but differ slightly in operational details. Here, each system is briefly introduced and explained.

a) MRTOF@ISOLDE

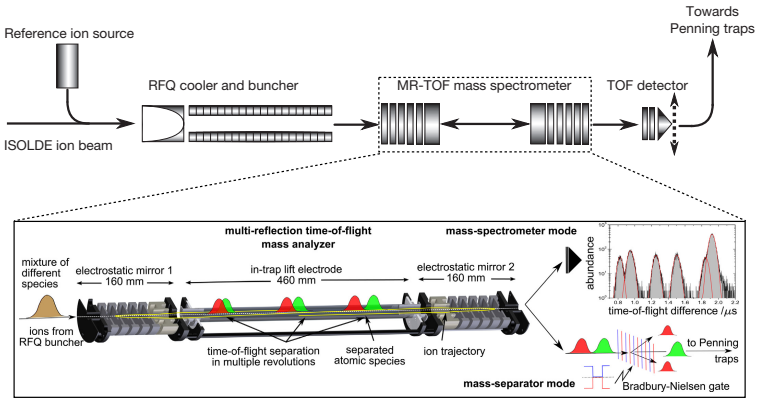

Figure 1.6: (top) Main components relevant for MRTOF mass measurements at ISOLDE: incoming ISOLDE ion beam, reference ion source, radio-frequency quadrupole (RFQ) cooler/buncher, MRTOF and (removable) time-of-flight ion detector. (bottom) Sectional view of the MRTOF. The mass-separated ions are either detected by a microchannel-plate (MCP) detector to record a time-of-flight spectrum or selected by a Bradbury-Nielsen gate.

ISOLTRAP at ISOLDE/CERN is pioneer facility for high-precision mass measurements of unstable

nuclei. The unstable nuclei are produced at the online isotope separator ISOLDE in proton-induced fission reactions within a thick uranium carbide target using intense 1.4 GeV proton beams. The target material is kept at an elevated temperature so that the radioactive atoms produced can diffuse out of the target into different dedicated ion sources. There, the atoms are ionized by several different methods: in hot plasma, on hot surface or by laser ionization. The ions are accelerated and transported to ISOLTRAP set-up via an isotope separator online (ISOL) as a continuous 30 keV beam. They are captured and cooled in the radio-frequency quadrupole (RFQ) cooler/buncher and forwarded to the MR-TOF as short-time bunches (see Fig. 1.6(top)).

For sufficiently long-lived species and low contaminant cases, high-precision mass measurements are performed with a Penning trap located after the MRTOF. In that case, the MRTOF is used as an isobar separator, therefore the time-of-flight detector after the MRTOF is removable and replaced by a Bradbury-Nielsen gate (BNG) (see Fig. 1.6(bottom)).

In the case of the MRTOF at ISOLDE, the drift tube potential is lifted up and down instead of switching the mirrors to store ions in or eject ions from the MRTOF. The potential lift method is electrically easier and the mirror potential where ions turn around can be calmer than the mirror switching method. The field penetration to the drift region is, however, created from both mirrors, therefore the effective mass band-width become much smaller than the mirror switching method when ions are injected and ejected. This method is not suitable for wide mass band-width measurements such as combined with an in-flight separator, but sufficient for narrow mass band-width (or isobaric) measurements such as combined with an ISOL technique.

Recently, the MRTOF at ISOLDE has been used for online mass measurements of neutron-rich calcium isotopes. In the case of ^{51,52}Ca, the MRTOF was operated as an isobar separator, delivering the purified bunches to the Penning traps. However, for ^{53,54}Ca the Penning-trap measurements were not possible because of the low production rates, short life-times and copious isobaric contamination. For example, only a few ^{54}Ca ions per minute were detected behind the MRTOF system, accompanied by several thousand contaminating ^{54}Cr ions. The rate of delivery of ^{54}Ca to the Penning traps was considerably reduced owing to the lower transport efficiency and the decay losses caused by the required extra ion trapping time. Thus for ^{53,54}Ca the MRTOF device itself was employed as a mass spectrometer. In the experiments, the masses of ^{53,54}Ca were deduced by a conventional calibration method, *i.e.*, ^{39}K and ^{53,54}Cr were used as references. The mass of ^{52}Ca deduced from the MRTOF was consistent with the one deduced from the Penning trap, and the masses of ^{53,54}Ca were determined from the MRTOF for the first time with a mass precision of $\delta m/m \approx 10^{-6}$. The measured masses unambiguously establish a prominent shell closure at neutron number $N = 32$, in excellent agreement with theoretical calculations.

b) MRTOF@GSI

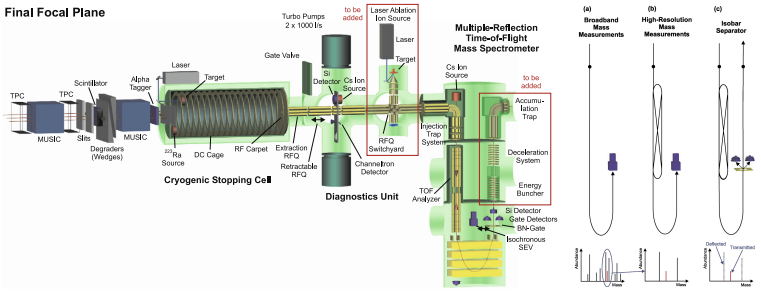

Figure 1.7: Schematic view of the setup of the cryogenic stopping cell, the RFQ beam line and the MRTOF. Components that will be added in the future are highlighted using red frames.

The MRTOF at GSI is coupled with a cryogenic stopping cell (CSC) operated at a helium gas pressure of 100 mbar and a temperature of 90 K after the FRS in-flight separator. The unstable nuclei are produced by projectile fragmentation of a ^{238}U primary beam at an energy of 1 A GeV impinging

a Be target. The projectile fragments are separated, range-bunched in the FRS, injected into the CSC and thermalized. A DC field created by a DC cage with ring electrodes throughout the length of the cell drags the ions towards the exit side of the CSC. There, an RF carpet with an electrode pitch of 0.25 mm creates a repulsive force with a DC potential gradient to guide the ions radially towards the exit hole. Once the ions reach the exit hole, the gas flow drags them out off the CSC. The extracted ions are transported by an RFQ ion guide system, which allows for differential pumping in the vicinity of the CSC and for ion beam cooling, transport, bunching, beam monitoring and mass separation (see Fig. 1.7).

The ions transported through the beam line above are accumulated and cooled further in the triple-stage injection trap system. The injection scheme to the MRTOF is similar to the one used for ISOLDE, *i.e.*, the ions are prepared by a conventional segmented Paul trap and ejected axially. The MRTOF at GSI employs a mirror switching method different from the one at ISOLDE. In addition to the two cylindrical mirrors in the MRTOF, it has a post-reflector after the ejection mirror (see Fig. 1.7). This configuration allows the MRTOF a wide-band mass spectrometry with a mass resolving power of $\Delta m/m > 10^4$ and compact vertical setup for future applications using purified beam. A time-of-flight detector is located after the post-reflector and the detector can be replaced with a BNG for isobar separation.

Recently, they also performed an online commissioning with heavy α emitting nuclei. The successful extraction of ^{213}Rn, ^{218}Rn and ^{221}Ac with half-lives of 19.5 ms, 35 ms and 52 ms, respectively, demonstrates the access to very short-lived nuclei using a combination of an in-flight separator and a gas catcher system. It is quite difficult to access such short-lived nuclei with ISOL techniques such as ISOLDE described above due to the restriction of the RI production process. Therefore, the combination of the MRTOF with a gas catcher system is the best choice to achieve high-precision mass measurements of short-lived nuclei. For the first time, time-of-flight measurements were performed on heavy projectile fragments, ^{211}Po, ^{211}Rn and ^{213}Rn, using an MRTOF. The data analysis of the experiments is still underway, therefore no details can be presented here.

c) MRTOF@RIKEN

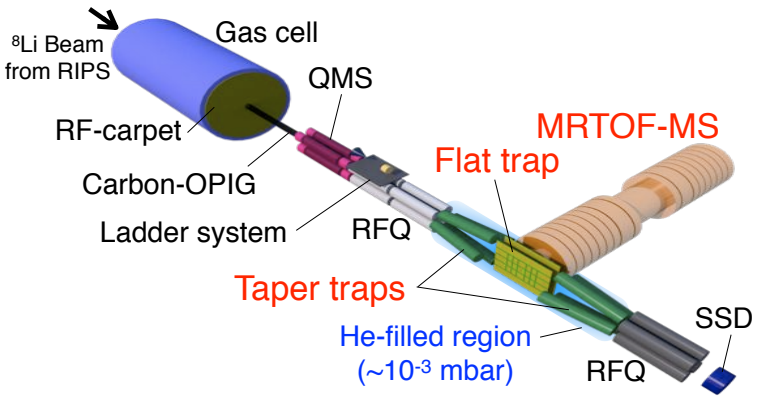

Figure 1.8: Schematic view of the MRTOF at RIKEN for online mass measurements.

RIKEN, Japan's premiere research facility, provides multiple sources of radioactive ion beams (RIB). The BigRIPS [23] in-flight separator at the RIBF is capable of providing nuclei along or near the r-process pathway. Yields exceeding several hundred per hour are expected for many of these nuclei [61]. Additionally, the GARIS separator coupled with a high-intensity linear accelerator for SHE studies via heavy-ion fusion is available at RIKEN. It can provide reasonable yields for a great many trans-uranium nuclei.

The MRTOF at RIKEN is coupled with an in-flight separator and a gas catcher system (see Fig. 1.8). Efficient conversion of these energetic RIB to low energy beams can be achieved with proven gas cell techniques [62, 63] and allow the MRTOF to be used with these RIB. The gas catcher originally

developed at RIKEN consists of a DC cage to drag the ions towards the exit side and an RF carpet creates a repulsive force with a DC potential gradient to perform efficiently extraction from the gas cell. The ions extracted from the gas cell are efficiently transported by an RFQ ion guide system to a preparation trap system. The preparation trap for ion injection to the MRTOF has a novel structure different from a conventional segmented Paul trap system employed at ISOLDE and GSI. The trap consists of a pair of printed circuit boards and therefore is possible to create a pure dipole ejection field which allows creation of a lower emittance beam than the conventional system. Therefore, there is no intensity reduction after multiple reflections in the MRTOF, while the intensity drop is observed to be 30-40% after several reflections due to emittance selection in the MRTOF at ISOLDE and GSI. Additionally, the flat trap structure allows independent injection from both sides, gas cell side or opposite, and a reference ion source can be installed at the opposite side. The MRTOF at RIKEN is dedicated to high-precision mass measurements for now and has only a time-of-flight detector after the MRTOF. After multiple reflections in the MRTOF, the ions are simply ejected to the detector.

Recently, an online mass measurements of unstable ^{8}Li were performed combined with a gas catcher system. The details are described below, but note that this is the first online mass measurement with MRTOF coupled with an in-flight separator and in the analysis, so-called single-reference method was first adopted for high-precision time-of-flight mass spectrometry. In the analysis, only one reference ion was used to deduce the mass of ^{8}Li. The method allowed higher mass precision and easier compensation of ToF drift during the experiments.

Herein we describe the details of the design and performance of the MRTOF, our motivations for using it for r-process and SHE nuclei and the results we anticipate for such future experiments.

1.5 Comparisons with various mass measurement techniques

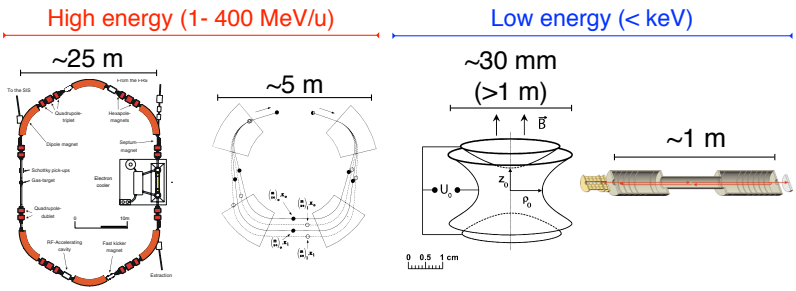

Device	Storage ring (SR) *ESR@GSI* *CSR@Lanchou*		In-flight spec. *SPEG@GANIL* *TOFI@Los Alamos* ...	Penning trap (PTMS) *ISOLTRAP@ISOLDE* *SHIPTRAP@GSI* ...	MRTOF *@RIKEN* *@ISOLDE* *@GSI*
Cost	$ 50M		$ 10M	$ 2M	$ 0.3M
Method	IMS	e-CSMS			
	ToF	ω	ToF-Bρ	ω_c	ToF
Mass resolving power	~10^5	~10^6	~10^4	>10^6	>10^5
Mass precision	~10^{-6}	~10^{-7}	~10^{-5}	<10^{-7}	<10^{-6}
Half-life	10 μs	>1 s	1 μs	≥100 ms	<10 ms
Drawbacks	calibrants e-cooling time (e-CSMS) field optimization (IMS)		μs-isomer calibration	meas. time single-ion meas.	stabilization

Figure 1.9: Comparisons with various direct mass measurement techniques

As described above, various mass measurement techniques exist. In this section, the MRTOF is compared with three other major techniques: the storage ring, the in-flight spectrometer and the Penning trap.

Figure 1.9 shows the comparisons with respect to various figures of merit. The devices are roughly categorized based on energy ranges of beam. For higher beam energy, the size of the device has to be

larger (>5 m) due to the higher magnetic rigidity ($B\rho$). On the other hand, for lower beam energy, the size of the devices can be much smaller (<1 m) as the ions can be confined with electric potentials. The MRTOF is the second smallest. However a functional Penning trap system is similar to the MRTOF in size when their superconducting magnet and cryostat are included.. Additionally the MRTOF is the only portable device, which means the measurable region does not depend on the ion sources.

As the size gets larger, the construction cost also increases. Note that while the Penning trap itself is small, an expensive superconducting magnet is necessary for the operation. Therefore, the full cost of the MRTOF is smallest, only \$0.3 M for overall system.

The measurement methods differ. However, there is a rough relation between their methods and the achievable mass resolving power and mass precision. Except for the in-flight mass spectrometer, the measurement is performed with ion trapping or storage. For frequency measurements such as Schottky mass spectrometry mode with electron cooling in the storage ring (e-CSMS), which measures revolution frequency, and ToF-ICR mode of the Penning trap, which measures cyclotron frequency, it takes a relatively long time to get more than 10^6 mass resolving power, while for ToF measurements such as an isochronous mass spectrometry mode of the storage ring (IMS), which measures ToF for every revolution, and the MRTOF, which measures total ToF after multiple reflections, it takes a relatively short time and sufficiently high mass resolving power.

A comparison of the sensitivity or the minimum number of ions is valuable for the measurement of rare isotopes. The sensitivity of the in-flight spectrometer should be more than 10^{-1} ions per second due to the need for calibration of the magnetic field. The Penning trap requires a total count of more than 10^2, otherwise the fitting of the resonance curve can fail. In the case of the storage ring, the measurement can be done by single ions with both methods, in principle. Calibration, however, is necessary and the calibrants are not always detected simultaneously. Eventually, the mass accuracies could be worse. While due to the MRTOF being a low-energy device, the calibration is much easier. Therefore the realistic sensitivity confirmed so far is less than one ion per hour and in principle much lower.

As a conclusion of this comparison, despite the MRTOF having the least construction cost (\$0.3 M) and being a portable system (∼1 m), it has a sufficiently high resolving power (>10^5) and precision (<10^{-6}), the measurement time is short enough (<10 ms) to accept the most exotic nuclei which can be produced with current existing facilities, and the sensitivity is reasonably high ($\ll$1 /s) to measure rare species.

1.6 Research goals and strategy

So far, the MRTOF was studied with offline ion source [54, 64] and the prototype-SLOWRI system (the gas cell, the rf carpet and the OPIG) [25, 62, 26, 63]. The goal of the developments in this study, described in the following sections, is to implement the measurement online with unstable nuclei which includes,

1. developing the MRTOF preparation trap with sufficiently short cooling time and high efficiency (Sec. 3.1-3.3)
2. optimization of the parameters to get a mass resolving power of $R_\mathrm{m} > 10^5$ with the trap(Sec. 3.4)
3. building associated devices, an ion transport line, a quadrupole mass separator and reference ion source for calibration(Sec. 3.5)
4. confirming the overall system online(Sec. 4.1-4.2)
5. establishing an analysis method of the MRTOF mass measurement(Sec. 4.3)

This is the first challenge to apply an MRTOF for precision mass measurement of unstable nuclei coupled with a fragment separator and a gas cell techniques.

2 Experimental setup

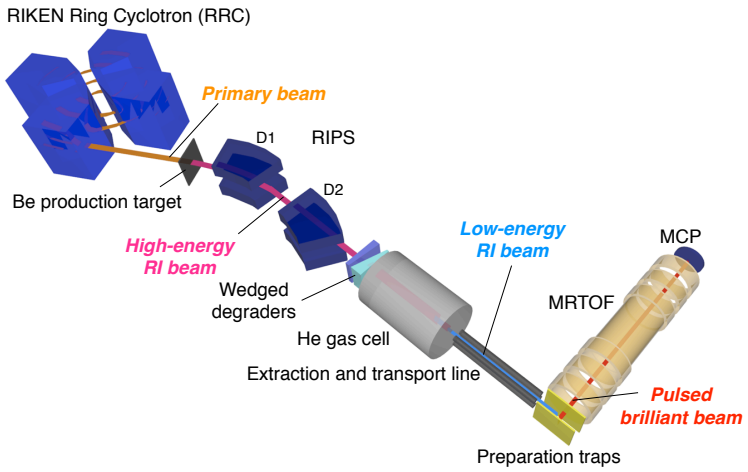

Figure 2.1: A schematic overview of our experimental setup

A schematic overview of our experimental setup is shown in Fig. 2.1. The experimental procedure was carried out in the following steps:

1. Production of RI beams via fragmentation reactions by bombarding a thin Be production target with primary beam
2. Separation of RI beams by A/Z using the first dipole magnet (D1) of the RIKEN projectile fragment separator (RIPS)
3. Particle identification of the beam passing through the second dipole magnet (D2) of RIPS
4. Conversion to low-energy beam
    a) Energy degrading and compression of the beam
    b) Deceleration and thermalization in a helium gas cell
    c) Transport within and extraction from the gas cell via an rf-carpet technique
5. Transport of the low-energy beam through differential pumping and into high-vacuum using an rf octupole ion beam guide (carbon-OPIG) made from carbon reinforced polymer rods
6. Selection of desired A/q by rf quadrupole mass separator
7. Trapping in preparation traps
8. ToF measurement with MRTOF

In the following sections this system is explained in detail.

2.1 Production of high-energy RI beams

In our experiments, a ^{8}Li beam was produced by projectile fragmentation reactions. The RIKEN projectile fragment separator (RIPS) [11] was used to separate fragments. Figure 2.2 shows a schematic

layout of RIPS. In the case of fully stripped ions, the first dipole magnet D1 provides a selection in terms of magnetic rigidity $B\rho$ [65] as, relativistically,

$$B\rho = 0.1439\frac{A}{Z}\sqrt{E\left(1+\frac{E}{2m_{\mathrm{u}}}\right)} \tag{2.1}$$

where A is the mass number of a projectile fragment, Z is the atomic number of the projectile fragment, E is the kinetic energy of the projectile fragment in A MeV, m_{u} is the atomic mass unit in MeV/c^2, namely, $m_{\mathrm{u}} = 931.494043(80)$ MeV/c^2. Through $B\rho$ analysis via the D1 magnet, projectile fragments can be separated in A/Z due to the nearly uniform velocities of the various fragments. Although the full RIPS system can provide selection of any desired A and Z independently, by utilizing a second dipole magnet (D2) in conjunction with an energy degrader, only D1 in the upstream part of RIPS was used in our experiment. To minimize problems from intense contaminants of unwanted secondary beams with A/Z similar to our desired beam, we could use a mono-energetic degrader system, which will be discussed in the next section.

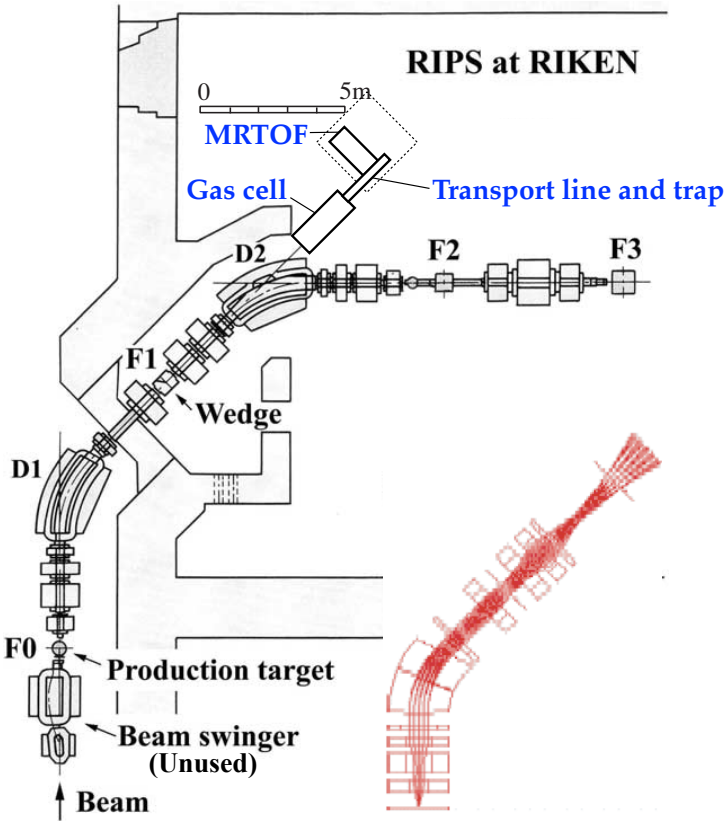

Figure 2.2: Schematic layout of the RIPS separator at RIKEN and the location of our experimental setup. Inserted red image shows a beam envelope in the horizontal plane.

The unstable nucleus of interest, ^{8}Li, was produced in the projectile fragmentation reaction of a 100 A MeV ^{13}C beam, provided by the RIKEN ring cyclotron (RRC), impinging a thin Be production target. The reaction produces a so-called "cocktail beam" containing many isotopes. Because of this, RIPS was needed for particle identification (PI) and to separate our desired species from the rest of the cocktail.

Performing PI required the following quantities:

- ΔE: energy deposited in the scintillator $\propto Z^2/v^2$
- ToF: time difference between rf signal from the RRC and the scintillator signal $\propto 1/v$

- $B\rho$: magnetic field strength of D1 $\propto (A/Z)v$ (non-relativistic)

When $B\rho \propto (A/Z)v$ is constant, $\Delta E \propto A^2$ and $TOF \propto A/Z$. Particles can be identified not only from the mapping pattern but also their intensities by calculating the yield using the LISE++ [66] computer program.

TOF and ΔE signals are connected to TDC and ADC of the data acquisition system and the particles are identified by software. Meanwhile these signals are also connected to a hardware PI circuit as shown in Fig. 2.3 to produce hardware PI signals used to count the particles of interest without any dead time.

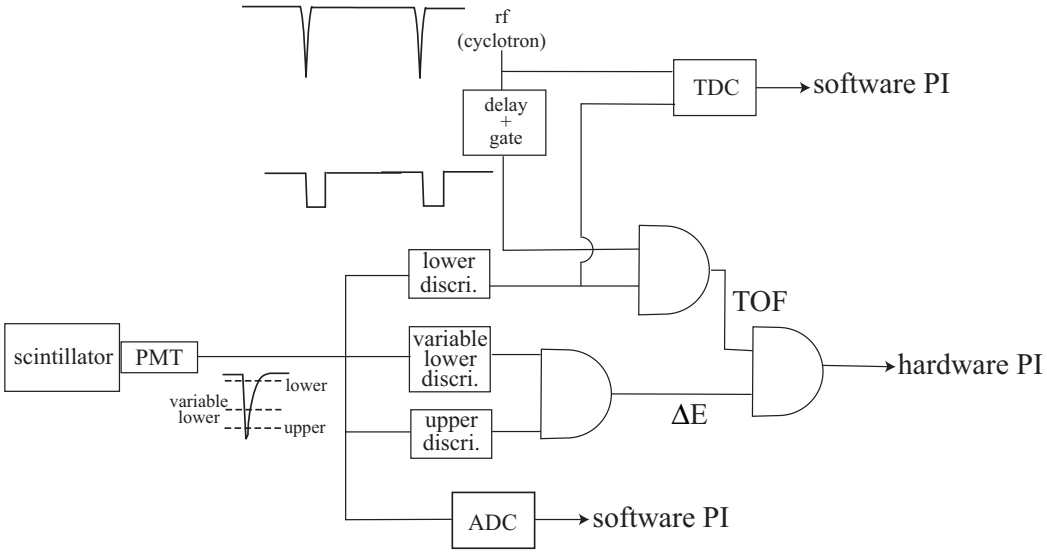

Figure 2.3: Sketch of hardware system for particle identification signals

2.2 Prototype-SLOWRI system

As previously mentioned, the energetic beams produced by the fragmentation process must be converted into low-energy beams compatible with our experimental methods. The system used to do this was the prototype for the SLOWRI low-energy RI facility currently under construction at RIBF. This prototype system comprised a 2 m-long gas cell with large rf-carpet, a differential pumping system and a carbon-reinforced polymer OPIG to transport ions extracted from the gas cell into high-vacuum.

Radioactive ions of ≈100 A MeV from RIPS are first decelerated by a wedge-shaped degrader, then injected and thermalized in a Helium gas cell. In the gas cell these slow ions are transported by dc fields towards the end of the cell. An rf carpet, which is located at the end of the cell, guide the ions to the exit nozzle using dc and rf electric fields. This system has been named an "rf ion guide". In this subsection an rf ion guide system for decelerating and efficient cooling of energetic unstable isotope beams and extraction of slow unstable isotope beams which was used for the SLOWRI prototype are described.

The wedge-shaped energy degrader is located at the energy-dispersive focal plane of the first half of RIPS where the dispersion of the momentum is -42 mm/%. If a degrader of uniform thickness was used to decelerate the beam, the energy spread of the beam after passing through the degrader would be quite large because the beam already has a momentum spread of more than 3%. Since, at the energy dispersive focal plane, the transverse position of the beam correlates with the beam energy, it is possible to reduce the energy spread by using a wedged degrader. By placing the thicker side of the wedge at the higher-energy side of the distribution, more energetic ions undergo greater energy reduction than lower-energy ions. In order to achieve optimal performance, a degrader system

in which both the effective thickness (total energy loss) and the wedge angle (energy compression) were adjustable was used [26].

2.2.1 Gas cell

A helium buffer gas to thermalize high-energy ions exiting the degrader was used because the high ionization potential of helium minimizes possible neutralization of the ions of interest. In order to stop as many ions as possible, a 2 m-long gas cell with a diameter of 400 mm was used. In the 2 m-long gas cell with a pressure of 27 mbar He, $A > 20$ ions, which have energies as high as 5 A MeV after the degrader, are stopped.

The conventional Ion Guide Isotope Separator On-Line (IGISOL) systems utilize a very small gas cell (≈10 mm-long) which can stop ions of not more than ≈10 A keV. Because the ions are delivered by the gas flow only, if a large gas cell were used in IGISOL, it would take too much time to extract the ions before RIs decay. In our system, most ions stopped in the He gas end up as singly charged ions, and therefore a static electric field can be used to transport the ions toward the extraction region of the catcher gas cell. The axial dc field is produced by electrodes on a stripe-patterned printed circuit board mounted in a Cu cylinder within the gas cell. For ion transport, a voltage divided along the length of the striped circuit board by resistors produced a drag field of up to 0.22 V/mm. Chip resistors bridged the valleys between the stripes of the printed circuit board. The printed circuit board, which was rolled into a cylinder, was attached to the inner wall of a Cu cylinder with Torr Seal®.

2.2.2 RF-carpet

The rf-carpet used for the experiments was the same one as used for Be laser spectroscopy [63]. Figure 2.4(top) shows a photograph of the rf-carpet and schematics of the circuits used for driving it. There are 160 concentric ring electrodes, each 0.14 mm wide and separated by 0.14 mm, in the inner region, *i.e.*, within a diameter of 110 mm. RF voltages are applied between adjacent ring electrodes to prevent the ions from reaching the surface of the rf carpet.

In addition, dc fields are applied to the ring electrodes to guide the ions towards the exit nozzle at the center of the rf carpet. There are 85 additional concentric ring electrodes, each 0.8 mm wide and separated by 0.2 mm in the outer region, *i.e.*, between a diameter of $110 - 290$ mm. Only dc voltages are applied to these ring electrodes to drive the ions towards the central region. Although the rf electric fields would be effective in case of high beam intensities, this RF power was saved since in the present situation, most of the ions are rather distant from the surfaces of the electrodes. Figure 2.4(bottom) shows the backside of the rf-carpet which has an rf divider circuit and a dc resistive divider with a copper cooling tube in which ethylene glycol circulates at -17 °C.

2.2.3 Carbon-OPIG

In order to transport the extracted slow RIs from the gas cell into the high vacuum region, an rf octupole ion beam guide whose rods are made of carbon fiber reinforced plastic (carbon-OPIG) was used [26]. The rod has about a 40 Ω resistance if the diameter is 1 mm and the length is 600 mm, and therefore it is quite easy to provide an axial dc potential gradient of 1 V per 600 mm with a reasonably low electric current of 0.2 A. The carbon-OPIG consists of eight circular rods uniformly distributed on a circle in the plane perpendicular to the axis of symmetry. Under the combined action of the multipole rf electric fields and the residual He buffer gas cooling, well focused ion beams with low energy and small spatial spread can be efficiently transmitted with efficient differential pumping by use of the carbon-OPIG.

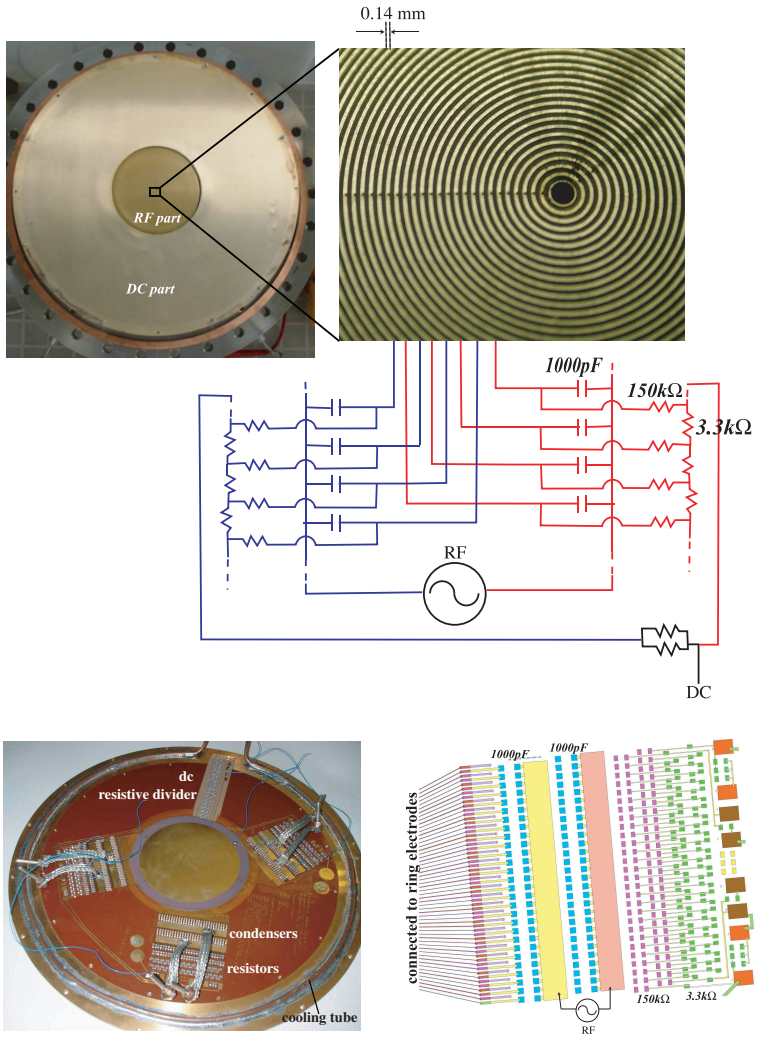

Figure 2.4: (top) Photograph of an rf carpet and schematic of rf divider circuits. (bottom) The electrical parts, dc resistive divider, capacitors and resisters, are directly mounted on the back side of the rf-carpet. The rf circuit is divided into three different sections from outer to inner to reduce each input rf power.

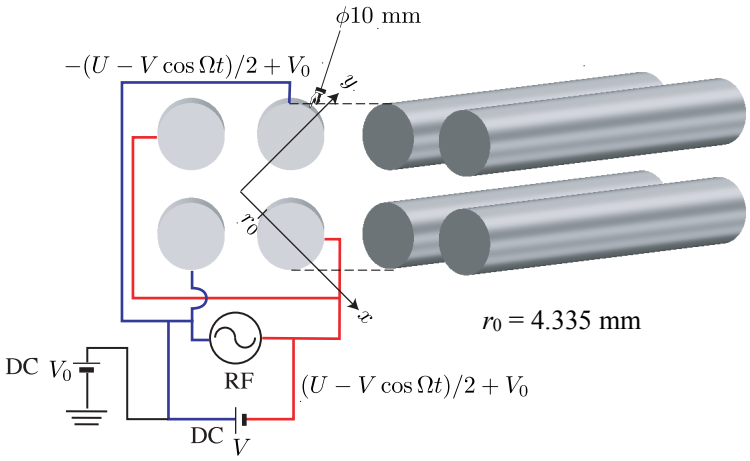

Figure 2.5: Schematic drawing of a quadrupole mass separator

2.3 Quadrupole mass separator

The rf-carpet and carbon-OPIG each have rather wide mass bandwidths. As such, stable molecular ions produced by charge exchange between Helium ions and gas impurities can be extracted from the gas cell alongside the ions of interest. An rf quadrupole mass separator (QMS) was placed after the carbon-OPIG in order to eliminate such impurity ions produced in the gas cell.

The QMS consists of 4 rounded rods of 10 mm diameter with inter-rod spacing of $r_0 = 4.335$ mm. A schematic drawing of the QMS is shown in Fig. 2.5. The QMS was typically operated with rf signals at ≈6 MHz.

2.4 Ladder system

It is useful to measure the ion rate immediately after the QMS in order to find an optimal balance between efficiency and purity. To do so, mass scans for various values of U/V must be evaluated. Typically, this would be done by installing a channel electron multiplier (CEM) after the QMS. However, particularly under online conditions, it is useful to be able to simultaneously tune the trap and other downstream components.

To accomplish such, a ladder system was installed between the QMS and the rf-quadrupole ion guide (QPIG). In the ladder system, a CEM and an alkali ion source are mounted above a small section of QPIG as shown in Fig. 2.6. They are connected to the ladder support system which can move up and down. In the up position (transmission mode), the QPIG is located on the beam axis, while in the down position (tuning mode) the CEM and ion source are located on the beam axis, with the CEM facing the gas cell and the ion source facing the downstream rf ion trap. In transmission mode, the rods of the small section of QPIG are electrically connected to those of the fixed-position QPIG.

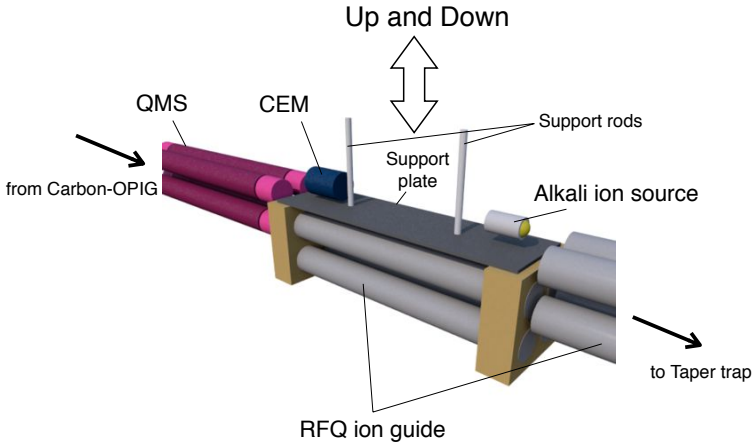

Figure 2.6: Schematic view of the ladder system. The support rods are fixed on linear motion guides. The support plate is fixed on PEEK blocks which are the support structure of the RFQ rods.

2.5 Preparation traps

In order to convert the continuous RI beam delivered by the gas cell, preparation traps filled by helium buffer gas are used. The use of gas-filled rf-multipole ion traps to accumulate and cool ions is a proven technique [67, 68, 69]. Here a brief discussion of the implementation of this technique as developed for the MRTOF is provided; a more substantial discussion has been published separately [70].

To ensure maximum system efficiency, two traps were utilized. The first trap, referred to as the "taper trap", accumulates and pre-cools ions from the continuous RI beam. Ions can be transferred

with near unity efficiency from this accumulation trap to the second trap, referred to as the "flat trap", in which the ions are further cooled prior to being orthogonally ejected and transfered to the reflection chamber.

In this way optimal ion cooling can be performed without any losses due to duty cycle. Additionally, because ions are ejected from the flat trap orthogonal to the axis of entry, the flat trap can accept ions from upstream as well as from down stream. Combined with the taper trap, this allows for interleaving measurements from online RIs and offline stable sources without loss of precious RIs or the need for any beam merging electrode system.

2.5.1 Taper trap

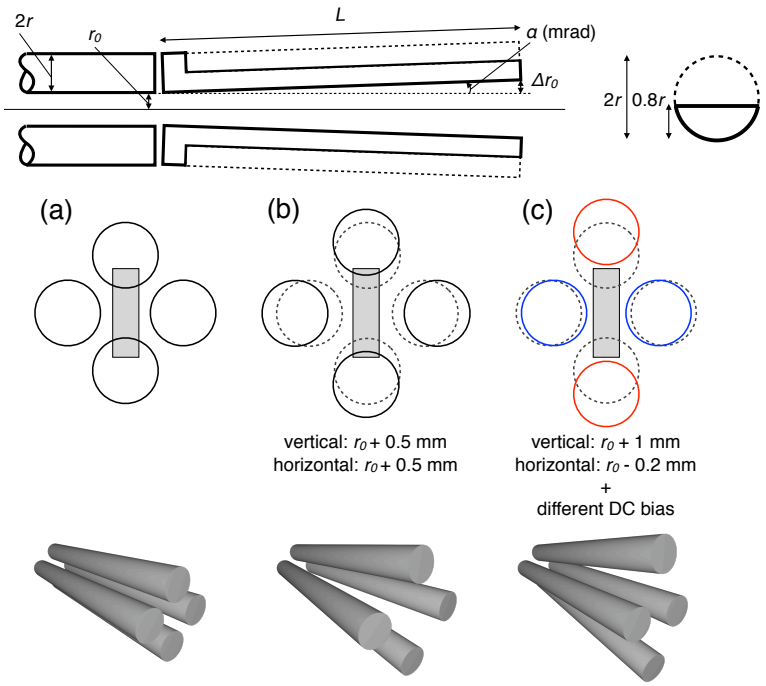

Figure 2.7: (top) Schematic view of the taper trap. In order to fit into the stainless steel tube, the rods are 4 mm thick circular segments. (bottom) Cross sectional and 3D view of the rods in three configurations: (a) the parallel trap, (b) the taper trap and (c) the asymmetric taper trap (see text). The cross sectional view of entrance side is indicated by dashed line and the flat trap aperture is indicated by rectangular gray area in bottom figures. The rods are mounted in PEEK blocks at each end.

Typically, a gas-filled RFQ consists of segmented rods [67, 68, 69]. While the axial potential configuration is flexible, the structure can be mechanically complicated and the axial potential has a stepped shape. When a low-energy continuous ion beam is slowed down by gas collisions in a segmented gas-filled RFQ, some ions could become effectively trapped in the central region of any segment if the segments are too long. Smaller segmentation requires a more complicated structure and control (*i.e.*, resistive divider, assembling, alignment, power supply, size, etc.).

In our system, both the taper trap and the flat trap, located after the taper trap, need to be filled with low-pressure helium buffer gas. The structure should be as small as possible to achieve fast cooling and produce tight ion bunches. The requisite segmented structure would be rather difficult to implement. To circumvent these mechanical difficulties, we have developed a tapered structure that can produce an effective axial drag force [71] without the usual need for segmentation of the rods. Similar structure has been used for a collision cell for molecular science using conical rods [71]. In practice, to machine the conical rods with sufficient mechanical precision to be used for an RFQ is not so easy. Thus, the tapered structure which consists of four tilted straight-rounded rods was adopted in

our study, which is simpler structure than the conical-rod structure and first applied for ion trapping purpose in this study.

The taper trap illustrated in Fig. 2.7 consists of four tilted rods with radius of $r = 5$ mm and length of $L = 190$ mm. The inter-rod-gap, r_0, at the outer end is 4.35 mm, while at the inner end it is slightly larger, $r_0 + \Delta r_0$, due to the tapered structure. The optimal Δr_0 was chosen based on SIMION [72] simulations. The taper trap is housed in a stainless steel tube to isolate it from the vacuum region outside the flat trap; a collimator at the entrance reduces the gas flow into the vacuum region.

Along the symmetry axis of any rf multipole ion guide structure, the z-component of the pseudo-potential gradient vanishes. As such, the force along the z-axis can be evaluated from the static potential. For the symmetric geometry discussed thus far, decreased field penetration from the wide side results in a net field along the z-axis. As a result, the tapered structure can produce an effective axial drag force without the usual need for segmentation of the rods.

As explained above, the strength of the effective axial drag force is determined by the slope of the taper rods. It is simplest structure, however the strength of the effective axial drag force is uncontrolled once installed. To allow for control of the strength of the drag force in the taper trap, the symmetric structure was slightly changed to be asymmetric as shown in Fig. 2.7(c) in this study. The asymmetric taper trap was developed for ion trapping for the first time in this study and drastically improved the trapping efficiency.

2.5.2 Flat trap

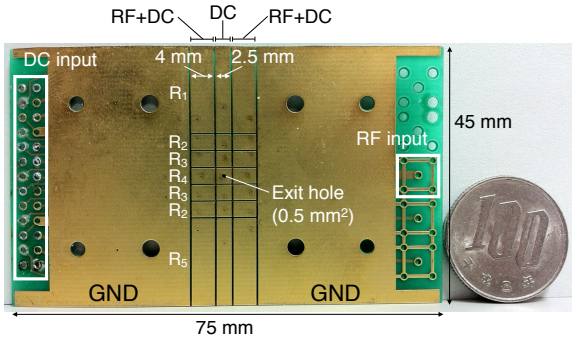

Electrode		R_1	R_2	R_3	R_4	R_5
Length (mm)		14.9	2.6	2.6	2.6	14.9
DC voltage (V)	: Accumulation*	-4.5	-5.7	-5.8	-6.0	5.0
	: Cooling	27	10.5	7.5	5.0	27

* R_1 side is the entrance in this case.

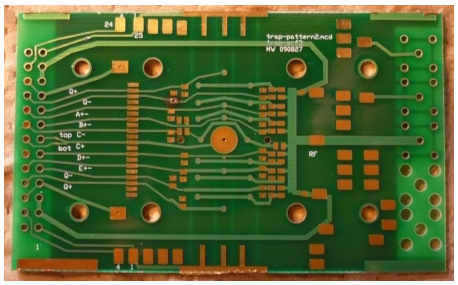

Figure 2.8: Photograph of the flat trap PCB with scales and typical dc voltages annotated. Segmented electrodes are printed on the front (left) and electrical circuit is printed on the back (right). Capacitors and resisters on the back of the PCB distribute rf and dc signals to the individual electrodes. Spacing between adjacent electrodes is 0.3 mm. A ¥100 coin is included for scale.

The flat trap is constructed using two printed circuit boards (PCB) as shown in Fig. 2.8. It operates on the same principle as a traditional segmented Paul trap, but uses a novel geometry. While a traditional Paul trap creates a well-approximated quadrupole field using four rod electrodes, our flat trap design uses six strip electrodes. While the quadrupole approximation is not sufficient for use as a mass filter, it is perfectly well-suited for ion storage and cooling.

The PCBs are mounted on an aluminum block and separated by 4 mm distance. Each PCB consists of three strips divided into 7 segments (see Fig. 2.8). The central electrode of each board has a 0.5 mm^2 plated hole at its center. By applying a potential difference between the center electrodes of the PCBs, ions can be extracted orthogonal to the injection axis through the small exit holes. DC electric potentials are used, in the standard manner, to create an axial potential well while an rf signal superimposed on the outer strips provides a radially confining pseudo-potential. By operating the

trap in rf unbalanced mode, there is no need to connect the central strip segments to an RC network, a feature which allows for very fast switching of the centermost segment. Such fast switching is used to apply a well-defined dipole field at the trap center to eject ions from the trap via the small hole in the central electrode. This ensures that the ion optical properties of the ion pulse are without higher-order optical aberrations and that the ions have a low emittance.

2.6 Reference ion sources

Any time-of-flight mass spectrometer needs mass references to derive unknown masses from ToF and, in principle, to track the ToF drift in devices for high-precision mass measurement; the MRTOF is no exception. In general, to determine the mass of a given ion, at least two known reference masses are required. The reference masses should, preferably, be isobars of the species of interest to avoid any high-order effect in the relation between ToF and masses. And also, intensity of the reference ions should be sufficiently high, otherwise the measurement duty cycle for the species of interest is reduced and the tracking of the ToF drift in MRTOF is impossible.

In online experiments, however, such isobaric references cannot always be obtained with sufficiently high intensity from the same beam as the species of interest. Therefore, an external ion source which is independent from the high-energy beam of the species of interest is necessary.

2.6.1 Alkali ion source

As previously mentioned, the flat trap can accept ions independently from two directions. This allows for the installation of offline ion sources without a need to disconnect from the RI beam line. The use of an offline source is ideal not only for performing offline testing, but also for online calibration. For precision mass measurements, isobaric references are optimal. However, for simple identification of ion species, isobars are not necessary; well-known reference ions are. To this end, thermal ion sources capable of supplying alkali and alkali-earth ions (Li^+, Na^+ , K^+, Ca^+, Rb^+ and Cs^+) have been utilized.

In the actual setup, alkali element thermal ion sources bought from HeatWave Labs [73] were installed. A typical setup is shown in Fig. 2.9. The ion source was mounted on feedthroughs connected by an ICF70-NW40 conversion nipple which is electrically isolated from ground. The ion source has a two-lead heater electrically isolated from the body. The body has three support leads. To fix the ion source in place, the heater leads and one body lead were connected to feedthroughs. An extraction electrode which has the same potential as the conversion nipple was located on the ion source to transport ions efficiently. Typical electric power to the heater was ≈10 W, at which the manufacturer estimates the ion emission surface approaches 1200 °C.

2.6.2 RF-carpet electrospray ion source

The SLOWRI and SHE-Mass projects plan to measure masses of isotopes from Be through the heaviest trans-Uranium elements. For sub-bismuth elements, with $A/q < 209$, isobaric atomic reference ions can be made from stable elements. Some elements are more readily ionized than others; the optimal ionization method depends on the element. However, for ions with $A/q > 209$, stable or long-lived atomic isobars do not exist, with the exception of $A/q \in \{232, 234, 235, 238\}$; isotopes for which atomic masses have been precisely determined by direct mass measurements are only slightly less rare in this region. Between the lack of atomic reference ions above $A/q = 209$ and lack of a flexible all-purpose method for ionizing most elements, we chose to develop a molecular ion source to produce reference ions.

There exist a wide variety of schemes to produce molecular ions. We require the ion source to meet two conditions: providing reference ions for studies up through the trans-uranium mass region, and to do so without any major changes of the existing setup. In particular, it must be vacuum compatible while not necessitating frequently breaking vacuum.

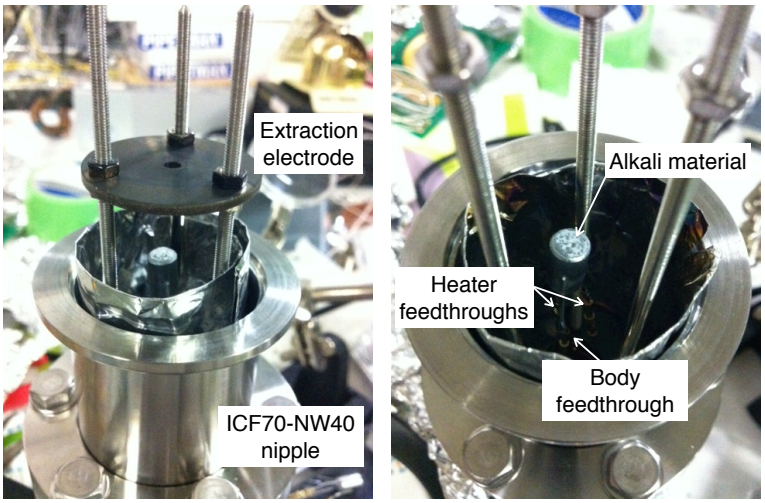

Figure 2.9: Photographs of an Alkali ion source and its mounting. The ion source was mounted on feedthroughs connected by an ICF70-NW40 conversion nipple which is electrically isolated from GND. Typical electric power to the heater was ≈10 W, resulting in a temperature of ≈1200°C.

Based on our criteria, electrospray (ESI) was determined to be the most preferable method. An ESI ion source can provide ions across a wide-mass range by adduction of polar molecules onto a central ion. The setup is rather simple and the source material can be kept at atmospheric pressure – changing references does not require opening any vacuum chamber, minimizing possible contamination of the vacuum side and traps as well minimizing time required to change references. A possible drawback to the ESI is that ions must be transported from atmosphere ($\approx 10^3$ mbar) to vacuum ($< 10^{-3}$ mbar). In conventional ESI systems, multiple skimmer electrodes are used in conjunction with differential pumping. To achieve good vacuum, either small skimmer-holes are necessary to reduce gas conductance or a large pumping system is needed to handle the heavy gas flow. The former is generally adopted. However, the small holes cause a large reduction in ion transmission efficiency. The ion intensity is not alway sufficient, then, for low-abundance molecules, which can be several orders of magnitude less than that of the main species. Minimizing efficiency loss at the skimmer is therefore highly desirable.

With this in mind, an ESI ion source with improved vacuum coupling was developed to provide isobaric molecular reference ions for SLOWRI and SHE-Mass projects [74]. In this ion source, the conventional skimmer is replaced by an rf-carpet for more efficient transport of molecular ions into the high-vacuum region. The small exit hole negates the need for a large pumping system or complex of skimmers. Moreover, the use of the rf-carpet allows more efficient transport of ions into vacuum than any complex of skimmers would.

The rf-carpet ESI ion source was tested with the MRTOF. The experimental setup consisted of the rf-carpet ESI ion source and the MRTOF in combination with the preparation traps as shown in Fig. 2.10. The ions produced by the ESI are introduced from atmosphere to low vacuum (≈1 mbar) by gas flowing through a transport capillary. The transported ions are collected above the rf-carpet. A super-imposed dc-gradient drags the ions toward the exit orifice, from which they are then transported to a quadrupole mass separator (QMS) behind the rf-carpet. The QMS was used to select the mass range of interest. The selected ions were then guided to the preparation traps where they were accumulated, cooled and injected into the MRTOF as an ion bunch confined to a small phase space. ToF measurements were performed in the manner described in Section 3.4.

The ESI part was built with the help of Dr. Gary Eiceman's group [75] at New Mexico State University. It consists of a syringe (HAMILTON: 1005TLL), a syringe pump (ISIS: CXF1010), a fused silica tube (UPCHURCH SCIENTIFIC: FS-110, 360 μm×100 μm×2 m) and an ESI capillary (PicoTip: MT320-100-5-5) as shown in Fig. 2.11(top right). The fused silica tube was connected to the ESI capillary with an insulation adapter.

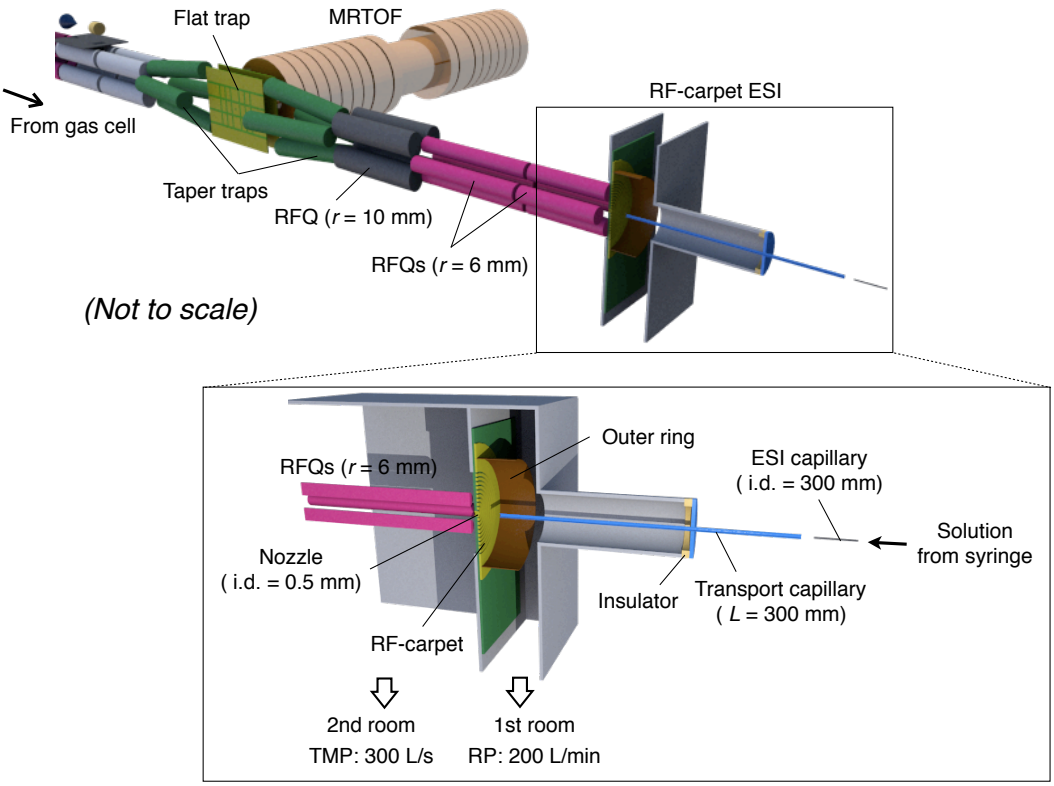

Figure 2.10: Schematic view of the RF-carpet ESI setup with the MRTOF system. The ESI setup was installed at the opposite side from the gas cell. The setup behind the RFQs of $r = 6$ mm (RFQ of $r = 10$ mm, Taper trap, Flat trap and MRTOF) was identical to online experiments.

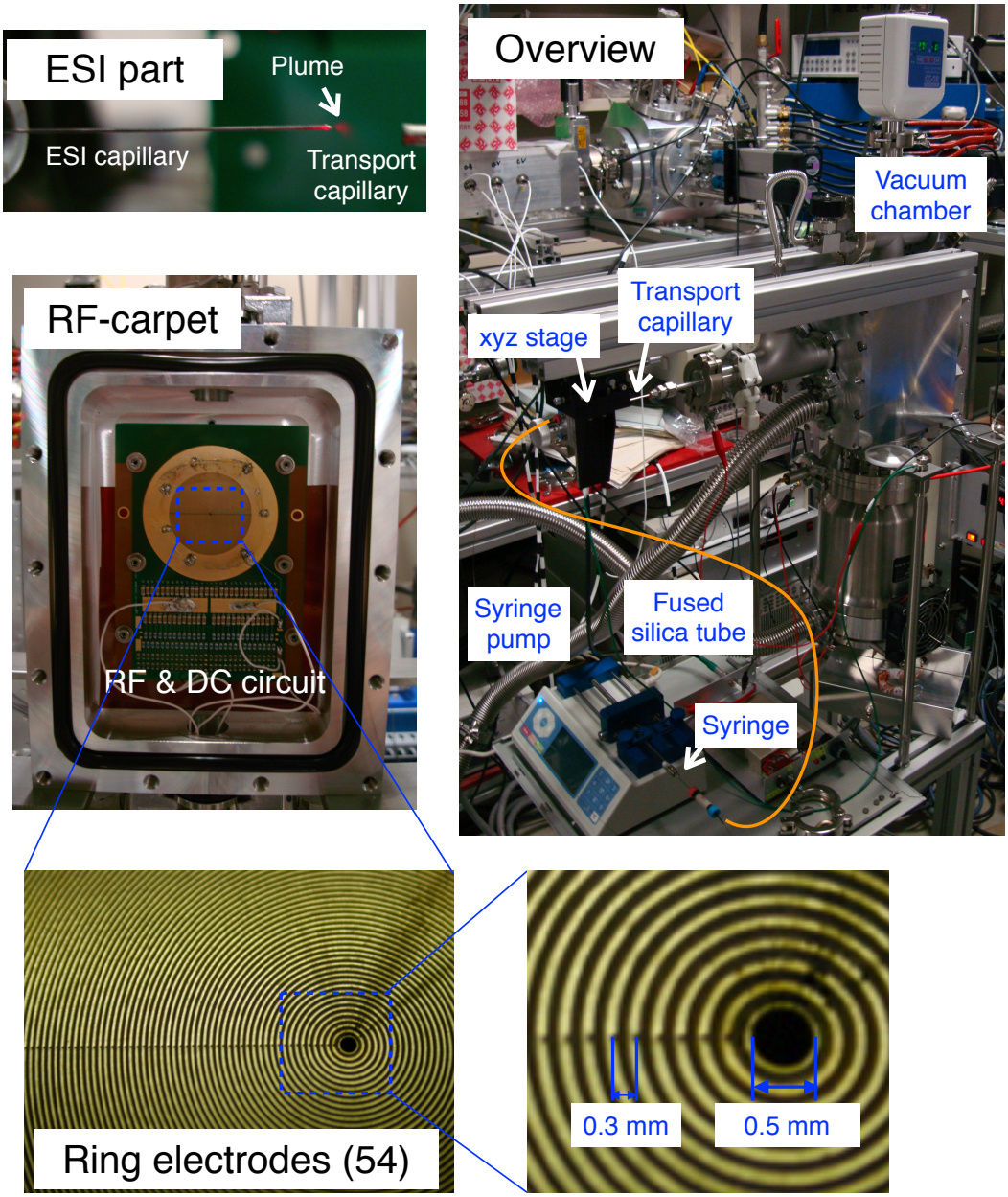

Figure 2.11: Photographs of the offline RF-carpet ESI setup. The ESI capillary was mounted on an XYZ-stage for alignment. A plume near the tip of the ESI capillary is illuminated by laser light for ease of visualization. The rf-carpet was mounted on the wall of the bulkhead between the 1^{st} and 2^{nd} rooms, together with the rf and dc mixing circuit. The rf-carpet has 55 electrodes with a 0.28 mm pitch and a 0.4 mm^2 exit orifice at the center.

The ESI capillary and transport capillary were separated by a few millimeters for insulation, and a potential difference of >1 kV was applied between them to pull the ions into the transport capillary, as well as to create the Taylor cone that the ESI depends on. The transport capillary connected the atmospheric portion of the ESI to the 1^{st} room. In the 1^{st} room, the rf-carpet PCB was mounted on the wall of the bulkhead between the 1^{st} and 2^{nd} rooms together with the rf and dc mixing circuitry. On the outer electrode of the rf-carpet, a ring electrode was attached to suppress field penetration from the ground potential of the chamber. Beyond the rf-carpet, in the 2^{nd} room, RFQ ion guides with $r = 6$ mm were located, to transport the ions to the preparation traps.

It is of utmost importance that the ion source not diminish the vacuum quality of the overall system. As such, in the 2^{nd} room the pressure needs to be less than 10^{-1} Pa, corresponding to a mean-free-path of $\lambda \sim 70$ mm, to transport the ions efficiently. To achieve this condition, the gas conductance must be minimized. In the case of the rf-carpet ESI, the conductance is fully determined by the geometry of the transport capillary and the area of the rf-carpet exit orifice. For the exit orifice, the lower bound on the area is determined by the geometry of the carpet – the diameter of the orifice should be reasonably larger than the inter-electrode pitch of 0.28 mm.

In order to categorize the gas-flow situation, the Knudsen number Kn is often used. It is defined as

$$Kn = \lambda / D, \tag{2.2}$$

where λ is the mean free path and D is a representative physical length scale, such as inner diameter of the transport capillary in this case. λ in air at atmospheric pressure is about 70 nm, so if we assume the diameter of 0.5 mm, we calculate Kn to be

$$Kn \sim 1.4 \times 10^{-4}. \tag{2.3}$$

The flow state is different depending Kn and is typically categorized as

$$Kn < 0.01 : \quad \text{viscous flow} \tag{2.4}$$
$$0.01 \geq Kn > 1 : \quad \text{transitional flow} \tag{2.5}$$
$$Kn \geq 1 : \quad \text{molecular flow}, \tag{2.6}$$

indicating that the flow in the transport capillary can be treated as viscous flow.

The gas conductance in viscous flow, C_{vis}, is described by

$$C_{\text{vis}} = \frac{\pi D^4}{128 \eta L} \frac{(P_0 + P_1)}{2}, \tag{2.7}$$

where P_0 and P_1 are, respectively, the pressures before and after the transport capillary, η is the viscosity coefficient and L is the length of the transport capillary. In air at ordinary temperatures, the viscosity coefficient is $\eta = 18.1$ μPa·s, therefore C_{vis} is calculated to be

$$C_{\text{vis}} = 1.41 \times 10^{-10} (P_0 + P_1) \text{ [m}^3\text{/s]}. \tag{2.8}$$

The flow rate Q is described as $Q = C \cdot \Delta P = C \cdot (P_2 - P_1)$, so

$$Q = 1.41 \times 10^{-10} (P_1^2 - P_0^2). \tag{2.9}$$

The effective pumping speed of the rotary pump connected to the 1^{st} room is 200 L/min and P_0 is atmospheric pressure, therefore P_1 is calculated to be ≈427 Pa, in good agreement with the measured value of 410 Pa.

The 2^{nd} room is connected to the 1^{st} by a 0.4 mm^2 orifice. Here, Kn is calculated to be $Kn \sim 0.03$, corresponding to transitional flow. Assuming molecular flow, the gas conductance, C_{mol}, is described by

$$C_{\text{mol}} = A\sqrt{\frac{RT}{2\pi M}}\ [\text{m}^3/\text{s}], \tag{2.10}$$

where R is the gas constant, T is the temperature, M is the molar mass of the gas and A is the cross-sectional area of the orifice. Using the molar mass of air at room temperature, C_{mol} is calculated to be

$$C_{\text{mol}} = 2.3 \times 10^{-5}\ [\text{m}^3/\text{s}]. \tag{2.11}$$

On the other hand, assuming viscous flow with a short tube of 0.3 mm length, the gas conductance, C_{vis}, calculated in the same manner as for the transport capillary, is found to be

$$C_{\text{vis}} = 1.4 \times 10^{-7}(P_1 + P_2)\ [\text{m}^3/\text{s}]. \tag{2.12}$$

From these conductances and the 500 L/s pumping speed of the TMP connected to the 2nd room, the pressure in the 2nd room is calculated to be 3.1×10^{-2} Pa or 8.0×10^{-2} for viscous or molecular flow, respectively. The pressure measured in the 2nd room was 4.4×10^{-2} Pa, between two conditions.

The pressure of 4.4×10^{-2} Pa in the 2nd room is sufficiently low pressure for ion transport, therefore the 300 mm long transport capillary with 0.5 mm inner diameter is sufficient.

2.7 MRTOF

Herein we describe the details of the design and performance of the MRTOF, our motivations for using it for r-process and SHE nuclei and the results we anticipate for such future experiments.

RIKEN, Japan's premiere research facility, provides multiple sources of radioactive ion beams (RIB). The BigRIPS in-flight separator at the RIBF is capable of providing nuclei along or near the r-process pathway. Yields exceeding several hundred per hour are expected for many of these nuclei [61]. Additionally, a high-intensity linear accelerator combined with the GARIS separator for SHE studies via heavy-ion fusion is available at RIKEN [76]. It can provide reasonable yields for a great many trans-uranium nuclei [77]. Efficient conversion of these energetic RIB to low energy beams can be achieved with proven gas cell techniques [62, 63] and allow the MRTOF to be used with these RIB.

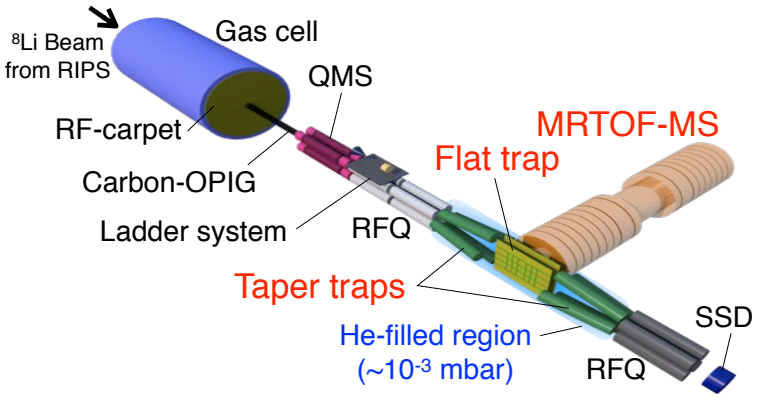

Figure 2.12: Sketch of the experimental setup (not to scale). A section of RFQ between the QMS and the taper trap was mounted on a ladder system along with a channeltron electron multiplier, which can be used as a beam intensity monitor, and an alkali ion source for offline test. An SSD detector was used for α decay detection during ^{8}Li for beam line tuning.

The components of the MRTOF are mounted on a rollaway frame of adjustable height to allow for transport of the MRTOF with a minimized concern for misalignment of the ion-optical components. This is to allow the device to be easily transported between the various RI beams available at RIKEN.

In fact, the device has been transferred from an initial off-line experimental space (B3F in the RIBF building) to the RIPS on-line experimental hall (B2F in the original Nishina Accelerator building), with the help of an elevator and a crane, in half of a day. The system was immediately turned back on and worked well after simply pumping down to nominal vacuum conditions within a few days. The primary components, shown in Fig. 2.12, are a buffer gas filled rf-multipole ion trap and an ion reflection chamber, with space reserved for a dedicated gas cell to possibly be installed in the future. In the interim, radioactive isotopes can be provided by the prototype-SLOWRI system at RIPS [11].

2.7.1 Principles of operation

The MRTOF requires low-energy ion beams amenable to ion trapping. Since the ions we are interested to measure are delivered as a high-energy beam, typically $\sim$5 A MeV for SHE and $\geq$100 A MeV for other exotic nuclei, a gas cell and energy degrader system are used for conversion to low energy beams. Stopping high-energy ion beams in helium gas is a proven technique for thermalizing such beams.

Passing through a thick degrader, typically glass or polycarbonate plastic, reduces the kinetic energy of the ions to $\lesssim 5A$ MeV. The energy is further degraded by passing through a thin beryllium window. The window provides separation of vacuum and high-pressure (20 mbar) helium environs. The ions undergo collisions with the helium gas, eventually coming to thermalize in the gas. Electric fields are employed to extract these stopped ions from the gas cell. A radio-frequency multipole ("rf multipole") ion guide system is used to efficiently transport ions through a differential pumping system after extraction from the gas cell. Ions are delivered from the gas cell as a continuous ion beam. A pair of buffer gas filled rf ion traps convert the continuous beam into a pulsed beam with optimal ion-optical properties. Ions accumulated in the first trap ("taper trap") can be efficiently transferred to the second trap ("flat trap"), where they are further cooled before being ejected orthogonally. While ions are cooling in the flat trap, more ions can accumulate in the first trap. In this way no ions are wasted regardless of the measurement duty cycle.

Ions ejected from the flat trap are transported to the MRTOF reflection chamber as a short duration, low energy-spread ion pulse. This period shortly after ejection from the flat trap will be referred to as "MRTOF injection". During MRTOF injection, ions are electrostatically accelerated toward the reflection chamber, passing through a set of beam steering electrodes along the way. The reflection chamber consists of a pair of electrostatic ion mirrors and lenses along with a field-free drift region.

Simplistically, one can envision that the ions drift back and forth, reflecting between the mirrors. However, it is important to consider that ions with slightly different kinetic energies will actually travel slightly different paths inside the mirrors. An ion with a higher energy will penetrate the mirror more deeply than an ion with smaller energy, thus traveling a slightly longer distance. As a result, after travel some distance following the reflection, the lower energy ions can catch-up with the higher energy ions. This is the mechanism used by to create a sharp time-focus in a reflection [78]. By adjusting a pair of mirror potentials the MRTOF can extend the position of this time-focus out to a flight length of kilometers, assuming sufficient vacuum conditions [53, 64].

Each mirror comprises several annular electrodes. By quickly switching the potential of the outmost electrode in the mirrors, it is possible to allow ions to enter and exit the reflection chamber. During MRTOF injection, the outermost electrode of the injection-side mirror is switched to a sufficiently low potential as to allow ions to enter the reflection chamber. After the ions have had sufficient time to reach the ejection-side mirror, but not so long as for them to have returned to the injection side, the potential is switched back to a nominal mirror value. This traps the ions between the mirrors, where they reflect back and forth until such time as the potential applied to the outermost electrode on the ejection side is lowered sufficiently to permit the ions to leave the reflection chamber and travel to an ion detector. Such ejection switching is preferably done while the ions are in or near to the injection-side mirror.

In choosing the time of ejection from the reflection chamber, one effectively chooses how many reflections an ion makes, and thus the flight path. Choosing a flight path that matches the position of the time-focus results in a minimum width in the detected time-of-flight. This width will ideally be

the so-called turn-around time for ions ejected from the trap, typically a few ns. As such, very high resolving powers can be achieved.

2.7.2 Vacuum system

It is important to achieve as good vacuum as possible in the reflection chamber to minimize collisions of ions with residual gas. Such collisions can result in ion loss or the production of a low-energy tail in the ToF spectra. The reflection chamber is pumped via a pair of turbo-molecular pumps (TMP) with 400 L/s pumping speed, one near each mirror. The electrodes and mounting structures are made of Titanium, which has attractive vacuum qualities and coefficient of thermal expansion well-matched to the ceramics used for isolating the electrodes. This allows for the system to be baked without risk of the electrode shifting about. The flat trap is mounted very near to the reflection chamber, both for ion-optical purposes, and to minimize the overall size of the MRTOF system, to allow it to be easily moved between RI sources.

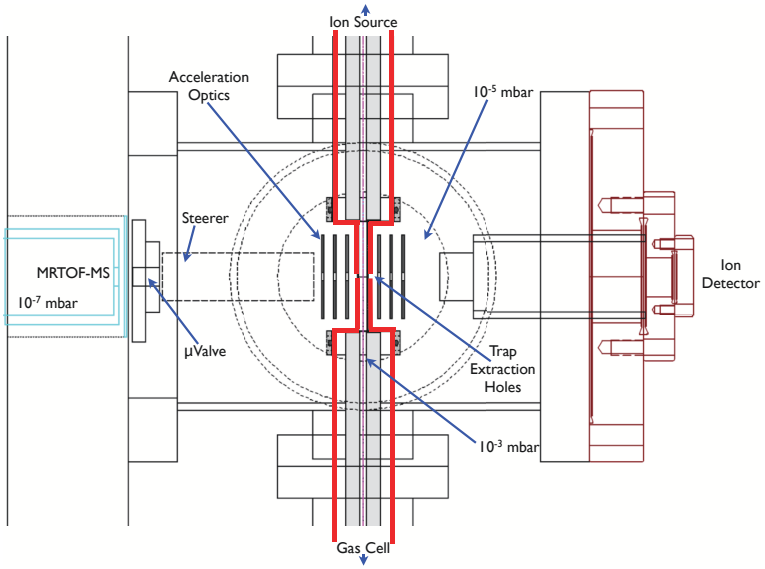

Figure 2.13: Schematic details of vacuum coupling of trap and MRTOF. The flat trap is located at the center sandwiched in between acceleration electrodes. The flat trap and taper traps are enclosed by PCBs and stainless tube to preserve the same gas pressure of 10^{-3} mbar.

The pressure requirements of the preparation traps and the reflection chamber are, unfortunately, not aligned. The preparation traps must be filled with a Helium buffer gas at a pressure on the order of 10^{-3} mbar, while in the reflection chamber high-vacuum is required, preferably $<10^{-7}$ mbar, so that the mean free path is greater than the total flight path. Both conditions are met by constructing the preparation traps such that the gas conductance to the reflection chamber is minimal. The buffer gas volume of the trap is well-sealed between a pair of printed circuit boards mounted on an aluminum block. A gas line built into the Aluminum frame allows buffer gas to be delivered directly to the sealed volume of the trap. This structure is mounted inside a multi-flange vacuum chamber pumped by a 300 L/s TMP backed by a dry scroll pump. Ions enter the trap via a large opening (3 mm $\times$ 6 mm) in the aluminum block on which the trap is constructed, the details of which will be described in Sec. 3.2. This entrance area is isolated from the primary trap vacuum chamber by means of a reentrant vacuum chamber pumped by a small TMP. The only conductance exposure to the reflection is a small 0.5 mm^2 opening through which the ions can be ejected orthogonal to the direction they entered. The Aluminum mounting bracket has a cylindrical opening on each side to allow ions to enter. The rf quadrupole rod structures used to transport the ions to the trap are placed inside stainless steel tubes which fit snugly into the cylindrical openings by means of a rubber O-ring. The far end of each tube is snugly secured, similarly by means of rubber O-ring, in an ICF70 flange. In this way, the bulk of the trap chamber, pumped by a 300 L/s TMP, experiences a minimal gas load from the trap.

A miniaturized gate valve (μ-valve) is installed at the front of the reflection chamber to allow modification of the trap chamber without introducing air (and water) into the reflection chamber. Due to space limitations and a need to minimize electric field perturbations, a special geometry is used for the gate valve. A thin plate is mounted on a rotary-linear motion feedthrough on the trap chamber side of a differential pumping barrier. The pumping barrier has a 5 mm diameter opening for ions to pass through during normal operation. A rubber O-ring separates the plate from the barrier. When the plate is moved to its lowest position, high-pressure in the trap chamber compresses the plate onto the O-ring and creates an effective valve to preserve the vacuum in the reflection chamber while opening the trap chamber for modification or maintenance. When the Helium buffer gas is removed from the preparation traps, typical background pressure in the trap chamber is $<10^{-7}$ mbar, while that of the reflection chamber is 5×10^{-10} mbar, mostly water and hydrogen. Under typical operating conditions, the vacuum in the primary trap chamber is $\sim 1.5 \times 10^{-5}$ mbar. The small geometry of the preparation traps prohibits direct measurement of the pressure inside, but conductance calculations indicate it is on the order of 10^{-3} mbar. Under such conditions, the pressure in the reflection chamber is typically 8×10^{-7} mbar. This is sufficient, as it yields a mean free path on the order of 100 m.

2.7.3 Reflection chamber

The MRTOF reflection chamber contains a suite of annular cylindrical electrodes comprising a pair of electrostatic mirrors and lenses separated by a drift tube. Each mirror is comprised of five electrodes of 20 mm length and 100 mm annular diameter with 2 mm inter-electrode spacing. The lenses are each 64 mm long with 18 mm annular diameter. The drift tube is made from stainless steel mesh, 370 mm long with an inner diameter of 105 mm. With the exception of the drift tube, all electrodes are machined from titanium, with the inner surface being gold plated. A Hamamatsu F4655-10 multichannel plate (MCP) ion detector is mounted with its detection surface 10 mm from the final electrode.

The electrodes are mounted on a U-shaped titanium support bracket as shown in Fig. 2.14. Highly uniform ceramic rods on either side of the electrodes provide insulation between the electrode and the support bracket and ensure uniform centering of the electrodes. Bolts, insulated from the support bracket by ceramic collars, are used to fix the electrodes firmly in place. At the time of mounting, the inter-electrode gap was fixed using precision gap plates.

Titanium was chosen as the material for the electrodes and support structure for both its vacuum and thermal expansion properties. The ceramic and Titanium, having nearly identical coefficients of expansion, allow the system to be baked without risk of misaligning the optics. Baking the system to a sufficient temperature, furthermore, can activate the titanium such that it will act as a pump.

The potential distribution used in biasing the mirrors and lenses, as well as the potentials for the injection to and ejection from the reflection chamber, were determined by the use of unpublished code developed by V.A. Shchepunov. The code is based on the differential algebra [79] methods commonly used to analyze synchrotron accelerators. The result of this optimization is a less-than-obvious potential distribution. The optimization suggests that, for the geometry we chose to use, best results occur by using a single lens, on the ejection side, while connecting the injection-side lens to the drift tube. Additionally, the mirror potentials are not arranged monotonically, as can be inferred from Fig. 2.15. Despite this unusual potential distribution, simulations with SIMION [72] and similar ray-tracing codes [80] indicated extremely high mass resolving power could be achieved.

With the exception of the outermost (end cap) electrodes and one lens, the mirror electrodes are connected by an ex-vacuo divider chain, reducing the number of degrees of freedom. To achieve the best possible vacuum conditions in the reflection chamber, the divider chain is external to the vacuum chamber and each electrode has an independent feedthrough. Due to its outsized bias potential, the lens is independently biased. To allow ions ejected from the trap to enter the reflection chamber, the first electrode is switchable. Similarly, to allow ions in the reflection chamber to exit to the MCP, the final electrode is also switchable.

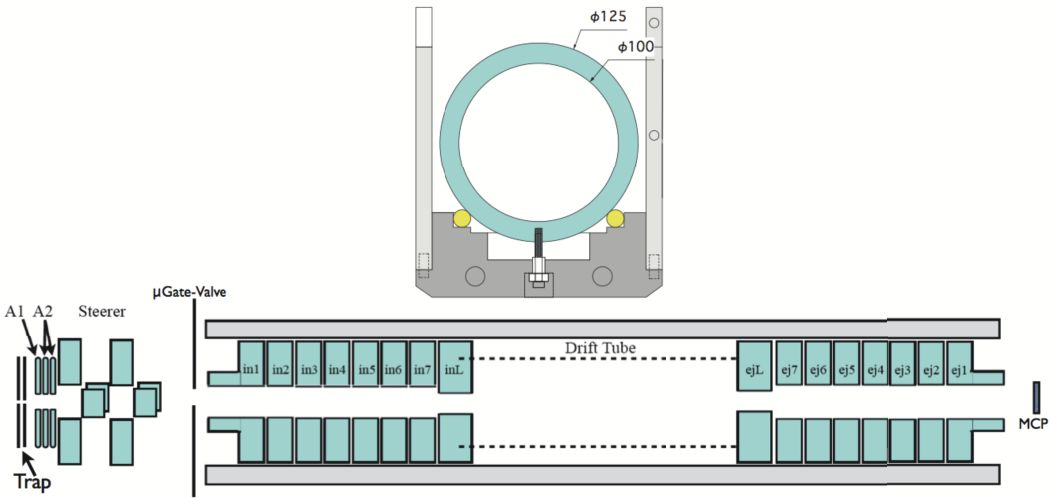

Figure 2.14: Sketch of MRTOF electrode mounting. (top) Electrode mounting technique. Ceramic rods run along the length of the support bracket to insulate the electrodes. A bolt through the electrode and bracket fixes the electrode firmly in place. (bottom) Electrode layout. Between the trap and MRTOF is a set of acceleration plates, followed by a pair of x-y steerers and a very small gate valve. The electrostatic mirrors are each built from seven ring electrodes (I1-I7 and E1-E7); in addition, there is a lens (IL and EL) between each mirror and the drift chamber.

2.7.4 Electronics

The MRTOF electronics can be divided into two groups – voltage control circuitry and timing circuitry. The voltage control circuitry is essentially USB-SPI interfaced DAC and ADC units used to regulate the various bias potentials of the MRTOF. The timing circuitry is a combination of delay circuits, fast switches, constant fraction discriminators and a TDC. The electronics are controlled via LabView interface.

Voltage distribution and stabilization

The four phases of the flat trap are created by an analog switch 74HC4052. The switch uses 2-bit logic to switch between four states. The outputs from this switch are sent to an array of PA85 fast high-voltage op-amps configured for 40× amplification. The high-capacitance of the trap results in a slew rates of ∼5 V/μs. Hence, the needs for the previously discussed dump phase to prepare the ion accumulation potential well.

The electrode bias potentials are provided by Matsusada programmable high voltage supplies. As described above, several electrodes are tied together via a voltage divider chain. This reduces the system to seven high-voltage supplies, a more reasonable number of degrees of freedom. A pair of Matsusada HPMR-5P (+5 kV, 2.5 W) are used for each of the switched electrodes. The drift potential is provided by a Matsusada HPMR-5N (−5 kV, 2.5 W), while the lens is biased using a Matsusada HFRS-10N (−10 kV, 5 W). A Matsusada HPMR-5P1.2 (+5 kV, 6 W) provides the bias for the mirror potentials, determined by a voltage divider array.

In order to utilize the MRTOF as a mass spectrograph, it is imperative that the time-of-flight of any given ion species not appreciably change over time. At a bare minimum, the time-of-flight must change smoothly and slowly (as compared to measurement duration) over time. A large effort has been made to minimize ToF drift.

There are three major sources of ToF drift. The MRTOF will expand or contract as the ambient temperature changes, leading to a small shift in the ToF. The phase of the trap rf signal has a strong impact on the ToF. The largest affect on the ToF, however, comes from the voltage distribution used to

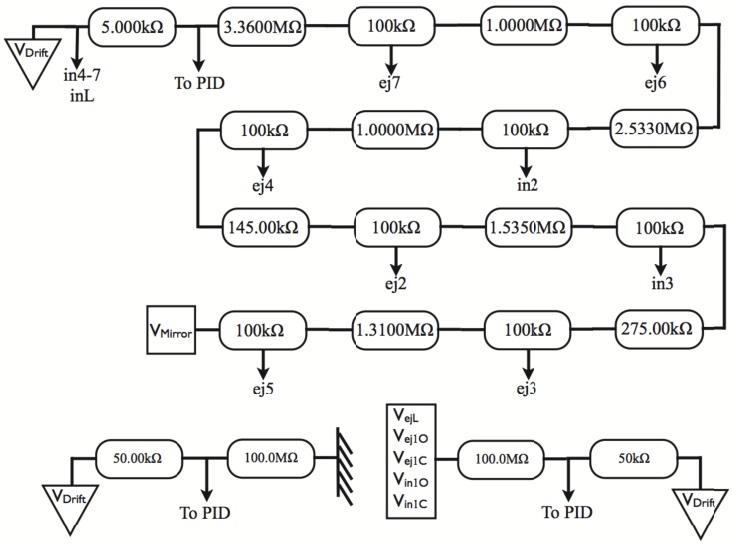

Figure 2.15: Voltage dividers used to bias the ring electrodes and monitor the various bias voltages. The 100MΩ resistors are high-precision resistors from Japan FineChem with temperature coefficients of 10 ppm/°C and the potentiometers are Bourns series 3006, chosen for their stability against vibration. All others are built from multiple ZeroTC resistors form Alpha Electronics Corp. The potentiometers allow for ∼0.1% variation in the voltages individually, without affecting the divider array. Four independent 50k:100M dividers are used for monitoring the mirror end cap voltages, while a 20k:100M divider is used to monitor the lens voltage.

form the mirrors potentials, along with the drift voltage and injection optics. Due to the massiveness of the MRTOF, little can be done about the thermal expansion, save for monitoring the temperature. The rf phase effect can be easily mollified by phase-locking the trap ejection timing. Controlling the voltage distribution is a more difficult task.

While the bias of certain electrodes are more critical than others, the most sensitive voltages approach a one-to-one effect on the ToF – wherein a 1 ppm change in voltage could lead to a 1 ppm change in ToF. To minimize these effects, a three-fold strategy is employed. The first strategy makes use of the fact the mirror potentials should be isochronous – small changes in the kinetic energy of an ion should not result in a change in the ion's ToF. For this reason, the mirror biases are provided by power supplies floating on the drift potential. In this way, if the drift potential changes slightly, all the other voltages drift with it, resulting in a slight change in the energy of the ion that should be compensated by the isochronous mirror potentials.

The second strategy is to bias most of the mirror electrodes using a resistive divider array, as shown in Fig. 2.15. The divider array uses Zero-TC resistors from Alpha Electronics Corp. These resistors have a temperature coefficient of ∼0.15 ppm/°C. Because the mirror end cap electrodes are switched between an injection (ejection) voltage and a trapping voltage, they are excluded from being biased via the divider array to minimize unwanted switching noise.

The third strategy is actively regulating the bias supplies. In total, seven power supplies are used in the reflection chamber – two for each end cap, one to set the mirror potentials, one for the ejection side lens (EL) and the drift potential that they float on. Each of these are monitored by using a high-impedance voltage divider. The dividers shown in Fig. 2.15 make use of 100 MΩ high-precision resistors from Japan Finechem (TC ∼ 10 ppm/°C) in series with a 50 kΩ ZeroTC resistor. The supply voltage is connected to the 100 MΩ resistor while the drift potential is connected to the ZeroTC resistor, providing a 1:2000 scale voltage relative to the floating ground. The monitors for the mirror potential and the drift potential are exceptions. The drift potential (being the floating ground) must be measured relative to true ground, as shown in Fig. 2.15. The mirror potential, as shown in

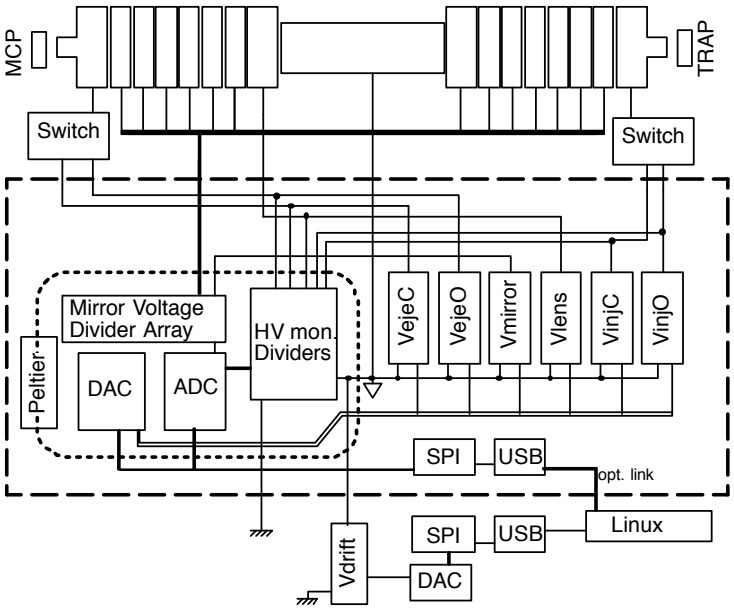

Figure 2.16: Sketch of voltage control and distribution system

Fig. 2.15, is connected to the floating ground by the 12.08 MΩ divider array. The voltage across the final resistor in the chain is used as a 1:2400 voltage monitor signal.

These voltage monitor signals are used as a feedback signal for a digital PID system, which maintains the voltages. The monitor signals are digitized using a 24-bit ADC (LTC2449, Linear Technologies) using a MAX6350 as voltage reference. An onboard computer then adjusts the high-voltage power supply programming voltages, according to a PID algorithm, to maintain each voltage at the desired value. The programming voltages are supplied by using a precision op-amp (OP4177) to combine two outputs from a 16-bit, 32-channel DAC (AD5372, Analog Devices) so as to approximate a 22-bit DAC. The ADC-DAC system, as well as the divider array and 1:2000 voltage dividers, is inside a well-sealed container. The temperature inside the container is measured using an LM135 temperature sensor. The PID system regulates the temperature inside the container by means of a 15 W Peltier cooler/heater (SL-3FF from Nippon Blower) element.

Timing and ion detection

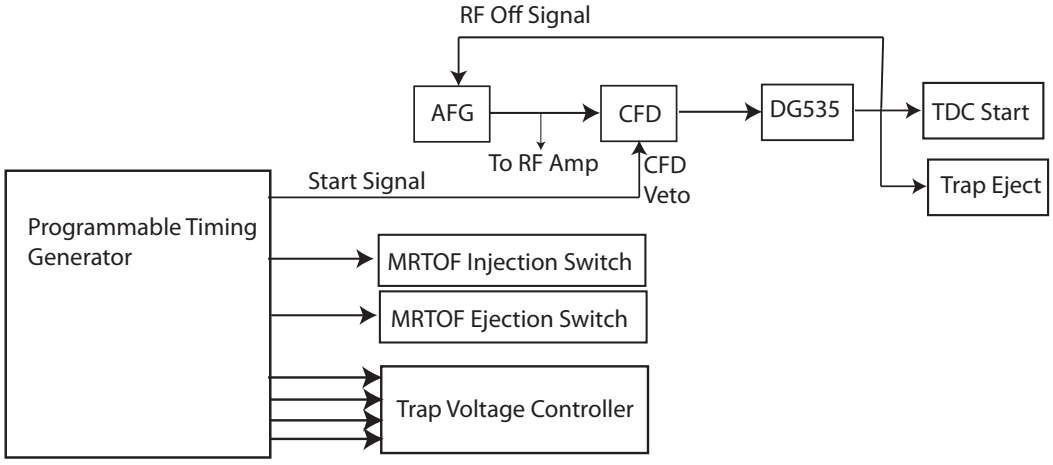

Figure 2.17: Schematic of MRTOF Timing Electronics

A schematic overview of the timing circuitry is shown in Fig. 2.17. In the case of the MRTOF, a P7887 TDC, from Fast ComTec GmbH, is used to measure the time between ejection of ions from the flat trap and their arrival at an MCP detector. The P7887 has 250 ps precision even with multiple stop signals. At the heart of the timing circuitry is a programmable timing generator NI PCI-6602 controlled by LabView. It provides TTL timing pulses for triggering trap ejection, injection mirror end cap switching, ejection mirror end cap switching and to select trap voltage configuration state. To create signals that are precisely delayed, a Stanford DG535 precision programmable delay generator is used. to adjust the trap potential through four states, a trap ejection signal, and a pair of signals to trigger injection into and ejection of ions from the reflection chamber. The trap ejection signal is considered to be the start of a cycle. It is used to eject trigger the ejection of ions from the trap and to phase lock the trap rf signal at ejection, which is vital for ensuring the ions always have the same initial conditions.

The trap ejection signal is split and sent to a Stanford DG535 precision programmable delay generator as well as being inverted and used as a veto for a constant fraction discriminator.

3 Offline studies

Before running, we must learn to walk. Similarly, before the MRTOF could be used for online mass measurements of any short-lived radioactive nuclei, numerous offline studies were required. These studies included computer simulations required for optimal design of the traps and reflection chamber, measurements of the efficiency of the traps, simulation of the MRTOF performance to optimize the design, and measurement of the actual MRTOF performance.

3.1 Taper trap

The taper trap required a fair amount of offline effort. Much time was spent on simulations. Good figures of merit for its performance had to be devised. The performance had to be measured.

3.1.1 Simulations for taper trap

Prior to making the taper trap, its performance and an optimal geometry were simulated by SIMION [72]. First a symmetric taper trap was considered, as shown in Fig. 2.7(b). For the same rf voltage and frequency, the strength of the effective drag force is uniquely determined by the angle of the taper rods Δr_0 which distort the electric field. Important quantities to be investigated in simulations were the transmission efficiency and the beam size after passing through the taper trap. The former reflects the strength of the effective drag force, while the latter influences the transfer efficiency into the flat trap located after the taper trap.

The transmission efficiency was calculated as a function of Δr_0. Ion trajectories in the taper trap were calculated assuming a Helium buffer gas pressure of 0.5 Pa, an rf frequency of 4 MHz and an rf voltage of 720 V_{pp}, which is a typical pressure for buffer gas cooling and realistic conditions for the system. Ion-gas interactions were modeled as hard sphere collisions. 2000 ions were started at the outer edge ($\Delta r_0 = 0$ mm) of the taper trap with an initial energy of 5 eV. The number of ions reaching the inner edge of the taper trap within 1 ms were then recorded. The transmission efficiency was defined as the ratio of recorded ions to initial ions. These calculations were performed for various Δr_0. The result is shown in Fig. 3.1(left). For $\Delta r_0 = 0$ mm, *i.e.*, a parallel RFQ without segmentation, only $\approx$57% of ions can be transported since the ions are stopped by collisions with the buffer gas and there is no force to transport them. For larger Δr_0, the transmission efficiency increases up to $\approx$93%. There is an effective drag force for these cases, therefore almost 100% of ions will eventually be transported, although such may require 3 - 5 ms.

Increasing Δr_0 weakens the confining pseudo-potential well and distorts the quadrupole field. Such features could affect the beam size. The beam size should be as small as possible because the entrance aperture of the flat trap is 4 mm $\times$ 11 mm and the effective acceptance of the flat trap is $\approx$70% of the gap, *i.e.*, $\approx$2.8 mm. The transverse beam profile was recorded at the same inner edge position used to determine transmission efficiency. The beam size was defined as $\pm 6\sigma$ of the Gaussian fitting of the beam profile corresponding to the area of 99.7%, where σ is the standard deviation of the Gaussian. Figure 3.1(right) shows the beam size as a function of Δr_0. For $\Delta r_0 = 0$ mm, the beam size is $\approx$1.7 mm, which is sufficiently small compared to the flat trap entrance. For larger Δr_0, the beam size increases, up to $\approx$4.3 mm for $\Delta r_0 = 2$ mm. The beam size of >3.0 mm at $\Delta r_0 > 0.8$ mm is slightly larger than the flat trap acceptance and causes an efficiency loss for the transport from the taper to the flat trap. If the transport time from the taper trap to the flat trap is longer than 3 ms, $\Delta r_0 = 0.5$ mm could be better than the others. Therefore, the taper trap with $\Delta r_0 = 0.5$ mm was adopted for experiments.

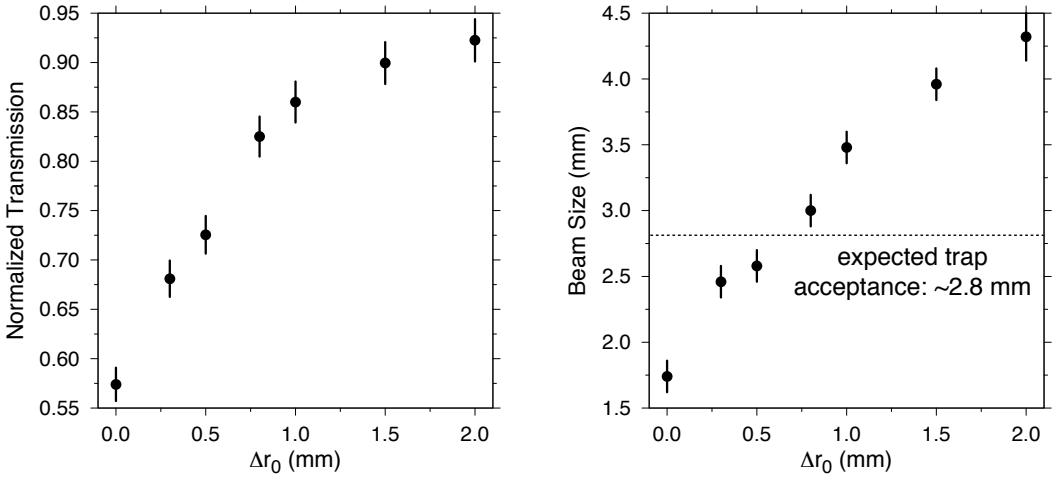

Figure 3.1: Simulated transmission efficiency and beam size as a function of Δr_0

3.1.2 Experiments for taper trap

The performance of the preparation traps was investigated in terms of the trapping efficiency, cooling time and trap capacity. Alkali ion sources capable of providing K^+ and mono-isotopic $^{23}Na^+$ and $^7Li^+$ ions were used. $^7Li^+$ and $^{23}Na^+$ were used for the efficiency measurements, while K^+ ions were used for cooling time and capacity measurements.

In a buffer-gas filled trap, cooled ions do not come out efficiently or quickly without any drag force. As previously mentioned, a taper structure produces an effective axial drag force. Due to the drag force, the pre-cooled ions can be efficiently transported to the flat trap. The axial drag force of the taper trap is determined by the rod angle, α. The value of α was optimized using SIMION, and an angle of $\alpha = 2.6$ mrad, corresponding to $\Delta r_0 = 0.5$ mm for $L = 190$ mm, was adopted as detailed in Sec. 3.1.1.

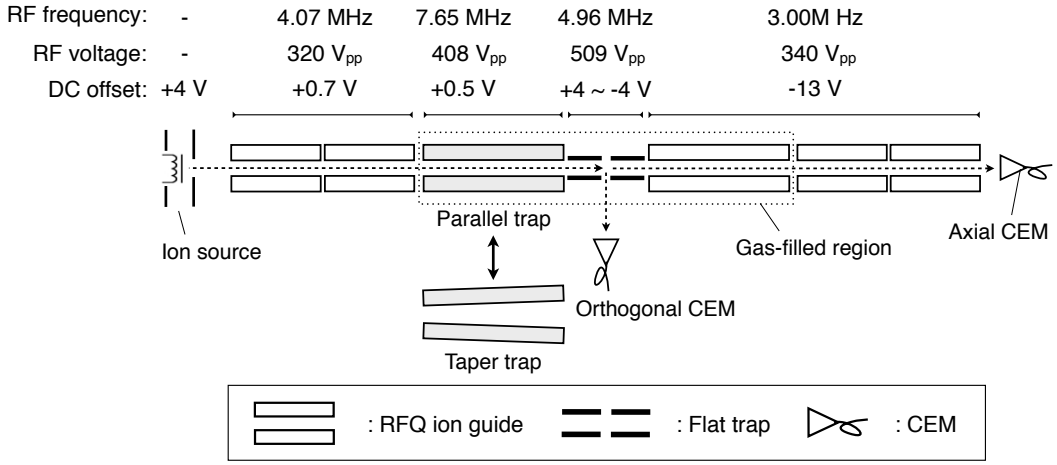

Figure 3.2: Experimental setup for the efficiency measurement of parallel and taper trap mode. Ions from the alkali ion source were transported by an rf quadrupole ion guide to the trap system. Channel electron multiplier (CEM) detectors were installed at the axial and orthogonal exits. Typical rf frequencies, rf voltages and dc offset voltages are listed above.

Using this geometry, the effective drag force and the trapping efficiency of the taper trap were studied. The experimental setup is shown in Fig. 3.2 together with typical rf frequencies, rf voltages and dc offset voltages. Na^+ ions from the alkali ion source were transported to the taper trap by rf quadrupole ion guides which consist of four 10 mm rods. CEM detectors were installed at the

axial and orthogonal exits. In order to reduce the gas conductance, the taper trap and flat trap were enclosed by stainless steel tubes and collimators. The pressure in the gas-filled region was maintained at ≈0.5 Pa as was used in calculations for the gas-flow conductance and the pressure measured outside of the flat trap. The flat trap was operated in transmission mode; the segmented dc electrodes were set to a uniform potential distribution. Measurements were made using both a tapered and parallel configuration for purpose of comparison.

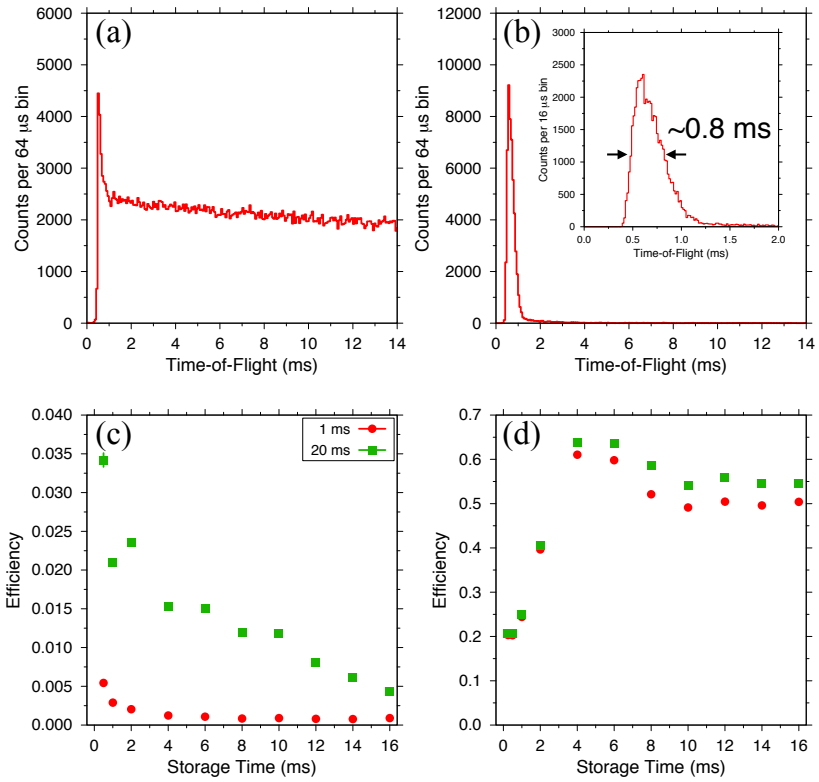

Figure 3.3: (top) Typical time-of-flight spectrum measured by CEM at axial exit for (a) the parallel trap and (b) the taper trap with enlarged figure around the peak. The ion counts are not comparable because the absolute intensity is different in each case. (bottom) Transport efficiency as a function of the storage time for (c) the parallel trap, (d) the taper trap. For both, the ion counts were integrated over 1 ms (filled squares) and 20 ms (filled circles).

Due to the taper effective drag, accumulated ions are ejected faster from the taper trap than the parallel trap, from which they essentially just diffuse. Figures 3.3(a) and (b) show axial ejection time-of-flight spectra for the parallel trap and the taper trap, respectively. As could be expected, the spectrum from the parallel trap has an extremely long tail, while the taper trap produces a sharp peak with a width of only 800 μs. The initial spike ahead of the long tail can be explained by ions which accumulated near the flat trap entrance which were extracted quickly when the potential of the flat trap entrance decreased. In the case of the taper trap, it is clearly seen that nearly 100% of the ions are extracted within this peak. This shows that the axial drag force due to the taper structure continuously pushes the ions toward the exit side, causing most ions to accumulate near the flat trap entrance from where such ions can quickly be extracted as a fairly tight bunch.

The transport efficiencies from the taper (parallel) trap to the flat trap were measured with the following methodology. First, the ion rates without trapping in the taper (parallel) trap, Y_{dc}, were measured at the axial CEM. Second, the ion rates after trapping, Y_{trap}, were measured at the same detector for various storage times. The transport efficiency, $\epsilon_{\mathrm{trans}}$, shown in Fig. 3.3(c) and (d) was defined as $\epsilon_{\mathrm{trans}} = Y_{\mathrm{trap}}/Y_{\mathrm{dc}}$.

The efficiency of the parallel trap quickly decreases with increasing storage time, while the taper trap peaks at 4 ms, then slowly reduces to an equilibrium. For the parallel trap, well-cooled ions, *e.g.* after a longer storage time, are hard to extract without an axial drag force, while for the taper trap, the well-cooled ions are efficiently extracted due to the effective drag force. It should be noted that for the taper trap, during the storage time of 0 - 4 ms ions are not well cooled, therefore the beam size is insufficiently small and the efficiency is not maximized within 4 ms. The taper effect is also exemplified by the difference in signals integrated over 1 ms and 20 ms, as shown in the bottom panels of Fig. 3.3. For the parallel trap, only ≈14 - ≈20% of ions from the 20 ms integrated time are contained in 1 ms integrated time, while for the taper trap, more than 90% of extracted ions are found in the first integrated millisecond.

3.2 Flat trap

The flat trap has a novel flat geometry specialized for brilliant ion bunch production for MRTOF mass measurement. Thus, in order to create a sufficiently good quadrupole field for ion trapping it was investigated in detail by calculations. The performance of the flat trap was then investigated experimentally with MRTOF.

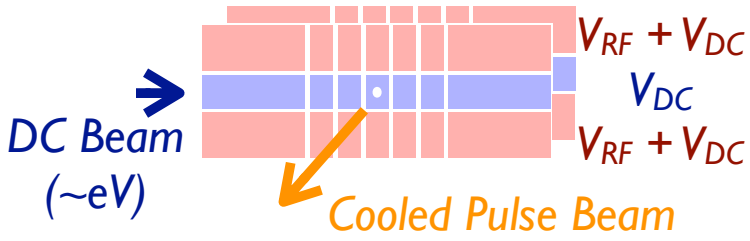

Figure 3.4: Schematic view of the flat trap. Each PCB consists of three strips divided into 7 segments (see Fig. 2.8). The central electrode of each board has a 0.5 mm^2 plated hole at its center. By applying a potential difference between the center electrodes of the PCBs, ions can be extracted orthogonal to the injection axis through the small exit holes.

3.2.1 Simulations for flat trap

It is known that the standard four-rod quadrupole creates a good approximation to a quadrupole electric field, and that this is maximized for rod diameter $r = 1.148r_0$ [27] where r_0 is the inter-rod radius. One way to evaluate the goodness of the quadrupole field is to look at the linearity of the fields along the transverse axes. Along the transverse axes, a perfect quadrupole field obeys

$$E_i = \left(V/r_0^2\right) x_i. \tag{3.1}$$

So the linearity of the fields along the axes can be used as a figure of merit. An additional figure of merit is the ratio of the linear coefficients for the two radial fields, which should ideally be unity.

In this investigation the "non-linearity" is defined as the deviation of Pearson's r from unity and the "imbalance" is defined as the deviation from unity of the ratio of linear coefficients. Using a standard Successive Over-Relaxation (SOR) algorithm, the potential map for a standard four-rod quadrupole was calculated. In each case the rod radius was $r = 150$ grids. After calculation of the potential map, the fields along the axes were calculated, the value of Pearson's r was calculated for the field along each axis, and their product was recorded, as well as the ratio of the linear fitting coefficients. This was repeated for a series of inter-rod distances, r_0.

The results are shown in Fig. 3.5. The minimun of non-linearlity was found at $r/r_0 = 1.111$ as shown in Fig. 3.5(left). A difference from proper value of 1.148 is 3% and corresponding to 3 grid units difference. As the field imbalance should be zero by geometric arguments in Fig. 3.5(right), the

deviation must be from the imperfect circular approximation on a grid – for larger r/r_0 the inter-rod separation is less and the effects of imperfection are amplified. Experience informs us that even under such conditions, the RFQ can be well simulated; therefore we will take an imbalance of 0.05% as equivalent to perfect when we approach the optimization of the flat trap.

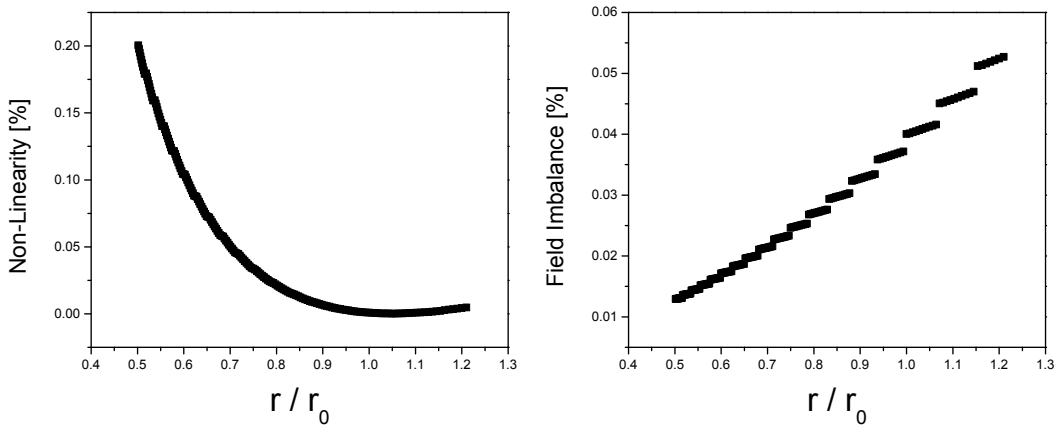

Figure 3.5: Simulation results of the non-linearity (left) and the imbalance (right) of a quadrupole field in the flat trap. The minimum of non-linearity was found at $r/r_0 = 1.111$. A difference from proper value of 1.148 is 3% and corresponding to 3 grid units difference.

It is also worthwhile to look at the region over which the linearity is good. Figure 3.6 shows the residual from a linear fit for the field along the x-axis. The linear fit was essentially perfect out to $\sim 0.67 r_0$ and the non-linearity was 10 ppm over $0.9 r_0$. This is our basis of comparison for the flat trap optimization.

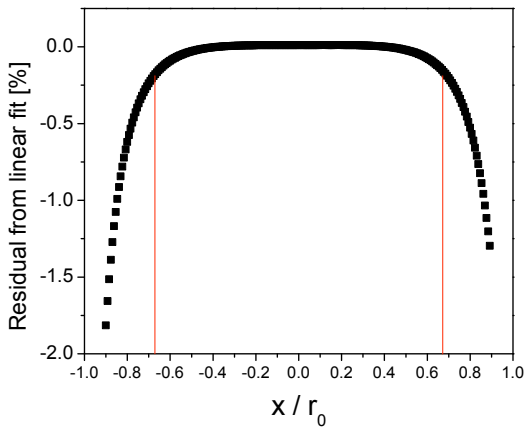

Figure 3.6: Residual from linear fit at $x/r_0 = 1.154$. The linear fit was essentially perfect out to $x \sim 0.67 r_0$ indicated by red line.

An initial geometry was set for 50-grid-units long electrodes separated by 10 grid units and gapped by 100 grid units. The geometry is shown in Fig. 3.7(left). The potential map was calculated using a standard SOR routine, the same as for the four rod quadrupole above. Based on the results for the optimal four rod system, a goal of non-linearity was set to <250 ppm along 2/3 trap volume with field imbalance of <0.05%.

The axial field strength for the initial geometry is shown in Fig. 3.7(right). This is clearly not an optimal solution. To find an optimal solution, the properties of the general geometry were investigated systematically. A program to create the geometry, calculate the potential $V(x, y)$, determine the axial fields and perform linear fitting was developed. The program allowed for modification and recalculation of the potential $V(x, y)$. For simplicity, the inter-sheet gap was fixed at 100 grids, since this gap was

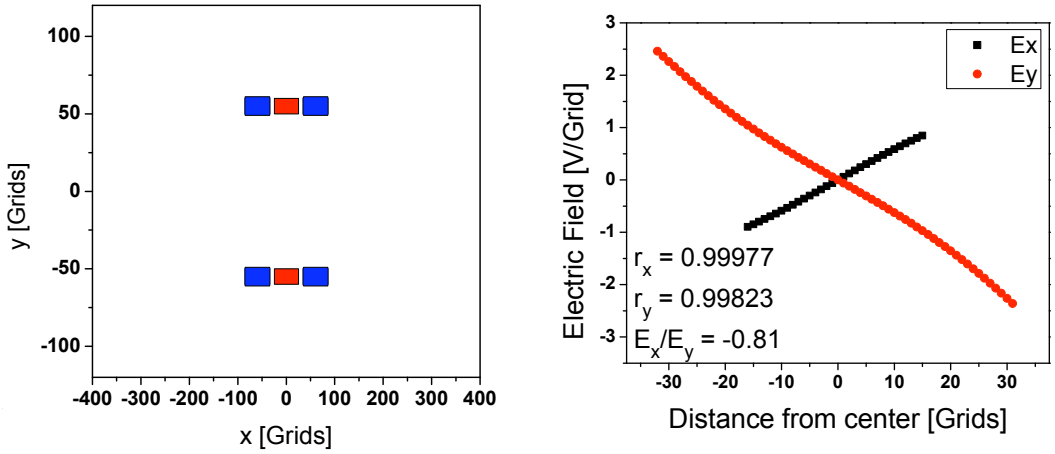

Figure 3.7: An initial geometry of the flat trap (left). The electrodes with applied rf signals are shown with blue squares and the grounded electrodes are shown with red squares. Each electrode was 50-grid-units long, is separated by 10 grid units and gapped by 100 grid units. The radial fields for the initial geometry are clearly not an optimal solution (right).

also fixed in the initial design of the trap at 3 mm.

To begin, the inter-electrode spacing was fix at 10 grids and the electrode lengths were scanned. For this scan, a unity ratio in the length of the center and outer electrodes was maintained. The minimum non-linearity was found for a length of 86 grids as shown in Fig. 3.8(left). This geometry, referred to as 86-10-86-100 has a non-linearity of 180 ppm with a 2% field imbalance.

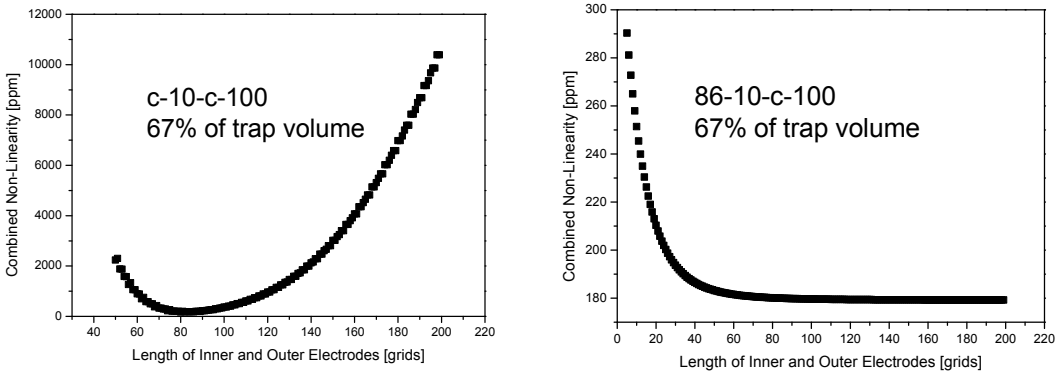

Figure 3.8: Combined non-linearity as a function of the length of both inner and outer electrodes (left) and outer electrodes with fixed central electrodes as 86 grids (right). The geometrical factor described in the figures are defined as (inner electrodes)-(inter-electrode spacing)-(outer electrode)-(trap gap) and scanning values are indicated as "c". In both figures, the non-linearity was calculated for 67% of trap volume. In the right figure the minimum non-linearity was found for a length of 86 grids. In the left figure, a non-linearity of 179.8 ppm was found at the length of 115 grids.

Next the central electrode length was fixed at 86 grids and the length of the outer electrode was scanned. For a length of 115 grids, the non-linearity was 179.8 ppm as shown in Fig. 3.8(right), but the field imbalance was reduced to 0.58%. Finally, the inter-electrode spacing was scanned and it was found that for the geometry 86-11-115-100 the non-linearity was 178.9 ppm with a field imbalance of 0.13%. This was not as nice as the four rod quadrupole, but is likely sufficient for our needs.

Next, a support frame was added to the geometry to ensure that it will not negatively impact the operation of the trap. The optimization was begun with a worst-case scenario of a frame which is 0.6 mm from the outer edge of the trap. The geometry is shown in Fig. 3.9(left); the scale is in millimeters.

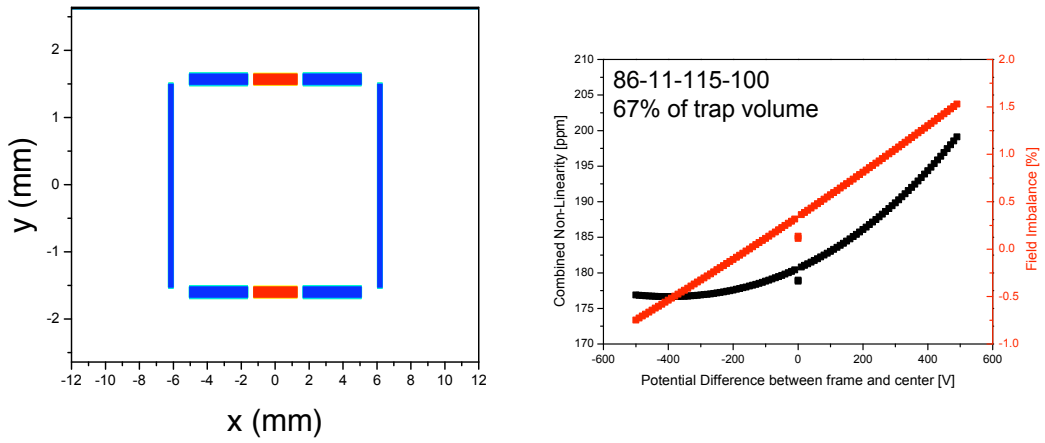

Figure 3.9: The geometry of 86-11-115-100 with a grounded support frame which is 0.6 mm from the outer edge of the trap (left). The combined non-linearity and the field imbalance are shown as a function of the potential difference between the frame and inner electrode (right).

The simple task of evaluating the fields as a function of the potential applied on the frame, relative to the inner electrode, was performed when the potential difference between the inner and outer electrodes is 200 V. As can be seen in Fig. 3.9(right), the effect of any reasonable potential difference is negligible. As such, the frame seems not to be disconcerting, since for any greater frame size the effect must be reduced. The drop at 0 V is the value for no frame. The electrode "disappears" at exactly zero volts. This is a non-detrimental artifact of the calculation method.

Now, the trap region itself must be finally considered. The impact of the central hole yet needs to be considered. In Fig. 3.10, the geometry 86-11-115-100-10, which adds a 0.3 mm wide hole to the inner electrodes, was shown. The impact of the hole, as a function of width is shown in Fig. 3.11. As we can see, it is very important to keep the hole as small as possible.

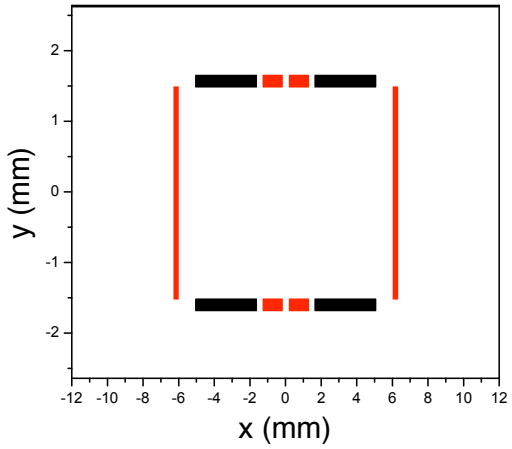

Figure 3.10: The geometry with 0.3 mm wide holes to the inner electrodes

For our desired 0.3 mm hole, the field is not unacceptably poor; the non-linearity is 286 ppm, with a field imbalance of 0.97%. This may not be great for use as a mass filter, but should be plenty sufficient for an ion trap.

As a final detail of the quadrupole field is the field factor. For an ideal quadrupole, the electric field is given by $E_i = (V/r_0^2)x_i$. The slope of our field for geometry 86-11-115-100 is 0.047 V/grid for V_q = 200 V and r_0 = 50 grids, which should give a slope of 0.08 V/grid. Thus, we have a field factor of 1.7 which should be taken into account when attempting to use this device as a quadrupole mass separator.

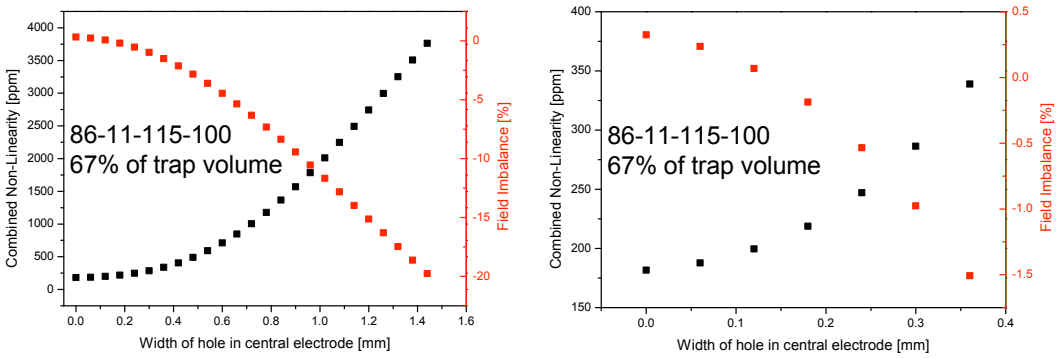

Figure 3.11: The combined non-linearity and the field imbalance as a function of the width of hole in inner electrodes (left) and the enlarged figure up to 0.4 mm (right).

Now, let us consider extraction of ions from the trap. For this, three geometries should be compared – the four rod quadrupole, the central switching flat trap and the full switching flat trap. In Fig. 3.12(left), the potential for full switching, whereby the center and outer electrodes are both set to $\pm V_d$, are shown. The red box in Fig. 3.12 indicates the region which was analyzed. The same region was analyzed for the central-only switching, in which the center electrodes are set to $V_{outer} \pm V_d$. A similar image is presented for the case of the four rod dipole in Fig. 3.12(right). The top and bottom rods are set to $\pm V_d$, while the side electrodes are at ground.

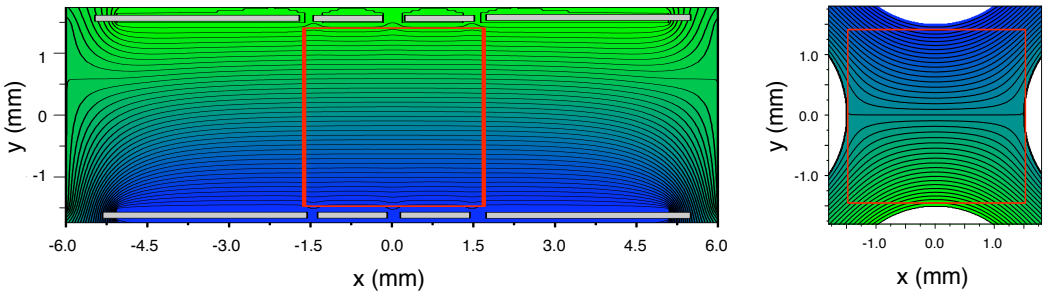

Figure 3.12: The equipotential line during the ejection from the flat trap with full switching (left) and the four rods quadrupole (right). Res boxes indicate the region which was analyses.

Figure 3.13 shows a comparison of the three scenarios. While the full switching flat trap is best, the central switching system is decidedly better than the four rod system. Furthermore, the region of ± 0.15 mm is the only part where the dipole field truly matters, as this is the area below the extraction slit. In this region both flat trap scenarios are equally good.

3.2.2 Cooling time of flat trap

Herein the cooling time characteristics of the flat trap are mainly discussed. As previously described, the flat trap is located after the taper trap. Its function is to provide final ion bunch preparation for the MRTOF. The width, emittance, and energy spread of ion bunches ejected from the flat trap directly affect the efficiency and the mass resolving power of the MRTOF. The flat trap is required to efficiently provide fast cooling of both axial and radial ion motions, and to eject ions with low emittance. Ejection is achieved by the novel flat geometry's ability to make a pure dipole field for orthogonal ion ejection. This is in stark contrast to the axial ejection from a traditional Paul trap, which produces ion pulses with large high-order optical aberrations.

Fast cooling is an important feature needed for the measurement of short-lived nuclei. In Helium buffer gas at pressures of $\approx 10^{-3}$ mbar at room temperature, the axial cooling is achieved by collisions with He atoms in the dc potential well created by the segmented electrodes, while the radial cooling is

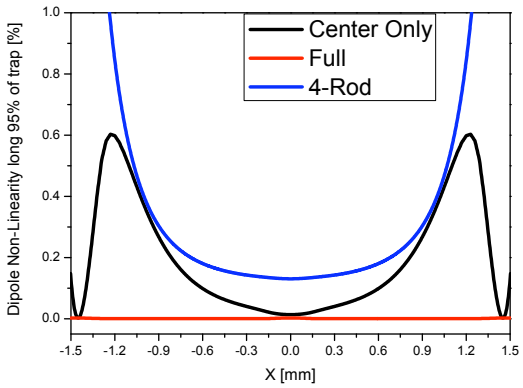

Figure 3.13: The non-linearity of dipole fields for the three situations. While the full switching flat trap is best, the central switching system is decidedly better than the four rod system.

achieved within the confinement of the rf quadrupole pseudo-potential well. Because of the orthogonal ejection from the flat trap, the axial and radial cooling are partially decoupled; both axial and radial motions must be quickly cooled for effective ion bunching.

As the ion cloud cools, it becomes smaller and the velocity of ions decreases. As the exit hole comprises a much smaller geometric factor along the axis than perpendicular to it, the axial cooling strongly determines the fraction of the ion cloud which can pass through the exit hole. The radial velocities of the ions, however, contribute to the energy spread and turn-around time, which determines the detected pulse width. Thus, the rate of detected ions provides a figure of merit for axial cooling, while the pulse width is a figure of merit for radial cooling. As shown in Fig. 3.14, both the count rate and peak width saturate within around 2 ms at $\approx 3 \times 10^{-3}$ mbar, indicating that the ions accumulated in the flat trap are fully cooled, both axially and radially, within 2 ms. The achieved cooling time is sufficiently short for mass measurements of short-lived nuclei with MRTOF.

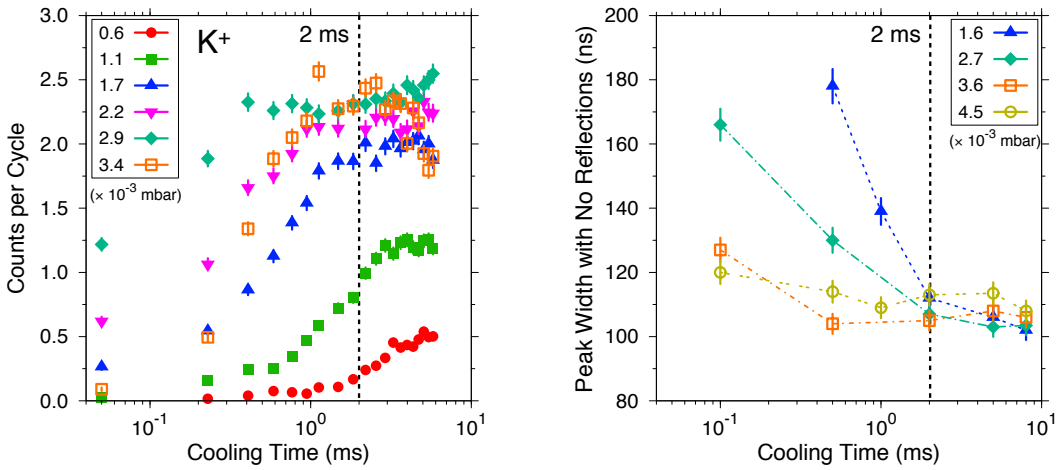

Figure 3.14: Two types of cooling time dependences of K^+ for various gas pressures. (left) The ion count rate, measured at the orthogonal CEM, as functions of the cooling time, representing the axial cooling. (right) The width of the ToF peak, measured after MRTOF without reflections, as functions of the cooling time, representing the radial cooling.

3.2.3 Trapping capacity of flat trap

In online experiments, the gas cell may deliver intense molecular impurities. Too many impurities could saturate the trap. To estimate the maximum allowable contaminant ratio, the trap capacity was measured using K isotopes with the MRTOF. The result is shown in Fig. 3.15. The intensity

of incoming K^+ ions was measured at the rods of the taper trap and the total number of trapped K ions was estimated from the $^{40}K^+$ counts at the MCP after mass analysis in the MRTOF. At high intensities, individual ion signals overlap and ion counting is not possible. K^+ ions were used due to the low abundance (0.0117%) of ^{40}K, which allowed for reasonable estimation of the total number of ions in a given pulse. By separating the K isotopes in the MRTOF, the total ion rate could be calculated from the rate of $^{40}K^+$ which never saturated due to its very low abundance. This measurement was performed under different conditions from the trapping efficiency measurements and thus the efficiencies cannot be compared.

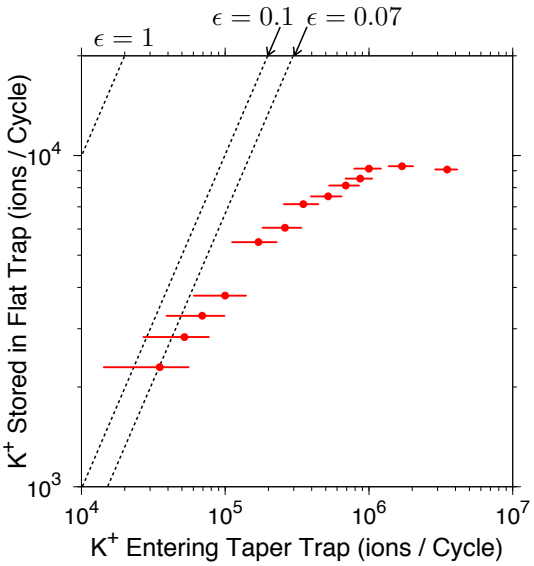

Figure 3.15: Trapping capacity of the flat trap. The total K^+ ions stored in the flat trap was estimated from the $^{40}K^+$ counts at the MCP after mass analysis in the MRTOF. Lines for efficiencies of $\epsilon = 1, 0.1, 0.07$ are described.

From the result described in Fig. 3.15. The flat trap capacity was found to be around 9.3×10^3 ions. The maximum ion density in the trap, $n_{\max}$, is dominantly limited by the space charge. $n_{\max}$ can be evaluated to be

$$n_{\max} = \frac{qV_{0\mathrm{p}}\epsilon_0}{er_0^2} = \frac{4D_r\epsilon_0}{er_0^2} \tag{3.2}$$

where q is the Mathieu's q-value, $V_{0\mathrm{p}}$ is the rf amplitude, r_0 is the inter-rod radius of the quadrupole field, and D_r is the pseudo-potential well depth. Using the experimental parameters, $q = 0.4$, $r_0 \sim 1.4$ mm, $V_{0\mathrm{p}} = 370$ $V_{0\mathrm{p}}$, which correspond to $D_r = 37$ V, $n_{\max}$ is obtained as $n_{\max} \sim 6 \times 10^4$ mm^{-3}.

Assuming the shape and the volume of the ion bunch are cylindrical shape and $\sim$0.2 mm^{-3} which corresponds to the radius of $r \sim 0.2$ mm and the width of $w \sim 2$ mm, the maximum number of ions per bunch is evaluated as $\sim 1.2 \times 10^4$ ions which is well-consistent with the experimental saturation limit of $\sim 9.3 \times 10^3$ ions.

3.3 Dual-trap system

Ions transported from gas-cell side have an energy of less than 10 eV and an energy spread of a $\sim$1 eV typically due to gas collisions in the poor vacuum region. On the other hand, the energy loss in the flat trap is estimated as a $\sim$1 eV. The lower-energy ions, which are well-cooled in the taper trap, are gently transported from the taper trap to the flat trap and smoothly trapped in the flat trap, while the higher-energy ions, which are not well-cooled in the taper trap, are transported in and go out from the flat trap. It causes an efficiency loss.

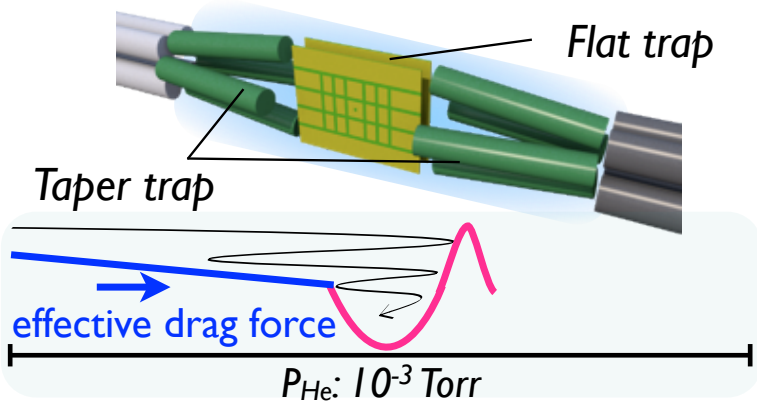

Figure 3.16: Schematic view of the dual-trap system. Two identical taper traps were installed on both side of the flat trap. Ions which have energies higher/lower than energy losses in the taper trap can be eventually trapped in the flat trap by the presence of the effective drag force.

In order to maximize the trapping efficiency, a dual-trap system were used as shown in Fig. 3.16. The taper trap was used as an auxiliary trap to accumulate and precool an ion bunch while an earlier bunch is being cooled in the flat trap, and to expand the trapping region of the flat trap during the first stage of cooling in the flat trap, thereby, it allows an operational duty cycle of ≈100%, with high efficiency.

3.3.1 Asymmetric taper trap

In the case of the symmetric taper trap, the ion envelope is symmetric near the boundary, while the flat trap entrance is not (see Fig. 3.17(a)). This can cause some ion loss at the interface with the flat trap during each back and forth pass. To avoid this, the inner shape of the taper trap was modified to be asymmetric as shown in Fig. 3.17(b).

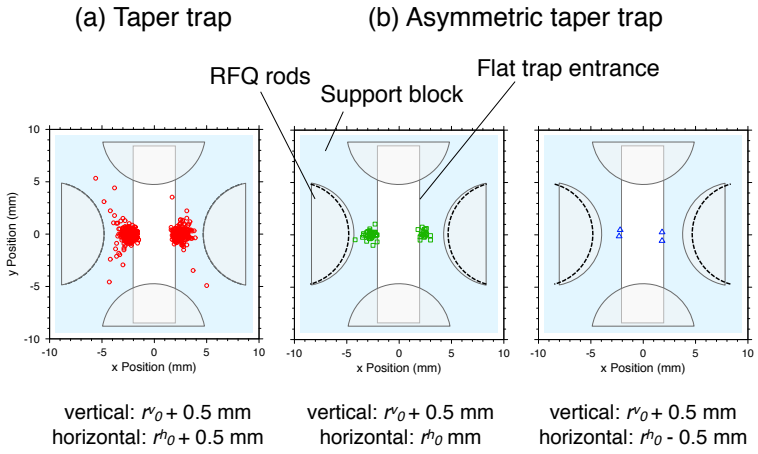

Figure 3.17: Cross-sectional views of the symmetric and asymmetric taper trap, and positions of ion losses at the front wall of the flat trap entrance. For all geometries, the inter-rod vertical gap is extended by $\Delta r_0 = 0.5$ mm. For horizontal gap, the symmetric taper trap has $\Delta r_0 = 0.5$ mm (left) and the asymmetric taper traps have $\Delta r_0 = 0$ mm (center) and 0.5 mm (right). The dashed lines indicate the position of $\Delta r_0 = 0.5$ mm. Ions lost by hitting to the front wall of the flat trap entrance, which is colored with light blue, are indicated.

This asymmetric geometry was investigated by simulation first. Figure 3.17 shows cross-sectional views of (a) the symmetric taper trap and (b) the asymmetric taper trap, and positions of ion losses at the front wall of the flat trap entrance. For all geometries, the inter-rod vertical gap is extended

by $\Delta r_0^{\mathrm{v}} = 0.5$ mm. For horizontal gap, the symmetric taper trap has $\Delta r_0^{\mathrm{h}} = 0.5$ mm (left) and the asymmetric taper traps have $\Delta r_0^{\mathrm{h}} = 0$ mm (center) and -0.5 mm (right). Ions lost by hitting the front wall of the flat trap entrance which is colored with light blue are indicated. For the symmetric taper trap, a lot of ions are hitting the wall horizontally, while for the asymmetric taper trap, a smaller amount of ions are hitting and only a few ions are hitting in the case of $\Delta r_0^{\mathrm{h}} = -0.5$ mm (right).

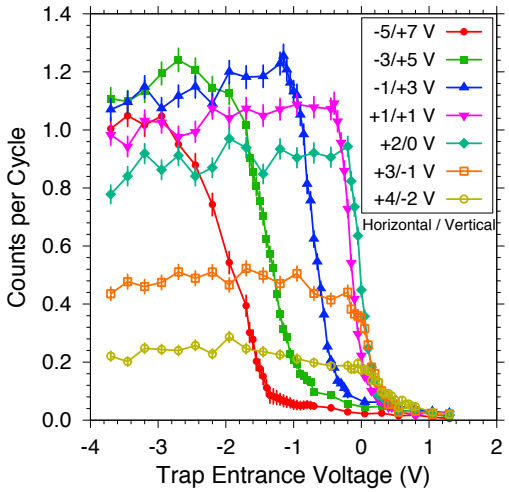

Figure 3.18: An example of the control of the potential gradient in the asymmetric taper trap. Ion rates were measured as a function of the trap offset voltage with various dc biases. The shift of rising positions indicate the average potential near the flat trap entrance is varied and the dependence of the ion rates maximum suggests the potential gradient is also changed.

An asymmetric geometry has an another feature. If unequal dc biases are applied to each pair of rods, the axial dc potential is changed from an symmetric geometry as described above. Thereby, the axial potential gradient in the taper trap can be controlled to some extent. Fig. 3.18 shows an example of the experimental verification of this effect. Incident ion energy at the flat trap is determined by the dc potential difference between the taper trap and the flat trap. In the result, the rising positions shift depending on the dc biases. That indicates the average potential of the taper trap is varied and the optimal trap offset voltage to trap ions in the flat trap also changes. Additionally, the dependence of the maximum ion rate suggests the potential gradient is also changed.

To optimize the geometry, the trapping efficiencies of various horizontal gaps, Δr_0^{h} using Na^+ ions were measured by adding spacer plates between the rods and the PEEK support block.. Prior to each efficiency measurements, the dc biases and the rf conditions were optimized, the gas pressure was set to $\approx$0.5 Pa in the flat trap, and the transmission efficiency for straight through the flat trap was measured.

To evaluate the transmission efficiency, the ion current at the taper trap, I_{taper}, located before the flat trap and at the RFQ ion guide, I_{RFQ}, located after the flat trap were measured (see Fig. 3.2). The transmission efficiency, $\epsilon_{\mathrm{straight}}$, was calculated as $\epsilon_{\mathrm{straight}} = I_{\mathrm{RFQ}}/I_{\mathrm{taper}}$ Figure 3.19 shows the result of the measurements. From the linear fitting of the data, the transmission efficiency of $\epsilon_{\mathrm{straight}} = 80(3)\%$ was obtained. In the following measurements of the trapping efficiency, the incoming ion rate measured at the axial CEM was normalized by the $\epsilon_{\mathrm{straight}}$.

The trapping efficiencies were evaluated in the same way as explained in Sec. 3.1.2. While operating at 100 Hz, ions were precooled and accumulated in the taper trap for 7 ms before being transferred to the flat trap. Cooling was performed in the flat trap for 3 ms. After the final cooling phase, ions were ejected from the flat trap and detected at the orthogonal CEM. While ions were cooling in the flat trap, new ions were also accumulating in the taper trap system.

The results are summarized in Table 3.1. The efficiency increases with decreasing horizontal gap. That is the same trend as expected from simulation. The efficiency reaches a maximum value of

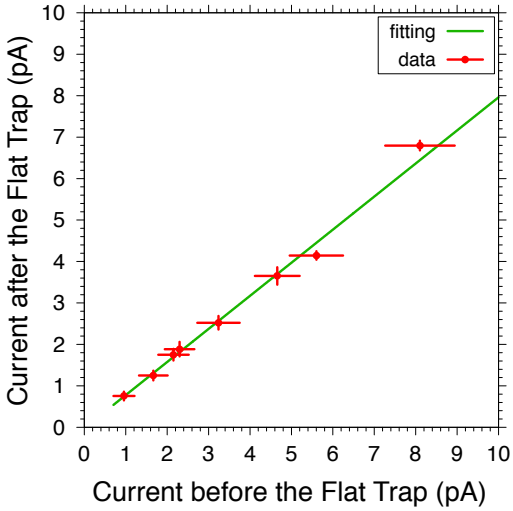

Figure 3.19: Transmission efficiency for straight through the flat trap. The ion current at the the taper trap located before the flat trap and at the RFQ ion guide located after the flat trap were measured. From the linear fitting of the data, the transmission efficiency of 80(3)% was obtained.

27% at $\Delta r_0^{\rm h} = -1.1$ mm and drops at $\Delta r_0^{\rm h} = -2.1$ mm to 5.4%. The reduction is explained by the quadrupole field distortion being too large to confine and transport ions stably, and the dc biases become too large for smaller $\Delta r_0^{\rm h}$ resulting in the ion heating.

Similarly to the measurement of Na^+, the trapping efficiency of $^7Li^+$ was also measured and an efficiency of 5.1% was obtained. The difference in efficiency between Na^+ and $^7Li^+$ is explained due to the mass difference which causes large momentum transfer in collision between $^7Li^+$ and helium atoms. This results in $^7Li^+$ being ejected from the rf pseudo-potential: often called "rf heating".

Table 3.1: Trapping efficiencies for various horizontal gaps, $\Delta r_0^{\rm h}$, using Na^+ ions. The vertical gap was fixed as $\Delta r_0^{\rm h} = 0.5$ mm.

$\Delta r_0^{\rm h}$ (mm)	$\Delta r_0^{\rm h}$ (mm)	Efficiency (%)	
+0.5	+0.5	12	symmetric
+0.5	0	19	horizontally in parallel
+0.5	−0.5	18	
+0.5	−1.1	27	
+0.5	−2.1	5.4	

The energy spread of uncooled ions entering the flat trap is estimated to be less than 10 eV, therefore higher-energy ions may turn back and leave the flat trap. By using the taper trap to extend the trapping region, ions can cross over the boundary between the flat and taper trap multiple times until the ion energy decreases enough to allow them to accumulate in the flat trap. Due to the effective trap drag force, ions cannot become trapped in the taper region during this "extended trap" phase. On the other hand, these traps can be used in dual-trap mode; the simulation is described in Fig. 3.20. The ions are first accumulated and precooled in the taper trap, then those well-cooled ions are transfered to the flat trap; the newly incoming ions (red line in Fig. 3.20) are trapped in this phase simultaneously.

The two operation modes were compared in terms of the efficiency with the parallel trap and the asymmetric taper trap optimized. Figure 3.21 shows the efficiency as a function of the offset voltage of the flat trap for each trap with transmission and trapping mode. In the transmission mode, ions were not precooled in the taper trap and were always trapped in whole region in the accumulation

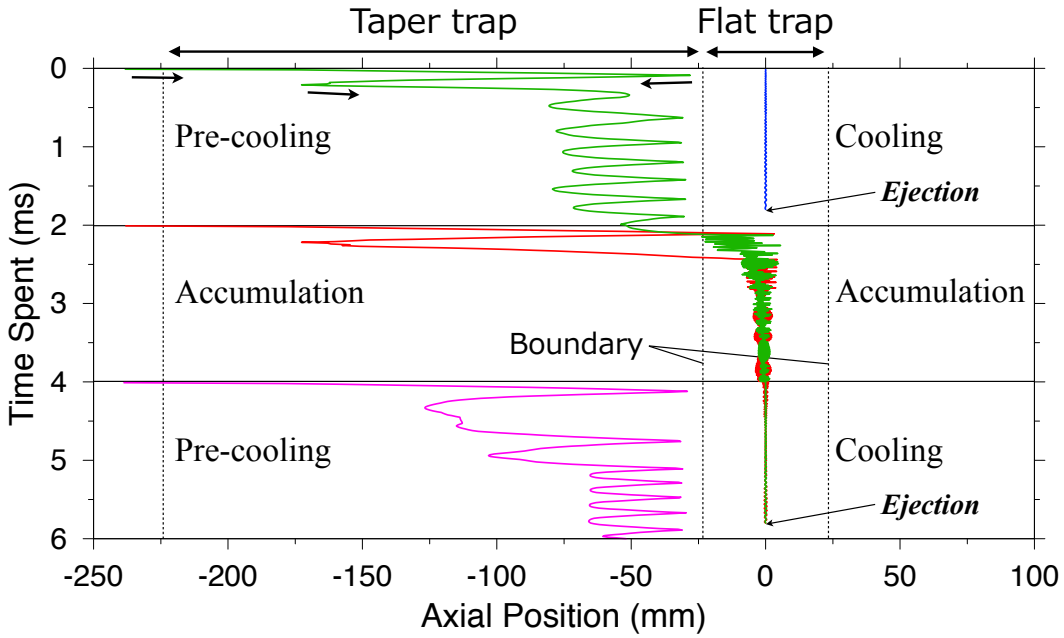

Figure 3.20: Schematic view of the dual-trap system. Two identical taper traps were installed both side of the flat trap. Ions which have energies higher/lower than energy losses in the taper trap can be eventually trapped in the flat trap by the presence of the effective drag force.

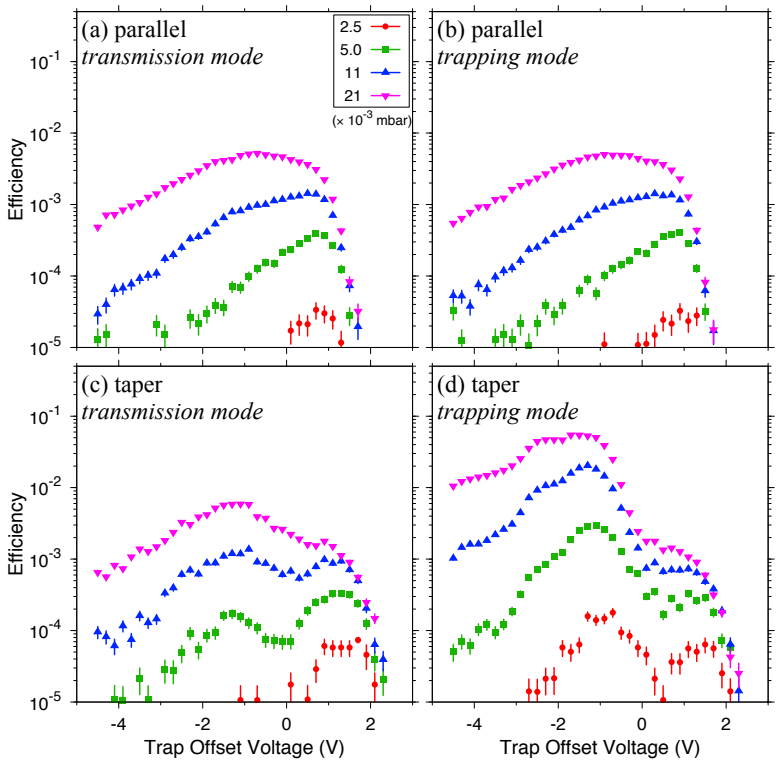

Figure 3.21: Trapping efficiency of $^{7}Li^{+}$ for the parallel trap in (a) transmission mode and (b) trapping mode, and for the taper trap in (c) transmission mode and (d) trapping mode.

phase. In the trapping mode, ions were precooled and accumulated in the taper trap for 7 ms before being transferred to the flat trap.

For the parallel trap, there is almost no gain between the two modes due to the absence of the drag force and well-cooled ions in the precooling don't contribute so much to the efficiency. It is consistent with the discussion so far.

The efficiency of the taper trap with the transmission mode also shows a low gain compared to the parallel trap with both modes, while with the trapping mode the efficiency is increased by an order of magnitude. In the transmission mode of the taper trap, higher-energy ions should cross over the boundary between the flat and taper trap multiple times until ions are accumulated in the flat trap, causing an efficiency gain. From these comparisons, it is assumed that the ion energy and emittance through the boundary are much higher than expected and such ion trajectories are disturbed and lost when ions cross over the boundary multiple times.

3.4 MRTOF

Our goal for the MRTOF has been to achieve mass resolving powers $R_{\mathrm{m}} > 100,000$. This requires determining, applying, and maintaining a proper set of bias voltages for the many electrodes.

For such requirements, simulations were first performed with ideal conditions, then optimal conditions were determined experimentally.

3.4.1 Simulations for MRTOF

Simulations were performed to determine an optimal bias distribution. Additionally, the simulations provided information on the error budget for the various biases. Of particular importance is the effect of slight errors in the various biases on the mass resolving power. Separately, since any real world measurements require some time, the mass resolving power could be reduced by dynamic shifts in the ToF due to fluctuations or drifts of the various biases. Important insight into these effects, provided by simulations, motivated decisions on how to implement the electrode bias system.

The evaluation of the MRTOF must begin with a comparison of calculated and experimental behavior. As part of the design procedure, many aspects of the MRTOF were simulated. As previously mentioned, the bias voltage distribution for the mirrors was optimized using a differential algebra-based routine. The differential algebra-based code does not calculate the ion trajectories, but calculates the electric potential on the flight axis and uses a differential algebra method to quickly (compared to *e.g.*, SIMION) calculate the ToF and ToF variance at a predetermined number of revolutions in the drift chamber, based on an assumed initial condition of the ion cloud in the rf trap. From the ToF and its variance, the mass resolving power is calculated and used by the code as a figure of merit for optimization of the electrode biases. The optimized values for a -5 kV drift potential with 518 revolutions, assuming an initial ion cloud of 500 μm rms radius at a temperature of $T = 300$ K, are given in Table 3.2.

The differential algebra code was also used to estimate the affect of small variations in the various voltages. Figure 3.22 shows the calculated affect of individual small deviations from the optimized electrode biases on the mass resolving power. Based on this result, relative errors of <50 ppm in any bias does not significantly reduce the achievable mass resolving power. The widths of the curves in Fig. 3.22, along with the affect of the bias variation on times of flight, are tabulated in Table 3.3. These results indicate that the resolving power is not adversely impacted by small deviations from the ideal voltages.

The differential algebra code, having the advantage of being rather fast, was well-suited for usage in calculating an optimized potential distribution. However, it has two short-comings: it could not calculate the peak shape, nor could it easily calculate affects of variation of the drift potential. For these reasons, a second code was used to verify the results of the differential algebra code. The IONFLY code [81] is an extension of SIMION with, among other features, improved Runge-Kutta

Table 3.2: Optimized MRTOF voltages from the differential algebra optimization code. Optimized for 518 revolutions with a drift potential of −5 kV. Initial condition of ion cloud was assumed to be $r_{\mathrm{rms}} = 0.5$ mm at $T = 300$ K.

Electrode	Bias (V)	Electrode	Bias (V)	Electrode	Bias (V)
ejL	−14350.35	inL	−5000	Drift	-5000
ej1C	2074.25	in1C	1115.52	A1	−1758
ej1O	−500	in1O	−1150	A2	−1150
ej2	−463.23	in2	−537.49	A3	−1150
ej3	414.78	in3	277.89	TrapP	300
ej4	−2356.60	in4	−5000	TrapN	−300
ej5	1048.58	in5	−5000		
ej6	−2841.95	in6	−5000		
ej7	−3381.23	in7	−5000		

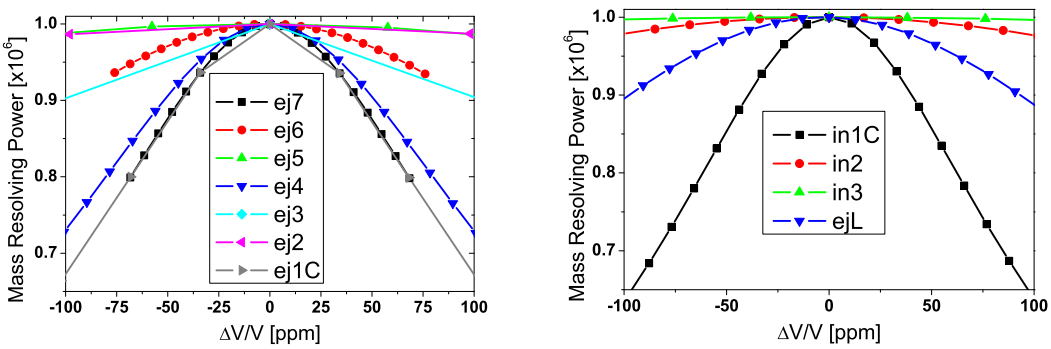

Figure 3.22: Calculated affects on mass resolving power from varying the bias voltages

Table 3.3: Calculated variation in R_{m} and ToF caused by variation in bias potential. FWHM(R_{m}) are given in ppm of voltage, while $\Delta t/\Delta V$ values are ppm/ppm.

Electrode	FWHM(R_{m})	$\Delta ToF_{\mathrm{DiffAlg}}/\Delta V$	$\Delta ToF_{\mathrm{IonFly}}/\Delta V$
ejL	430	−0.151	−0.032
ej1C	306	−0.193	−0.163
ej1O	–	–	1.7×10^{-3}
ej2	1657	−0.085	−0.076
ej3	744	−0.047	−0.052
ej4	255	0.026	0.021
ej5	1468	0.079	0.077
ej6	415	0.020	0.019
ej7	202	0.027	0.012
in1C	212	−0.260	−0.216
in1O	–	–	2.9×10^{-4}
in2	962	0.027	0.030
in3	2579	0.009	0.004
Drift	–	–	−0.265

routines for better calculation speed and accuracy. We decided to use it to verify the optimization and perform simulation studies that the differential algebra code was not capable of doing.

Using IONFLY with the optimized mirror potentials, the resolving power at 518 was found to be $R_{\mathrm{t}} \sim 10^6$. With this verified, the IONFLY code was used to verify the affect of bias variation on the times of flight. This was achieved by calculating the times of flight of 10 ions randomly selected from a "cloud" of $r_{\mathrm{rms}} = 0.5$ mm and $T = 300$ K, calculating the mean ToF, changing the bias potential and repeating. Linear fits to the data could then be made, as given in Table 3.3. In most cases, the agreement between the two calculations is quite good.

It is worthwhile to notice that the three largest $\Delta t/\Delta V$ values are for the mirror end caps (ej1C and in1C) and the drift potential. Since the end caps are switched and drift potential is also the next to lowest potential, after the out-sized lens (ejL) potential, it is reasonable to consider using the drift potential as a floating ground for the ensemble of MRTOF potentials. In this way, any change in the drift potential results in a uniform change of the entire MRTOF potential distribution. Effectively, changing only the kinetic energy of the ions injected into the reflection chamber. Since it is assumed that the mirror potentials are isochronous, this should not effect the time-of-flight or mass resolving power, at least not within some limited range.

As previously indicated, the code used to optimize the bias potentials was unable to provide information about the peak shape. The peak shape, however, is a very important quality. In particular, the better the peak shape is understood, the better the ToF can be determined by peak fitting. It was initially anticipated that the peak would be a Gaussian shape. The simulations, however, indicated that is was an asymmetric Gaussian shape, an example of which is provided in Fig. 3.23. It had previously been assumed that the slow-side tail seen in [54] was solely an effect of scattering. These simulations, however, indicated that the tail may actually be related to high-order optical aberrations.

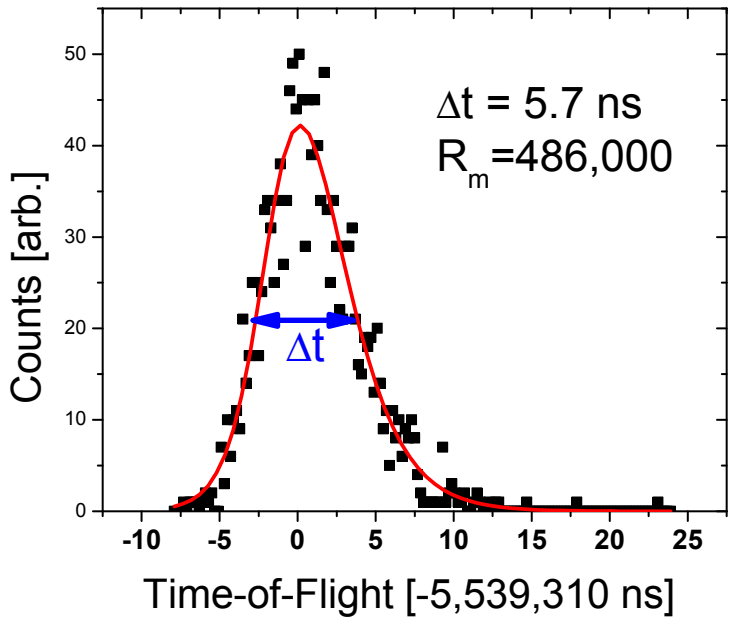

Figure 3.23: Calculated peak shape for ions with $A/q = 28$

3.4.2 Experiments for MRTOF

During initial commissioning of the MRTOF, it was found to be unable to hold the voltages required for 5 keV operation. With some effort, the structure eventually was able to hold voltages sufficient for 2 keV operation. The calculated optimal voltages were scaled down and a nearby optimum was found. As can be seen from Table 3.3, the bias potentials are very near to the calculated values. The mass resolving power achieved, $R_{\mathrm{m}} \approx 150,000$ is less than hoped by a factor of five, but still sufficient.

The various voltages of the MRTOF were scanned to experimentally determine the affect of the voltage variations. Figure 3.24 shows the resolving power as functions of the variation of bias voltages. These indicate that the calculation actually overestimated the affect of voltage variations on the resolving power. The resulting affect on the ToF is shown in Table 3.4, alongside the results of the IONFLY simulation. Despite the scaled down values, the agreement is remarkably good.

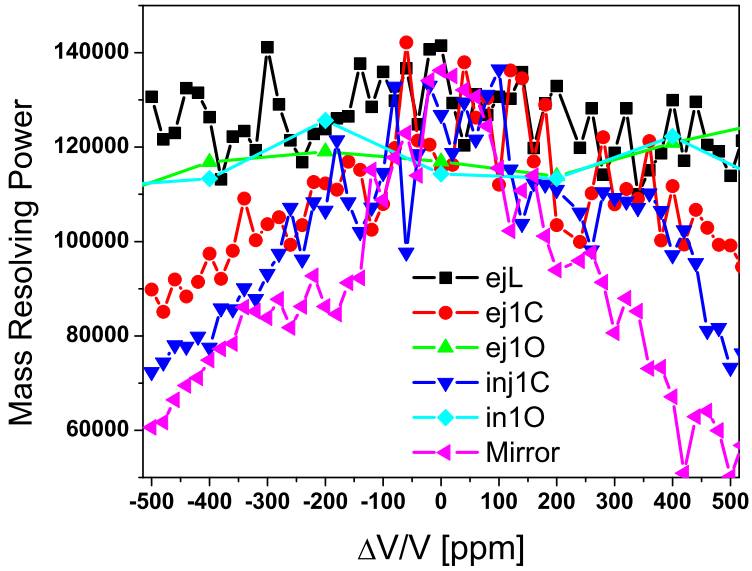

Figure 3.24: Measured affects on mass resolving power from varying the bias voltages

Table 3.4: Calculated and measured variation in ToF caused by variation in bias potential. All values are ppm/ppm

Electrode	$\Delta ToF_{\mathrm{Calc}}/\Delta V$	$\Delta ToF_{\mathrm{Exp}}/\Delta V$
ejL	-0.032	-0.038
ej1C	-0.163	-0.162
ej1O	1.7×10^{-3}	6.8×10^{-3}
Mirror	0.035	-0.087
in1C	-0.216	-0.221
in1O	2.9×10^{-4}	1.4×10^{-3}
Drift	–	7.7×10^{-4}

As the above results indicate, the achievable resolving power is limited by the stability of the applied biases. While the inherent resolving power is robust against small deviations from the optimum, the ToF can be strongly affected by small changes in the biases. To achieve the highest resolving powers, the voltages in the reflection chamber must be reasonably well maintained – in order to achieve $R_{\mathrm{m}} = 10^6$ requires, according to Table 3.3, that the all the biases are stable to $\Delta V/V \sim \pm 1$ ppm. To accomplish this, as has previously been discussed, a temperature regulated PID controller is used. The controller provides long-term stability on the order of $\Delta V/V \sim \pm 5$ ppm [82], sufficient to allow $R_{\mathrm{m}} \sim 200,000$.

The PID controller relies on voltage dividers and a high-precision voltage reference to monitor the applied voltages. Both the voltage divider, as well as the reference voltage, have some temperature dependence – 1 ppm/K for the voltage reference, 10 ppm/K for the ej1, ejL, and in1 voltage dividers, and <1 ppm/K for the mirror divider based on the manufacturer's data sheets. When these components suffer from thermal drift, the PID control system will incorrectly seem to be appropriately maintaining the voltages.

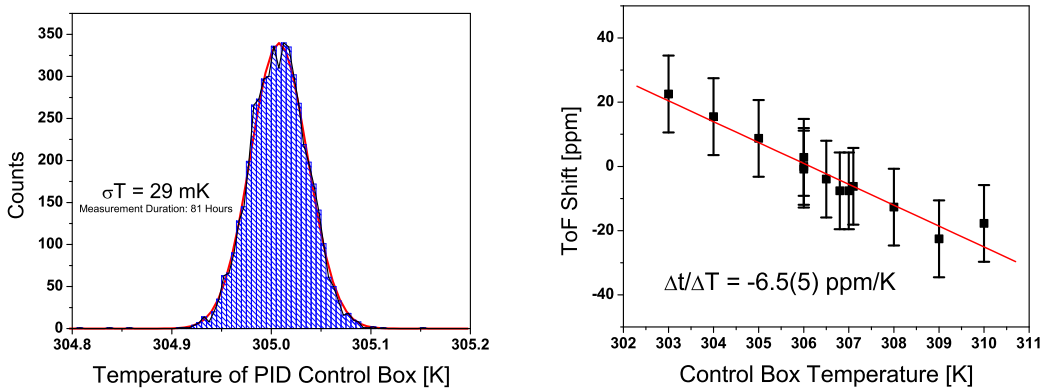

Figure 3.25: (left) The thermal stability of the PID controller was measured to be $\sigma T = 29$ mK. (right) The ToF drift caused by thermal fluctuations was measured to be $-6.5(5)$ ppm/K.

The magnitude with which this could effect the ToF spectrum depends on the net voltage drift as a function of temperature in combination with the level of thermal control which the PID controller can achieve. Figure 3.25(left) demonstrates that the PID thermal controller can obtain a longterm stability of $\sigma T \sim 29$ mK. The magnitude of the temperature effect on the ToF was checked to validate the sufficiency of the thermal stabilization of the PID controller system. To determine the thermal response of the PID controller, $^{39}K^{+}$ ions were analyzed with a mass resolving power of $R_{\mathrm{m}} \sim 100,000$. The setting of the temperature controller was changed and allowed to come to equilibrium, determined by waiting for the ToF peak to cease drifting after the change of the temperature controller. Between consecutive measurements, the temperature was returned to 306 K to ensure the observed drift was only related to the temperature of the PID controller. The result, shown in Fig. 3.25(right), is that a 1 K change in the temperature of the PID control box produces a 6.5 ppm shift in the ToF. The measured temperature stability therefore corresponds to a ± 0.19 ppm fluctuation in the ToF. As the period of the thermal fluctuations is on the order of minutes, this fluctuation mostly results in a slight broadening of the ToF peak for longterm measurements, but may still lead to undesirable shifts in the case of short duration data acquisition.

The PID controller is not the only possible source of thermal effects. The MRTOF is supported on a large Titanium structure. While it is designed to be bakeable, the structure is too massive to be reasonably thermally stabilized. As such, effects from thermal expansion and contraction should be expected.

A PT100 thermistor attached to the Titanium support bracket allows monitoring of the temperature of the structure. Because the structure is too large to thermally regulate, the effect of thermal expansion was investigated by baking the vacuum chamber at 60 °C and then turning off the baking. The structure quickly cooled to ∼45 °C. Because its only thermal contact is on the injection-side of the MRTOF, during the rapid cooling it is assumed the Titanium support structure had a large temperature gradient across its length. However, cooling from 45 °C down to room temperature occurred over the course of several hours, during which the Titanium support structure may be assumed to have only a small temperature gradient across its length. The ToF as a function of temperature during this period is shown in Fig. 3.26(left).

The evaluated effect of thermal expansion, $\Delta t/t \cdot K = 4.9$ ppm/K, is comparable to the 8.6 ppm/K thermal expansion coefficient of Titanium, perhaps reduced slightly by the isochronous nature of the electrostatic mirrors. This indicates the importance of monitoring, if not regulating, the temperature of the MRTOF bulk structure – a 0.2 °C change in the temperature between measurements could lead to a 1 ppm deviation in the measured mass.

Figure 3.26(right) shows the long term stability of the measured ToF over the course of two days. As can be seen, there are long durations with no ToF shift as well as durations when the ToF drift is $\approx 3 \times 10^{-7}$/hr. The longest duration of drift, leading to a 4 ppm shift in the ToF, is consistent with an increase in the bulk temperature of $\Delta T \approx 0.8$ °C over the course of 12 hours.

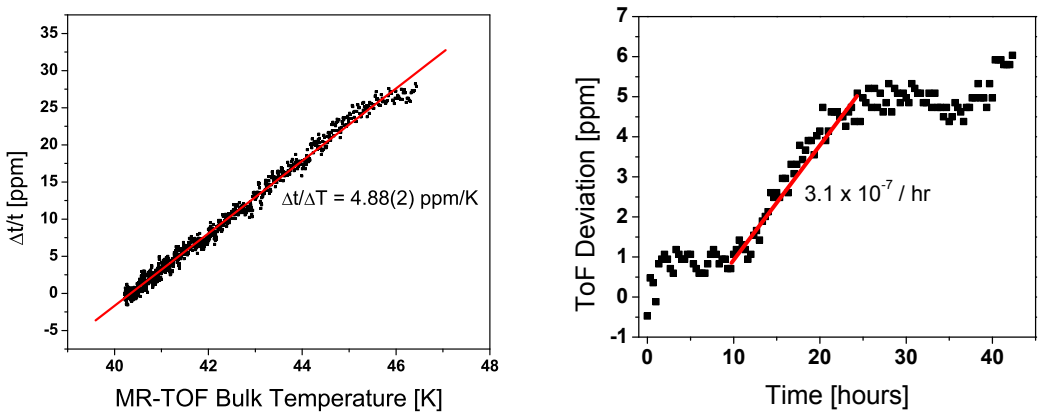

Figure 3.26: Effects of thermal expansion on the ToF. (left) Measured effect of thermal expansion on the ToF. (right) Long-term stability of the MRTOF. The fast component is consistent with thermal expansion from a 0.8 °C increase in the temperature of the MRTOF.

3.5 RF-carpet ESI

An electrospray ionization (ESI) ion source has possibility to provide a wide variety of molecular ions simultaneously and in almost all species isobars exist. That is a main reason to develop as a reference ion source for MRTOF mass measurements. Additionally, an rf-carpet technique developed in our group can replace a conventional skimmer system without a large amount of transmission loss. The performance of an ESI ion source with an rf-carpet is experimentally detailed below.

3.5.1 Production of wide-mass ions

As introduced in Sec. 2.6.2, between the lack of atomic reference ions above $A/q = 209$ and lack of a flexible all-purpose method for ionizing most elements, an ESI ion source can be the best solution to produce reference ions. The ESI can produce a wide variety of molecular ions simultaneously from a combination of solute and solvent.

Prior to testing with the MRTOF, the ESI part was tested with a commercial mass spectrometer, the Shimadzu 2020MS quadrupole mass spectrometer, at NMSU. A sample of Reserpine was dissolved in a solvent of Methanol:Water = 1:1 with Formic acid as a proton donor to a concentration of 5 ppm. A clear strong peak of $m/z = 609$ u was found and it was identified as Reserpine with proton as shown in Fig. 3.27(top). This confirmed that our ESI works in general usage.

Next, the ion production in the region of nuclear mass measurements was tested without any sample. The ions were produced from the solvent and contaminants by making adduct clusters. Over the region, a lot of peaks were confirmed with various yields as shown in Fig. 3.27(middle). The peaks were found over almost all mass numbers as shown in Fig. 3.27(bottom). This result satisfies our requirements for using as a reference ion source.

3.5.2 The RF-carpet ESI

To test with the MRTOF system, the ESI was combined with an rf-carpet and connected to the MRTOF system as shown in Fig. 2.10. To produce molecular ions with the ESI, first a solution is prepared with a specific sample in a solvent with a trace of formic acid being added to favor positively charged ions. In this work, we used three different solutions as listed in Table 3.5. The solution is pushed into the ESI capillary by a motor driven syringe pump. A voltage of 2-5 kV is applied between the ESI capillary and the transport capillary, which are separated from each other by 10-30 mm. Due to this short distance, the electric field is as high as 10^6 V/m. The molecules are polarized near the exposed surface, which forces the liquid to point downfield and form a so-called Taylor cone [83, 84]. Near the tip of the Taylor cone the repulsion between positive charges at the surface

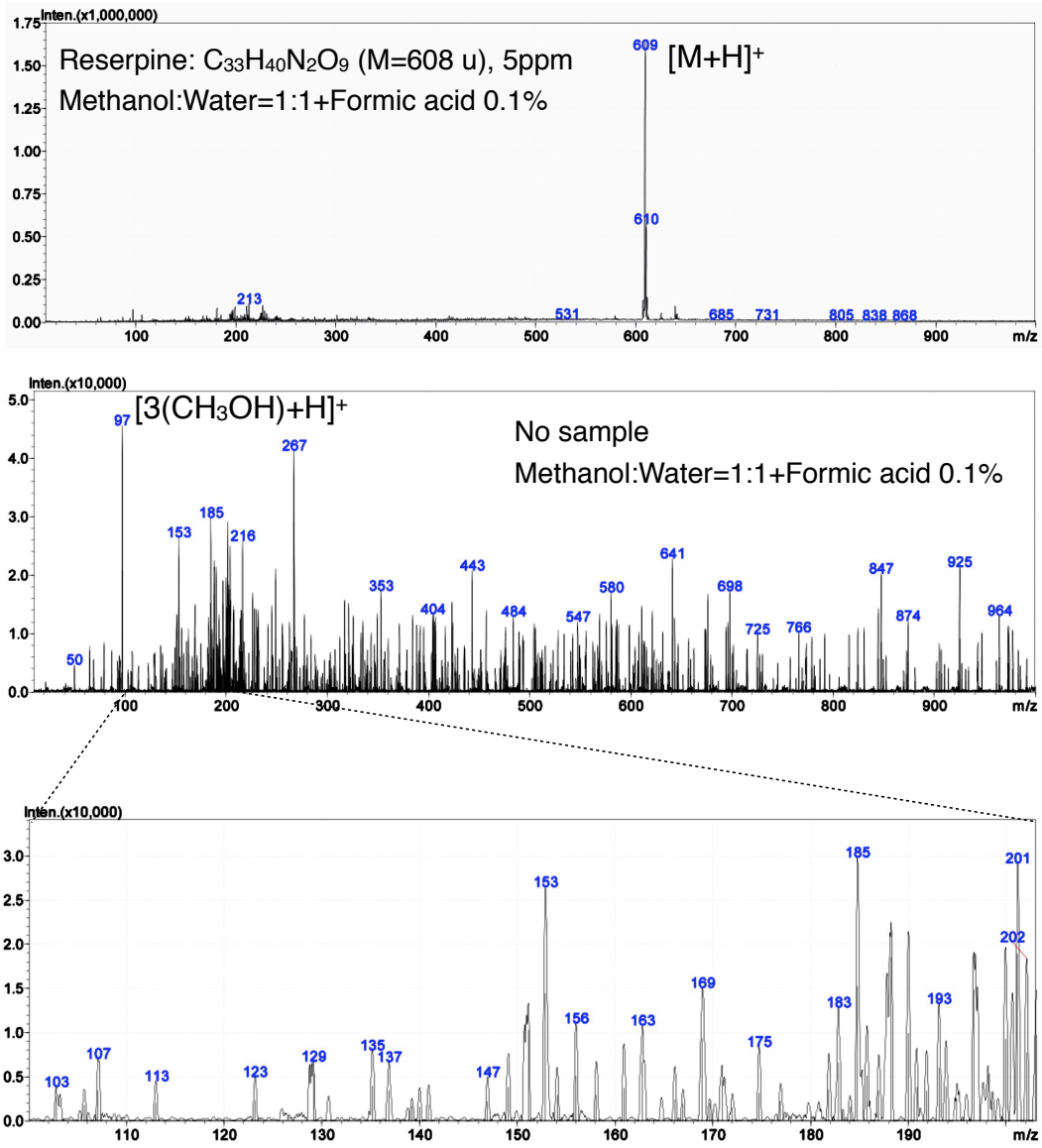

Figure 3.27: Mass spectra of the ions from ESI measured with the Shimadzu 2020MS quadrupole mass spectrometer. In general usage, a sample, for instance Reserpine, is ionized and makes a single strong peak (top), while for our purpose, a sample is not alway used but solvent clusters and contaminants are useful (middle). Over the region of interest for nuclear mass measurements, the peaks are made with various yields (bottom).

increases, causing instabilities which form droplets with approximately the same size as the cone's tip. The charged droplets evaporate while drifting toward the transport capillary; the droplets shrink while preserving the charge. At a certain radius, known as the Rayleigh limit [85, 86], the strong repulsion between charged ions overcomes the surface tension and Coulomb fission of the droplet occurs. Coulomb explosions leads to a jet of ever smaller charged droplets, which undergo cycles of evaporation and Coulomb fission until the droplets are small enough that ion evaporation occurs, forming gas-phase ions [87]. Gas flow forces transport the ions into and the through the transport capillary.

Table 3.5: Solutions used for the production of molecular ions by the ESI. Each solution is prepared by dissolving a sample in solvent (CH_3OH or C_2H_5OH) and formic acid (HCOOH) mixture. The amount of sample is chosen to provide the desired concentration (conc.) in the solvent. Concentrations of formic acid are on the percentage level of the total solution.

Sample	Conc. (ppm)	Solvent	Formic acid
$C_6H_8O_7$	200	CH_3OH	0.1%
$C_{17}H_{21}NO{\cdot}HCl$	100	CH_3OH	0.1%
No sample	–	C_2H_5OH	10%

In conventional ESI systems, a skimmer is placed behind the transport capillary where a potential difference is applied to pull ions to the high vacuum region. In our system, we replace the skimmer with an rf-carpet. Just as for the skimmer, an electric field transports ions to the rf-carpet, where they hover above the surface due to an inhomogeneous rf electric field, then they are driven by a dc electric field towards the rf-carpet exit hole of 0.5 mm diameter.

The rf-carpet consists of a planar printed circuit board with 54 ring electrodes, each 0.15 mm with a pitch of 0.3 mm as shown in Fig. 2.11. An rf amplitude of up to 300 V_{pp} has been applied between neighboring electrodes with a frequency up to 4 MHz, while a dc gradient of less than 3 V/mm has been superposed between the outmost ring and the center. The gas pressure in the rf-carpet chamber is about 4 mbar, while in the second chamber the pressure is on the order of 10^{-4} mbar. The residual gas is mainly air since the ESI system is placed in air. When ions reach the rf-carpet exit hole, they are pulled into the second chamber, where a rf quadrupole (RFQ) ion guide transports the ions and a mass separator (QMS) provides an initial mass selection.

3.5.3 The RF-carpet characteristics

An electric field transports the ions from the edge of the transport capillary to the rf-carpet. The ions are repelled from the rf-carpet surface by an inhomogeneous rf electric field and a dc electric field drives them toward the rf-carpet exit hole. According to the well-known Mathieu's equation, the ion motion is stable within a limited parameter space of dc and rf amplitudes. For the rf-carpet, the gas pressure must also be taken into account to find the stability region, which is determined by the two dimension-free parameters $(a - p^2)$ and q defined as

$$a - p^2 = \left(\frac{2eU}{mr_0^2\omega^2}\right) - \left(\frac{e}{m\mu\omega}\right) \tag{3.3}$$

$$q = \frac{4eV}{mr_0^2\omega^2}, \tag{3.4}$$

where e, m and μ are the electric charge, mass ans mobility of an ion, respectively, and U, V and ω are the dc-, rf-amplitudes and the angular frequency applied between adjacent electrodes, respectively. r_0 is related to the distance between adjacent electrodes. The inhomogeneous rf electric field can be described by electric pseudo-potential wells with a maximum average effective force approximated in

high pressure by [25]:

$$\bar{F}_{\mathrm{hp}}^{\max} = -\frac{1}{4} m\mu^2 \frac{V^2}{r_0^3}. \tag{3.5}$$

The rf-carpet pseudo-potential makes a corrugated shape, with the troughs being centered on the electrodes. In order for the pseudo-potential approximation to be valid, an ion must spend several oscillations of the field in the vicinity of a single trough. Efficiently transporting ions to the rf-carpet exit hole by having the required pseudo-potential depth makes the pressure, dc and rf electric fields critical parameters for stable ion motion.

To illustrate the characteristics of ideal transport for a particular mass, we performed tests at 4 mbar of gas pressure for low- and high-frequency rf electric fields, varying the rf and dc voltages applied to the rf-carpet ring electrodes. The dc voltage, V_{dc}, is the voltage applied between the outer and the central electrodes, where U in Eq. 3.4 can be deduced from V_{dc} [25]. The ions were detected behind the MRTOF after a single pass (without reflections). The time-of-flight (ToF) spectra obtained are shown in Fig. 3.28. The rf-carpet was tuned to ideal conditions for the transmission of light and heavy ions. By tuning the rf-carpet parameters (frequency, V_{rf} and V_{dc}), a mass range can be chosen as seen in Fig. 3.28, where low mass ions ($m/z < 150$) are drastically reduced when the rf-carpet is set for the transmission of heavy ions. Fig. 3.29 shows the ion intensity for particular examples; $m/z = 50$, 150 and 260 from Fig. 3.28, as a function of rf and dc voltages for frequencies of 4 MHz and 1.6 MHz. The ion intensity of low mass ions ($m/z = 50$) decreases at lower frequency, while for high mass ions low-frequency is still sufficient to guide ions to the rf-carpet exit hole. Higher rf frequency requires greater rf amplitude. Low mass ions require much higher rf amplitude than high mass ions at the same frequency.

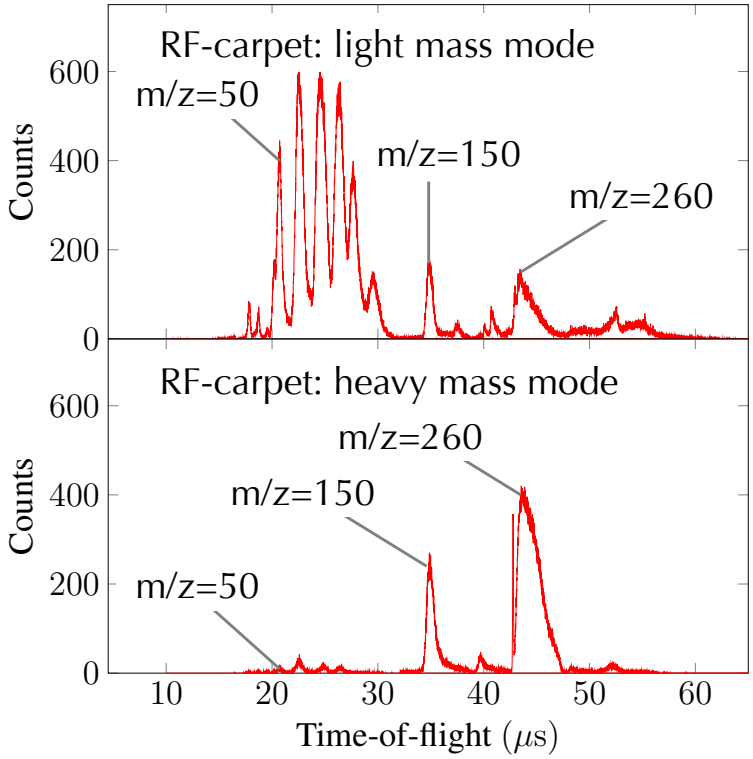

Figure 3.28: Time-of-flight from the trap to the MCP detector behind the MRTOF without any reflections. (Top) rf-carpet tuned for light ions transmission (4MHz, $V = 220$ V, $U = 60$ V). (Bottom) rf-carpet tuned for heavy ions transmission (4 MHz, $V = 60$ V, $U = 20$ V).

Typically, molecular species with low masses have higher mobility than molecular species with higher masses, thus for low frequency they may move between electrodes in less than a few rf periods

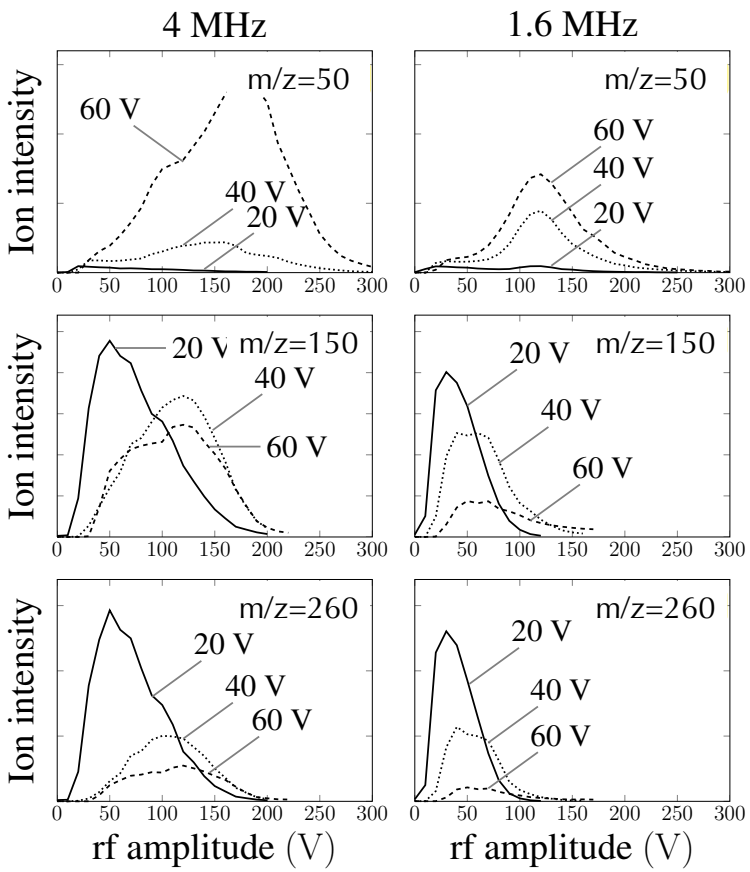

Figure 3.29: Ion intensities for various masses and various dc voltages as functions of the rf amplitude applied to the rf-carpet

making the pseudo-potential approximation invalid. Therefore, at low frequency, lighter ions may have unstable motion and could be lost before reaching the rf-carpet exit hole, while the motion of heavier ions is slower where the pseudo-potential approximation is still valid, allowing stable motion. At the higher rf amplitudes required for light ions, the pseudo-potential well becomes deep, therefore higher dc voltage is required for lighter ions to prevent them from being trapped. However, the dc voltage should not be so large as to cause unstable ion motion.

To efficiently transport low mass ions with the rf-carpet, higher frequency and higher dc and rf voltages are required. Higher mass ions can be transported using considerably lower frequency, dc and rf amplitudes.

3.5.4 The RF-carpet performance

In order to test the efficiency of the rf-carpet, we compare the current impinging on the carpet with the current extracted from the carpet. The impinging current was determined by utilizing the carpet itself as a Faraday cup. The current extracted from the rf-carpet was determined by utilizing the QMS as a Faraday cup. For this purpose, a solution of methanol and water with a ratio of 1:1 with formic acid (0.1% of the total volume) was used. Part of the large variety of molecular ions produced from this solution is shown in Fig. 3.27(middle), which was measured using the Shimadzu 2020MS placed behind the ESI system. The observed ion current behind the rf-carpet was ≈15% of the total ion current observed before the rf-carpet, with the rf-carpet tuned for low mass region. Considering the rf-carpet's limited mass bandwidth and the wide-band production of the ESI, we believe the true transmission efficiency is near unity.

3.5.5 Analysis of heavy molecular ions with the MRTOF

Once the ideal rf-carpet conditions are found, ions are stored in the rf ion trap and transferred to the MRTOF to fly for a time sufficient to separate molecular ions by mass. The time between consecutive reflections in a given mirror (one revolution) can be determined for a known reference ion and scaled for a given ion of interest. For this purpose, $^{85}Rb^+$ ions from the alkali ion source placed on the other side of the rf ion trap were used as a marker for low mass ions. For higher mass ions, $C_{17}H_{21}NOH^+$ ions from the solution prepared with diphenhydramine hydrochloride ($C_{17}H_{21}NO{\cdot}HCl$) as listed in Table 3.5 were used as a marker. After a certain number of reflections, the peak width is minimum – the time focus condition. Thus, the total time-of-flight can be written as:

$$t = t_0 + nT, \tag{3.6}$$

where n is the number of revolutions of the ions of interest, T is the time of one revolution and t_0 is to the first order the single pass ToF. In a given electrostatic field, light ions fly faster than heavier ions. Ions with slightly different masses stored for the same time (nT) will have different ToFs. Ions with sufficient mass difference may come at different number of revolutions, with heavy ions making lower number of revolutions than lighter ions. A typical ToF spectrum at the time focus condition is shown in Fig. 3.30, where $m/z = 93$, 94 and 95 isobars are well separated.

The ToF peaks were fitted with a Gaussian function by means of least-square approach to obtain the mean ToFs and their uncertainties. Figure 3.31 shows an example of a ToF peak of $m/z = 243$ with the fitting function. Further details concerning the fitting function of the ToF peaks will be discussed elsewhere. Some examples of the results are given in Table 3.6, where molecules with $m/z = 243$, 244 and 245 could be used as references for the mass measurement of trans-uranium elements $^{243-245}$Np, ^{243}Cf, $^{243-245}$Es, $^{243-245}$Fm and ^{245}Md, which have half-lives of a few milliseconds to minutes. A mass resolving power of $R\mathrm{m} \approx 100\,000$ could be achieved in 13-20 ms. This resolving power could be preserved for heavier masses. Due to this high resolving power, the molecular ions from the new ESI ion source could be unambiguously identified even for less abundant molecules as it is the case of $^{13}CC_4H_6N_2^+$(∼5.4% natural abundance).

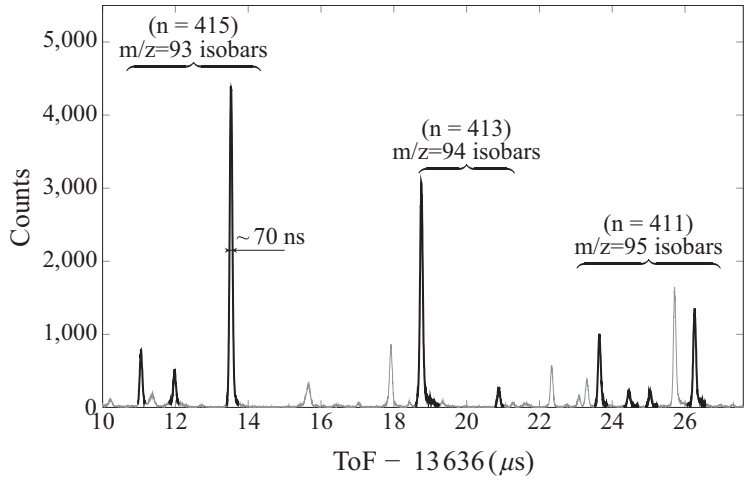

Figure 3.30: ToF spectrum of ions from ESI after a storage time of 13 629 μs. The spectrum was obtained from the ethanol solution as listed in Table 3.5. The m/z = 93, 94 and 95 isobars are well separated. Non highlighted peaks in the ToF spectrum are lighter or heavier molecular ions that come at much higher or lower numbers of revolutions in the MRTOF.

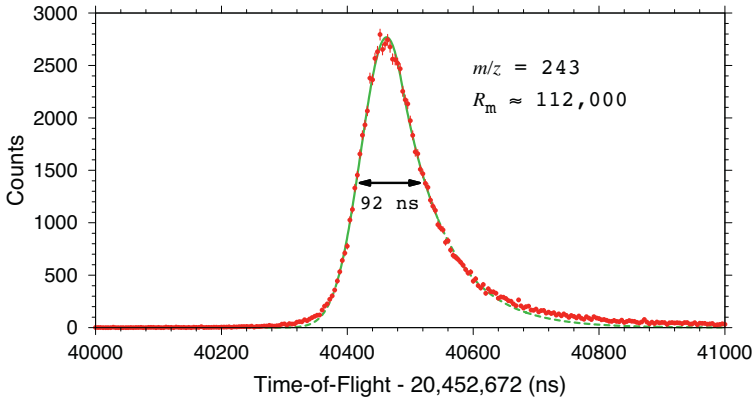

Figure 3.31: ToF peak of m/z = 243 fitted as a Gaussian with an exponential tail.

Table 3.6: Time-of-flight, peak width and the mass resolving power obtained for various molecules from the molecular ion source. The peak width Δt is the FWHM of the Gaussian fit.

m/z	Molecules	Time of flight (ns)	Δt (ns)	R_m
95	$C_5H_5NO^+$	13 626 528.8(0.3)	70	97 000
	$C_4H_5N_3^+$	13 627 327.0(0.6)	62	110 000
	$^{13}CC_4H_6N_2^+$	13 627 916.1(0.6)	71	97 000
	$C_6H_9N^+$	13 629 136.0(0.3)	67	102 000
243	$C_{12}H_9N_3O_3^+$	20 493 142.0(0.5)	92	112 000
244	$C_{12}H_{10}N_3O_3^+$	20 482 317.1(1.8)	120	86 000
245	$C_{10}H_5N_4O_4^+$	20 469 137.7(1.4)	103	99 000
	$C_{12}H_{11}N_3O_3^+$	20 471 084.7(3.1)	138	74 000

4 Online studies

To verify the performance of the MRTOF and the preparation traps with unstable nuclei, commissioning was performed by coupling them to the prototype SLOWRI system. The prototype SLOWRI system was designed for lighter nuclei, such as Li or Be. The performance for such lighter nuclei has been previously investigated via Be laser spectroscopy [63]. The easiest case was chosen for the commissioning experiment – the unstable nucleus ^{8}Li.

In the commissioning experiment, the trapping efficiency of $^{8}Li^{+}$ and the times-of-flight of $^{8}Li^{+}$ along with those of stable $^{7}Li^{+}$ and $^{9}Be^{+}$ were measured. In the analysis of atomic mass, a new analysis method, which we refer to as the "single-reference method", was adopted. The online experimental setup consisted of a gas cell filled with 20 mbar He gas, an rf-multipole transport system, buffer gas-filled ion trap, MRTOF, offline ion source and detector suite, as shown in Fig. 2.12.

^{8}Li ions were produced by projectile fragmentation of a 100A MeV primary beam of ^{13}C on a 1.86 g/cm^2 Be production target. Our desired nuclei, ^{8}Li, was selected by the RIPS projectile fragment separator [11] and transported to the prototype-SLOWRI branch, where the high-energy ions were first decelerated by a wedge-shaped energy degrader before being stopped in the gas cell. The ^{8}Li ions were extracted as $^{8}Li^{+}$ by an rf-carpet system [25, 62] and transported to high vacuum by an octupole ion guide (OPIG) made of resistive carbon fiber reinforced plastic which allows simple production of an axial drag force [26]. Stable ions produced in the gas cell could be largely eliminated by an rf quadrupole mass separator (QMS). The $A/q = 8$ beam comprised $^{8}Li^{+}$ and a small amount of $^{4}He_2^{+}$ produced in the gas cell.

4.1 Trapping efficiency with ^{8}Li

It is important to measure the trapping efficiency of the preparation traps not only offline, but also online. Doing so allows verification that there are no unintended potential wells in which ions can be inadvertently trapped. Using stable ions, the existence of such undesired features, in which ions could be delayed for long durations, can be difficult to determine. Initial conditions of the ions, for instance mean energy, energy spread and contaminants, are well-determined and often optimum offline, while they have a complicated relationship to the upstream conditions of the gas cell, the OPIG, the QMS and so on. Using ^{8}Li has a particular advantage for the efficiency evaluation online. ^{8}Li, with the half-life of $T_{1/2}$ = 840 ms, decays into ^{8}Be which immediately decays into two α particles with an energy of ≈1.5 MeV each. If ^{8}Li is implanted in a silicon detector (SSD) the α particle detection efficiency should be ≈100% and ^{8}Li ions can, additionally, be uniquely identified from their half-life.

In order to determine the efficiency, we must first determine the incoming rate of $^{8}Li^{+}$. This is complicated by the existence of a large fraction of unstopped light energetic particles ($^{1-3}$H, ^{3,4}He, etc.) which can not be removed by the D1 magnet and pass through to the detector. Therefore, the rate is determined by pulsing the beam from the cyclotron. To make the measurement maximally consistent with offline studies the decays are measured on an SSD after the trap system.

The beam was pulsed with a 2 s cycle where the beam on duty cycle was 33%. As shown in Fig. 4.1, this results in a fair amount of detected decays in any given cycle belonging to ^{8}Li which accumulated in previous cycles, complicating the analysis of the rate. The rate was determined by taking this into account as follows.

The number of ^{8}Li which accumulate on the SSD after $T_{\rm on}$ is given by

$$N_0 = \tau I_0 (1 - e^{-T_{\rm on}/\tau}) \tag{4.1}$$

where τ and I_0 are the lifetime and incoming rate of ^{8}Li. The number of those which decay in the subsequent duration T_{off} is then

$$N_{\text{d}} = N_0 \left(1 - e^{-T_{\text{off}}/\tau}\right). \tag{4.2}$$

The number of ^{8}Li on the SSD at the beginning of the n^{th} decay measurement cycle is then given by

$$k = 0 : N_k = N_0 \tag{4.3}$$
$$k = 1 : N_k = N_0 + N_0 e^{-T/\tau} \tag{4.4}$$
$$k = 2 : N_k = N_0 + N_0 e^{-T/\tau} + N_0 e^{-2T/\tau} \tag{4.5}$$
$$\vdots$$
$$k = n : N_k = N_0 \sum_{k=0}^{n} e^{-kT/\tau} \tag{4.6}$$

where T is the cycle time of 2 s. From Eq. 4.2 we can then write that the total number of detected decays after n cycles can be given by

$$N_{\text{d}}^{\text{tot}} = \sum_{l=0}^{n} \left\{ N_0 \sum_{k=0}^{l} e^{-kT/\tau} \left(1 - e^{-T_{\text{off}}/\tau}\right) \right\} = N_0 \left(1 - e^{-T_{\text{off}}/\tau}\right) \sum_{l=0}^{n} \sum_{k=0}^{l} e^{-kT/\tau} \tag{4.7}$$

However, since the fraction of ^{8}Li which remains after more than 3 cycles is minuscule, the terms of $k > 3$ can be neglected. Hence, assuming that the rate I_0 is relatively constant, the sum can then be written as

$$N_{\text{d}}^{\text{tot}} = N_0 \left(1 - e^{-T_{\text{off}}/\tau}\right) \left\{ n + (n-1)e^{-T/\tau} + (n-2)e^{-2T/\tau} + (n-3)e^{-3T/\tau} \right\} \tag{4.8}$$
$$= \tau I_0 (1 - e^{-T_{\text{on}}/\tau}) \left(1 - e^{-T_{\text{off}}/\tau}\right) \sum_{m=0}^{3} (n-m) e^{-mT/\tau} \tag{4.9}$$

where it has been accounted for that the first three cycles have less than three preceding cycles.

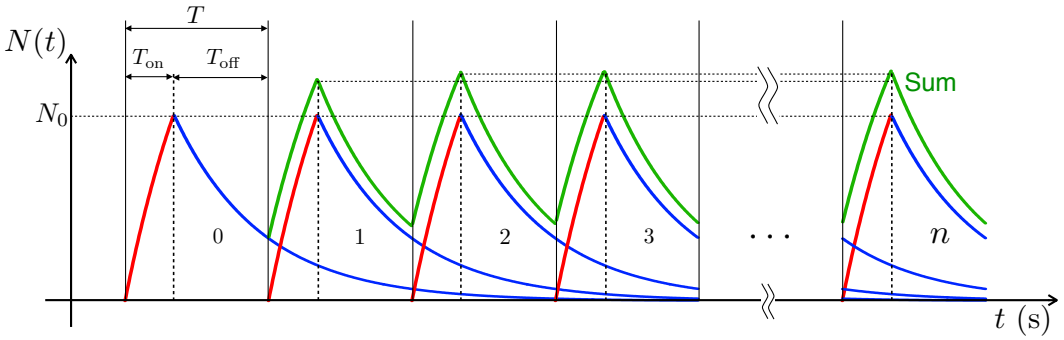

Figure 4.1: Experimental scheme of the ^{8}Li decay measurement. For the cycle n, the calculated decay counts of remaining ^{8}Li which are implanted in previous cycles contribute to the detected counts. The fraction of ^{8}Li which remains after more than 3 cycles is minuscule.

The efficiency measurement was performed in the same way as offline measurements, except with a different detector. The CEM detector was replaced by an SSD, which was referenced to a virtual

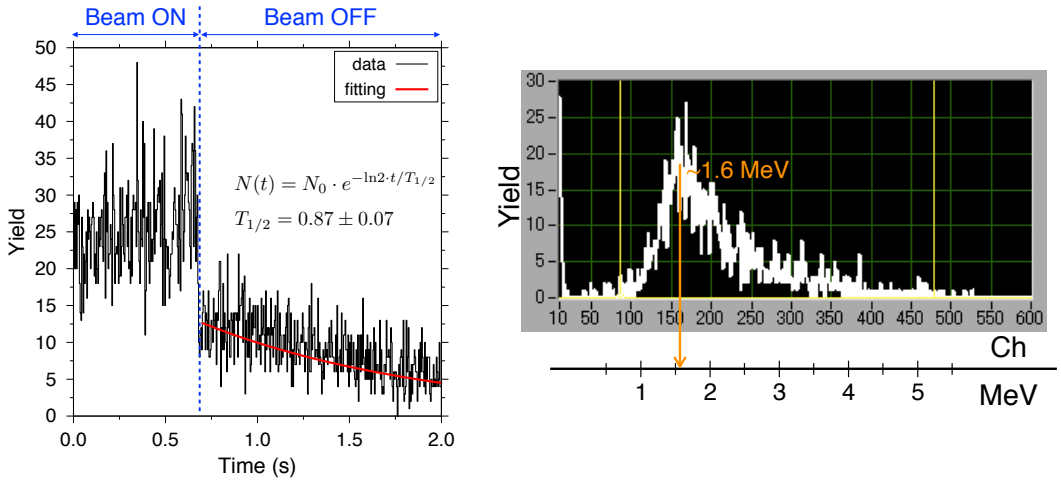

Figure 4.2: (left) A typical decay time spectrum of ^{8}Li with fitting of the decay function. The obtained half-life of $T_{1/2} = 0.87 \pm 0.07$ s agrees with literature value of $T_{1/2} = 0.84$ s. (right) A typical decay energy spectrum of α particle of ^{8}Li.

ground at -150 V in order to implant the ions. A pulsed $^{8}Li^{+}$ beam was delivered by chopping the beam prior to the cyclotron accelerator. Decay measurements were performed with a chopping rate of 0.5 Hz and Duty cycle of 66%. Decay time and energy spectra were obtained using the SSD as shown in Fig. 4.2. The beam was delivered for 0.68 s, then stopped for 1.32 s when decay measurements were performed.

The values needed to calculate I_0 were $T = 2$ s, $T_{\rm on} = 0.68$ s, $T_{\rm off} = 1.32$ s, $T_{\rm daq} = 454$ s, $n = 454/2 = 227$, $N_n^{\rm tot} = 1984$ counts, $\tau = T_{1/2}/\ln 2 = 1.21$ s. From Eq. 4.9 using these values, the beam rate was determined to be $I_0 = 21$ cps.

The rate of trapped ions was measured at the MCP at the end of the MRTOF after the ions performed $N = 880$ laps. Figure 4.4 shows a typical time-of-flight spectrum with an integrated count rate of ≈0.26 cps after the same measurement duration as the decay measurement. After $N = 880$ laps, the count rate at the MCP is known to be reduced by half compared to the rate with no reflection, due to collisions with residual gas. Therefore, a count rate of 0.52 cps was used for the efficiency calculation to make it consistent with offline measurements. From these numbers, the trapping efficiency for ^{8}Li was evaluated to be 2.5%, which is consistent with the efficiency for ^{7}Li of 2.5%.

The efficiency for conversion of a 1 GeV ^{8}Li beam to a continuous 5 eV beam by a 2-m-long gas cell with an rf-carpet ion guide was ≈5% [62] and the trapping efficiency for the 5 eV continuous beam was 2.5%. Thus, the total efficiency was ≈0.13%, excluding losses from collisions along the long MRTOF flight path. In general, higher Z ions yield higher stopping efficiency, gas-cell extraction efficiency and trapping efficiency. In an offline test with ^{23}Na ions, the MRTOF efficiency was found to be 27% as described in Sec. 3.3.1.

4.2 Time-of-flight measurements

Prior to being analyzed by the MRTOF, ions are prepared in a sequential pair of buffer gas-filled rf ion traps [70]. Ions are initially stored and precooled in the taper trap before being transferred to the flat trap. The flat trap quickly cools ions to a very small cloud and then ejects them toward the MRTOF by means of an electric dipole field. The small ion cloud and nearly pure dipole extraction field provide ideal conditions for analysis with the MRTOF. Complementary pulses of ±60 V applied to the central electrodes create a dipole electric field for orthogonally extracting ions from the trap.

During the measurement of $^{8}Li^{+}$, the taper trap was utilized as an auxiliary trap to accumulate and precool ions while another ion bunch was cooling in the flat trap.

As shown in Fig. 4.3, ions were accumulated and precooled in the taper trap for 10 ms before

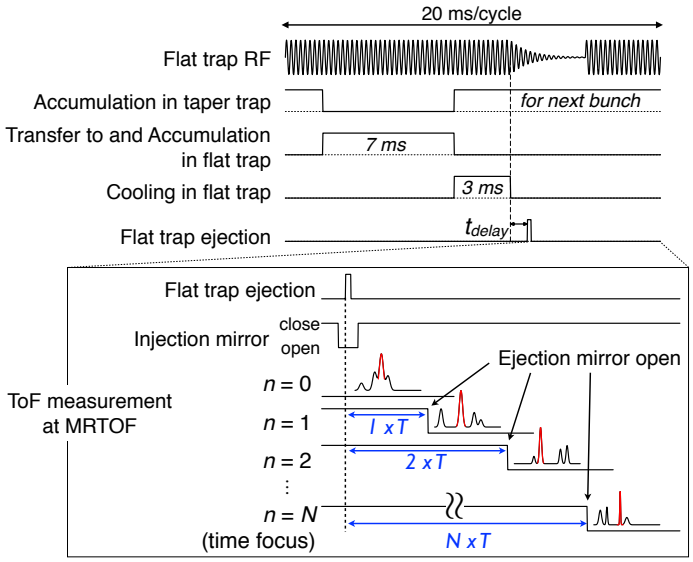

Figure 4.3: Measurement time sequence for the trap and MRTOF system (not to scale). After the species of interest, indicated by the red peak, makes N laps, the potential of the MRTOF ejection mirror is reduced to allow ions passage and the ions are detected with a MCP. Only ions with A/q sufficiently similar to the species of interest make N laps, while heavier (lighter) ions make fewer (more) laps.

being transferred to the flat trap. To maximize the accumulation efficiency, 7 ms was allotted for the transfer to and accumulation in the flat trap. After accumulating the ions in the flat trap, the trap axial potential well was deepened for 3 ms to maximally cool the ion cloud prior to ejection to the MRTOF. While one ion bunch is cooling in the flat trap, the next bunch is already accumulating in the taper trap, thereby, allowing an operational duty cycle of ≈100%.

After cooling, the flat trap rf signal was briefly turned off to minimize the effect of the rf electric field on ions leaving the trap. Due to the high Q-value of the rf resonant circuit, however, the rf amplitude decayed exponentially with a decay constant of $\tau \sim 250$ μs. Since waiting for the amplitude to fully decay would allow the ion cloud to expand, the ejection was instead phase locked to a point in the amplitude decay found to yield a maximum resolving power. The phase locked ejection signal served as the TDC start signal for the ion time-of-flight (ToF).

Prior to ejection of ions from the flat trap, the potential of the first MRTOF injection mirror electrode was reduced by 1 kV to allow the ions entry. The potential was then returned to its nominal value at the time when the ions were in the MRTOF ejection mirror electrodes, to minimize any effects from the changing potential. The ions were then allowed to reflect between the two mirrors for a time sufficient to allow the ions to make 880 laps. After 880 laps, while the ions are in the injection mirror, the final ejection mirror electrode potential was reduced by 1 kV to allow ions to exit and travel to a MCP detector, providing stop signals for the TDC.

As in any other mass spectroscopic technique, reference measurements are required to determine the mass from the time of flight. Ideally, isobaric references would be used. In the case of $^{8}Li^{+}$, however, the only isobaric reference available was $^{4}He_{2}^{+}$, the rate of which was almost an order of magnitude less than that of $^{8}Li^{+}$. As such, $^{12}C^{+}$ from the gas cell was used as a reference. Ions produced by the ESI described in Sec. 3.5.2 were not useful in this case, as it only produces ions heavier than ^{12}C.

Typical time-of-flight spectra for $^{8}Li^{+}$ and $^{12}C^{+}$ are shown in Fig. 4.4 with times-of-flight of $t_8 \sim 8$ ms and $t_{12} \sim 9.8$ ms, respectively. Due to higher-order ion optical aberrations in the mirrors and low-angle scattering from the residual gas during flight, the spectrum has a slow tail. In order to properly take the tail into account, a Gaussian fitting function with an exponential-tail [88], as described by Eq. (4.10), was used.

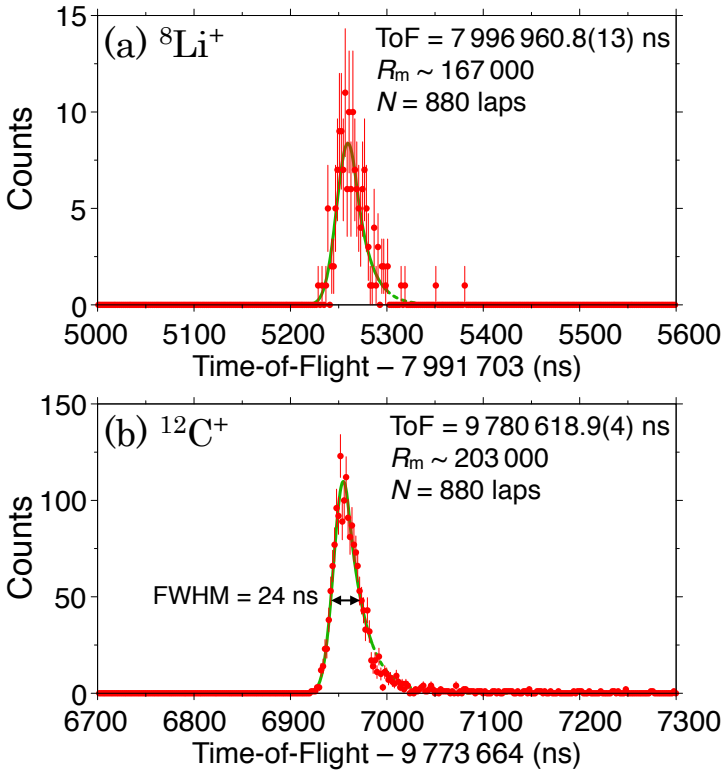

Figure 4.4: Typical time-of-flight spectra for (a) $^{8}Li^{+}$ and (b) $^{12}C^{+}$ after 880 laps in the MRTOF. The slow tail is a result of higher-order ion optical aberrations in the mirrors and low-angle scattering from the residual gas in the reflection chamber. The fit shown is from Eq. 4.10, see text for details.

$$f(t) = \begin{cases} A\ e^{-(t-t_m)^2/2\sigma^2} & \text{for } t \leq t_m + t_c \\ A\ e^{t_c(2t_m - 2t + t_c)/2\sigma^2} & \text{for } t \geq t_m + t_c \end{cases} \tag{4.10}$$

where A is the Gaussian peak height, t_m is the Gaussian centroid, σ is the standard deviation of the Gaussian, and t_c is the distance from t_m to the exponential tail switching point. The shape parameters t_c and σ were determined from a high-statistics $^{12}C^+$ spectrum and fixed for all fittings. The spectra of $^8Li^+$ were each accumulated for 600 s, while each spectrum of $^{12}C^+$ only required 50 s. Mass resolving powers of $R_m \sim 167\,000$ for $^8Li^+$ and $R_m \sim 203\,000$ for $^{12}C^+$ were achieved.

4.3 Data analysis by Single-reference method

The mass is related to the time-of-flight by the simple relation of $t = \alpha\sqrt{m}$, where t is the time-of-flight, m is the mass, and α is the coefficient related to the total kinetic energy of an ion and the flight length. In reality, however, the time of flight has an offset t_0, *i.e.*, $t = \alpha\sqrt{m} + t_0$, which results from *e.g.*, differences in cable and electronic delays between the TDC start and stop signals. To calculate the coefficient without knowledge of the offset, at least two reference ions whose masses are already known with sufficiently high precision are generally used. To perform this multi-reference method, such a pair of ions with well-known masses must be prepared with sufficient intensities.

In addition, for accurate mass measurements with the MRTOF, the slight ToF drift must be compensated by reference species. In the case of multi-reference method, the compensation can be rather complicated. Furthermore, the interval between the reference measurements become longer, and the linear interpolation of the drift may become less valid. Additionally, statistical uncertainty in the unknown mass contains fitting uncertainty from 5 sets of data.

In our measurements, therefore, a so-called "single-reference method" was adopted, as will be explained in the following section. Using the single-reference method, the analysis became fairly simple, the statistical uncertainty was minimized, and the ToF drift compensation was easily performed.

The behavior of the ToF drift during a measurement such as $^8Li^+$, for which the rate was low, can be a source of measurement uncertainty. The analysis of such uncertainty is not straightforward, however. In the following discussion, we apply two separate treatments of the drift to determine the mass of $^8Li^+$.

a) Linear interpolation approach

In order to determine the mass of ^{8}Li, we used the single-reference analysis method for the ToF-MS. Such analysis is already well-established in Penning trap mass spectrometry. The procedure of the method is illustrated in Fig. 4.5. $^8Li^+$ measurements are interleaved between two reference measurements of $^{12}C^+$. For various reasons, the ToF position drifts over time. While such drifts are in principle not linear, over short durations they can be reasonably approximated as linear. As such, a co-temporal ToF value for the reference ($^{12}C^+$) can be determined by linearly interpolating from reference measurements prior to and after the $^8Li^+$ measurement. The mass ratio between $^{12}C^+$ and $^8Li^+$ can then be determined, assuming the ToF offset t_0 is known.

The ToF offset t_0 was independently determined from the trap ejection noise, by comparing the time difference between the TDC start and the real ion ejection timing. The time difference was directly measured in the same circuit as the ToF measurements as shown in Fig. 4.6 and determined to be $t_0 = 199$ ns. The uncertainty in the propagation path of the noise is considered as a systematic uncertainty, conservatively estimated as $\delta t_0^{sys} = 10$ ns.

All ToF information for $^8Li^+$ and reference species $^{12}C^+$ used for the analysis are listed in Table 4.1, and described as a function of the time elapsed in Fig. 4.7. For all listed time-of-flight values the ToF offset evaluated above has been subtracted from the measured values.

The effective ToFs of $^{12}C^+$, t_{12}, are calculated by linear interpolation,

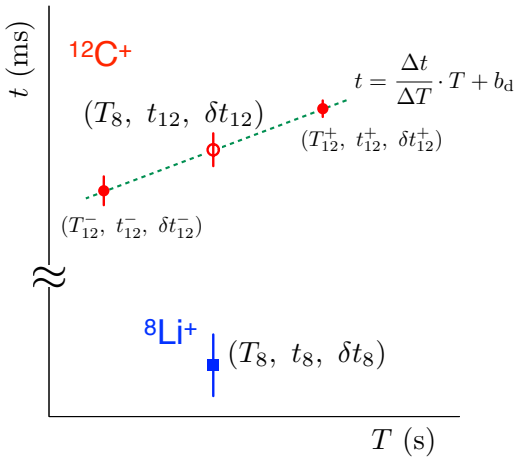

Figure 4.5: Schematic procedure of the single-reference method. Closed symbols indicate measurements for ^{8}Li$^+$ and reference ions ^{12}C$^+$, and open circle indicates the effective ToF of ^{12}C$^+$ at the time of ^{8}Li$^+$ measurement, T_8, interpolated linearly between interleaved ^{12}C$^+$ measurements.

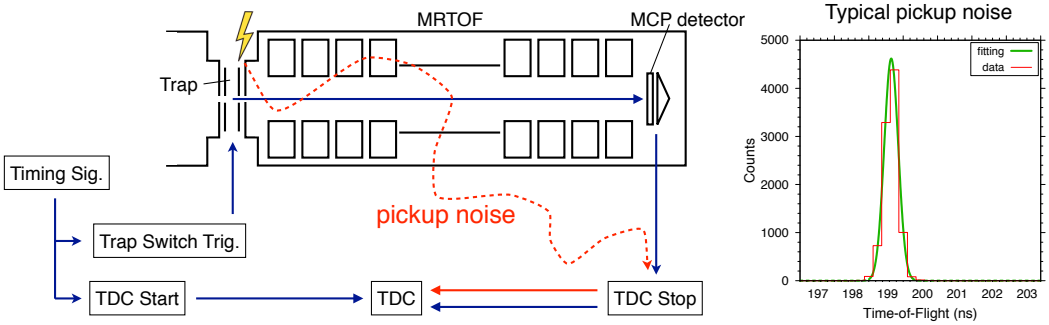

Figure 4.6: Schematic of the ToF offset measurement. The pathway where the pickup noise was passes is unclear.

Table 4.1: All measurements of ^{8}Li$^+$ and reference species ^{12}C$^+$

#	Time (s)	Species	Time of flight (ns)	Effective ToF (ns)
1	0.000	^{12}C$^+$	9 780 620.13(77)	–
2	393.188	^{8}Li$^+$	7 996 962.1(12)	9 780 612.56(67)
3	745.031	^{12}C$^+$	9 780 605.8(11)	–
4	1 088.844	^{8}Li$^+$	7 996 966.0(32)	9 780 610.1(15)
5	1 438.781	^{12}C$^+$	9 780 614.4(29)	–
6	1 782.976	^{8}Li$^+$	7 996 964.5(14)	9 780 617.0(15)
7	2 131.007	^{12}C$^+$	9 780 619.51(89)	–
8	2 473.960	^{8}Li$^+$	7 996 965.1(17)	9 780 616.21(58)
9	2 824.906	^{12}C$^+$	9 780 612.84(74)	–

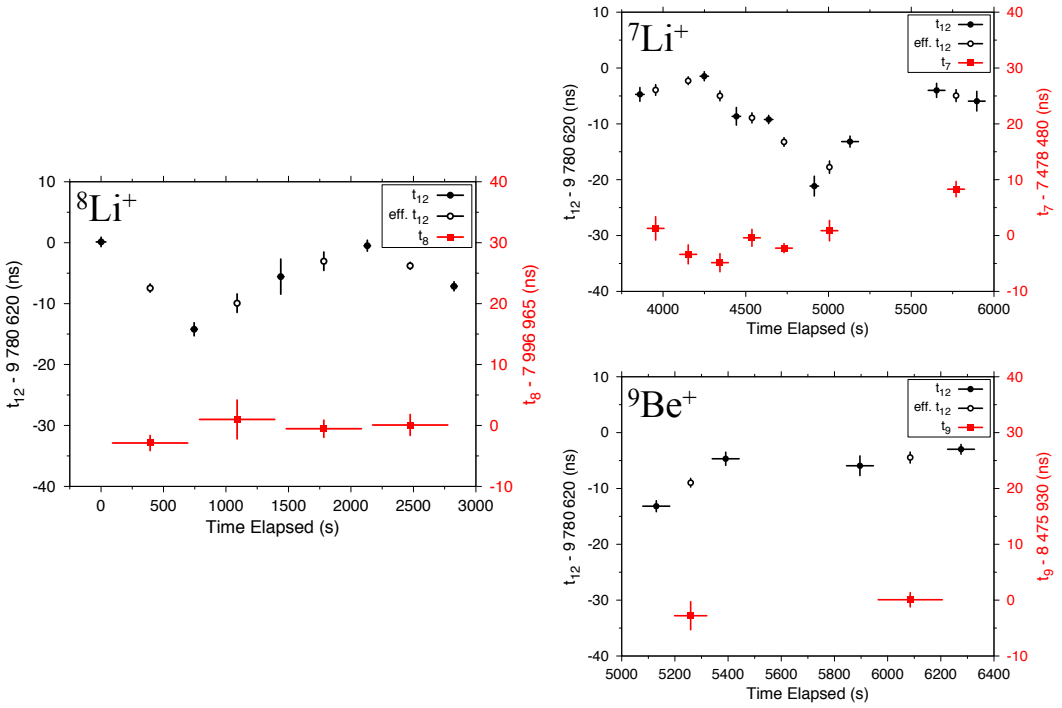

Figure 4.7: All measured ToFs and effective ToFs of $^{12}C^{+}$ calculated by linear interpolation approach as a function of the time elapsed. Vertical error bars represent calculable statistical uncertainties in ToF, while horizontal error bars indicate measurement time durations.

$$t_{12} = t_{12}^{-} + \frac{t_{12}^{+} - t_{12}^{-}}{T_{12}^{+} - T_{12}^{-}}(T_8 - T_{12}^{-}) \tag{4.11}$$

The uncertainty of t_{12}, δt_{12}, was calculated using

$$\delta t_{12} = \sqrt{\left(\frac{\partial t_{12}}{\partial t_{12}^{-}}\delta t_{12}^{-}\right)^2 + \left(\frac{\partial t_{12}}{\partial t_{12}^{+}}\delta t_{12}^{+}\right)^2} \tag{4.12}$$

$$= \sqrt{\left(\frac{T_8 - T_{12}^{+}}{T_{12}^{+} - T_{12}^{-}}\delta t_{12}^{-}\right)^2 + \left(\frac{T_8 - T_{12}^{-}}{T_{12}^{+} - T_{12}^{-}}\delta t_{12}^{+}\right)^2} \tag{4.13}$$

Using each pair of t_8 and t_{12}, the mass of $^{8}Li^{+}$, m_8, was calculated from the simple equation:

$$m_8 = \left(\frac{t_8}{t_{12}}\right)^2 m_{12} = \rho^2 m_{12} \tag{4.14}$$

The statistical uncertainty of m_8, $\delta m_8^{\mathrm{sta}}$, was then calculated from

$$\delta m_8^{\mathrm{sta}} = 2m_8\sqrt{\left(\frac{\delta t_8}{t_8}\right)^2 + \left(\frac{\delta t_{12}}{t_{12}}\right)^2} \tag{4.15}$$

The calculated ρ^2 and m_8 with statistical uncertainties are listed in Table 4.2.

The statistical uncertainties $\delta m_8^{\mathrm{sta}}$ were determined from uncertainties derived from the ToF fittings, while $\delta t_0^{\mathrm{sys}}$ described above leads to a systematic uncertainty. An expansion of Eq. 4.14, taking into account t_0, up to the 1st order in (t_0/t_{12}) yields

Table 4.2: ρ^2-values and masses of $^8Li^+$ in atomic mass units

#	ρ^2	m_8 (u)
2	0.668 525 48(23)	8.021 939 1(27)
4	0.668 526 47(57)	8.021 950 9(69)
6	0.668 525 28(31)	8.021 936 6(38)
8	0.668 525 48(30)	8.021 939 0(36)

$$m_8 = m_{12}\left(\frac{t_8}{t_{12}}\right)^2 + m_{12}\frac{t_8\,(t_8 - t_{12})}{t_{12}^3}t_0 \tag{4.16}$$

The effect of the uncertainty in t_{sys} is determined by the second term in Eq. 4.16. The adopted value of $\delta t_{\mathrm{sys}} = 10$ ns results in a systematic uncertainty of 3.4 keV.

From these results, final ^{8}Li masses were calculated as listed in Table 4.3. In the table, the calculated mass excesses, the weighted average mass excess and the literature mass excess are described together.

Table 4.3: Mass excesses, the weighted average mass excess and the literature value of ^{8}Li

#	Δ_{MRTOF} (keV)	Δ_{Lit} (keV)
2	20 947.0(25)(34)	
4	20 958.1(64)(34)	
6	20 944.7(35)(34)	
8	20 947.0(33)(34)	
wav.(^{8}Li)	20 947.3(17)(34)	20 945.80(5)

To confirm the single reference method, the masses of $^7Li^+$ and $^9Be^+$ were similarly determined with data taken during the online experiment. The ToFs, effective ToFs and ρ^2-values are listed in Table 4.4 calculated in the same way as ^{8}Li, and plotted as a function of the time elapsed in Fig. 4.7. The derived mass excesses are shown in Table 4.5 with the literature values. Figure 4.8 shows the individual deviations from the literature values. The weighted average, including the systematic uncertainty from δt_0, is represented by the green band. In all cases, the results were in agreement with the literature values. The weighted average deviation of ^{8}Li was found to be $\Delta m = 1.5(17)(34)$ keV, corresponding to a relative mass uncertainty of $\delta m/m_{\mathrm{stat}} = 2.3 \times 10^{-7}$. The weighted average deviations of ^{7}Li and ^{9}Be were similarly evaluated and found to be $\Delta m = 3.2(10)(41)$ keV and $\Delta m = 4.2(26)(26)$ keV, respectively.

To check for consistency in the statistical uncertainty evaluation, the Birge ratio [90], R, of the data points was calculated. The Birge ratio is described as

$$R = \frac{\sigma_{\mathrm{out}}}{\sigma_{\mathrm{in}}} \tag{4.17}$$

where the outer error, σ_{out}, gives a measure of the fluctuation of the data around the mean value:

$$\sigma_{\mathrm{out}} = \sqrt{\frac{\sum_i w_i\,(r_i - \bar{r})^2}{(N-1)\sum_i w_i}} \tag{4.18}$$

where r_i is the square of the ratio of the measured ToF to the reference ToF, ρ^2, for each point, w_i is the weight described as $w_i = 1/\sigma_i$ where σ_i is related to the error associated with the ratio r_i, N is the number of data points and $\bar{r}$ is the weighted average of r_i:

Table 4.4: All measurements of $^{7}Li^{+}$, $^{9}Be^{+}$ and reference species $^{12}C^{+}$. Some data which are not available for analysis are indicated by N/A.

#	Time (s)	Species	Time of flight (ns)	Effective ToF (ns)	ρ^2
10	3 860.094	$^{12}C^{+}$	9 780 615.3(12)	–	–
11	3 954.992	$^{7}Li^{+}$	7 478 481.3(21)	9 780 616.07(96)	0.584 648 91(35)
12	4 056.891	$^{12}C^{+}$	N/A	–	–
13	4 151.891	$^{7}Li^{+}$	7 478 476.6(17)	9 780 617.72(69)	0.584 647 98(28)
14	4 248.898	$^{12}C^{+}$	9 780 618.53(82)	–	–
15	4 343.898	$^{7}Li^{+}$	7 478 475.1(16)	9 780 615.01(88)	0.584 647 07(27)
16	4 442.929	$^{12}C^{+}$	9 780 611.4(16)	–	–
17	4 536.969	$^{7}Li^{+}$	7 478 479.6(15)	9 780 611.07(90)	0.584 648 24(26)
18	4 638.007	$^{12}C^{+}$	9 780 610.78(74)	–	–
19	4 731.109	$^{7}Li^{+}$	7 478 477.75(82)	9 780 606.76(78)	0.584 648 47(16)
20	4 914.023	$^{12}C^{+}$	9 780 598.9(18)	–	–
21	5 005.968	$^{7}Li^{+}$	7 478 480.9(18)	9 780 602.3(11)	0.584 649 50(32)
22	5 129.938	$^{12}C^{+}$	9 780 606.83(99)	–	–
23	5 259.179	$^{9}Be^{+}$	8 475 927.2(2.5)	9 780 611.03(77)	0.751 004 37(46)
24	5 391.047	$^{12}C^{+}$	9 780 615.3(12)	–	–
25	5 521.969	$^{9}BeH^{+}$	N/A	–	
26	5 652.984	$^{12}C^{+}$	9 780 616.0(13)	–	–
27	5 770.969	$^{7}Li^{+}$	7 478 488.3(14)	9 780 615.1(11)	0.584 649 13(25)
28	5 895.945	$^{12}C^{+}$	9 780 614.1(18)	–	–
29	6 085.000	$^{9}Be^{+}$	8 475 930.1(13)	9 780 615.53(98)	0.751 004 18(27)
30	6 276.000	$^{12}C^{+}$	9 780 617.01(87)	–	–

Table 4.5: Mass excesses, weighted-average and the literature value mass excess of ^{7}Li and ^{9}Be

#	Species	Δ_{MRTOF} (keV)	Δ_{Lit} (keV)
11	^{7}Li	14 906.5 (39)(41)	
13		14 896.1 (31)(41)	
15		14 897.1 (31)(41)	
17		14 910.2 (29)(41)	
19		14 912.7 (18)(41)	
21		14 924.2 (35)(41)	
27		14 920.1 (28)(41)	
wav.(^{7}Li)		14 910.3 (10)(41)	14 907.105(4)
23	^{9}Be	11 354.0 (52)(26)	
29		11 351.9 (31)(26)	
wav.(^{9}Be)		11 352.4 (26)(26)	11 348.45(8)

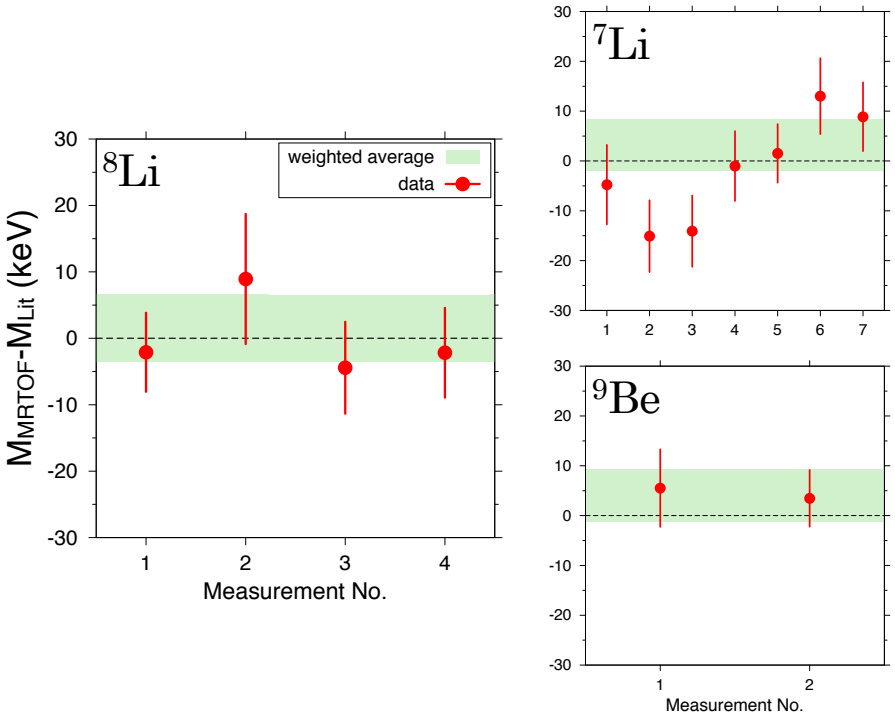

Figure 4.8: Deviations of each measurements from AME2012 values [89]. The systematic uncertainty in δt_0 has been included. The weighted averages with the systematic uncertainties are also shown by the green band.

$$\bar{r} = \frac{\sum_i w_i r_i}{\sum_i w_i} \tag{4.19}$$

The inner error, σ_{in}, is the weighted average error:

$$\sigma_{\text{in}} = \sqrt{\frac{1}{\sum_i w_i}} \tag{4.20}$$

The error in the Birge ratio can also be calculated and scales with the root of the number of data points:

$$\sigma_R = \frac{0.4769}{\sqrt{N}} \tag{4.21}$$

The Birge ratio gives an indication of whether or not the variance in the evaluated data has properly accounted for statistical uncertainties. A Birge ratio of 1 indicates that the evaluated data is consistent with statistical fluctuations. A ratio greater than one suggests that some source of statistical uncertainty has been neglected, resulting in an underestimated uncertainty in the evaluated data. A Birge ratio of less than one could suggest that the error bars have been overestimated.

Except for the case of ^{9}Be which had only two data points, the Birge ratios R were calculated and shown in Table. 4.6. The Birge ratio of ^{8}Li is unity within the uncertainty, so the evaluation of uncertainty seems to be correct, while the Birge ratio of ^{7}Li is still much larger than unity. Therefore, the uncertainty evaluation using linear interpolation, neglecting fluctuations during the measurement, underestimated the actual uncertainty in the evaluated data. Typically, one could simply rescale the

Table 4.6: Results with Birge ratios R for linear interpolation approach

Species	Δ_{MRTOF} (keV)	Δ_{Lit} (keV)	Deviation (keV)	R
^{8}Li	20 947.3(17)(34)	20 945.80(5)	1.5(17)(34)	1.07(28)
^{7}Li	14 910.3(10)(41)	14 907.105(4)	3.2(10)(41)	3.42(19)
^{9}Be	11 352.4(26)(26)	11 348.45(8)	4.0(26)(26)	N/A

evaluated uncertainties by the Birge ratio to compensate for such difficult to quantify statistical uncertainties.

b) Constant assumption approach

The Birge ratios for ^{7}Li is much larger than unity in Table. 4.6. This suggests an underestimate of the uncertainties in compute the mass values. This is most likely related to the difficult to quantify effect of fluctuations during the measurements. While we could simply rescale the uncertainties by the Birge ratio, let us try to account for these fluctuations by using a different method to calculate the reference ToF used. The linear interpolation method previously used assumed that the ToF drift was smooth and linear, however a real drift includes micro fluctuations in violation of this assumption. As such, using a weighted average value of two interleaved $^{12}C^{+}$ ToFs as an effective $^{12}C^{+}$ ToF and its standard deviation as an uncertainty could be better approach than using linear interpolation as regards evaluating the uncertainty.

The weighted average ToF and its standard deviation were calculated by

$$t_{\mathrm{wav}} = t_{12} = \frac{\sum_i w_i t_i}{\sum_i w_i} \tag{4.22}$$

$$\delta t_{\mathrm{wav}} = \delta t_{12} = \sqrt{\frac{\sum_i w_i \left(t_i - t_{\mathrm{wav}}\right)^2}{(n-1)\sum_i w_i}} \tag{4.23}$$

where n is the number of points, t_i and δt_i are the measured reference ToF and its uncertainty.The ToFs, effective ToFs and ρ^2-values are listed in Table 4.7, and plotted as a function of the time elapsed in Fig. 4.9. The derived mass excesses are shown in Table 4.8 with the literature values and the Birge ratios R. The Birge ratio of ^{8}Li is unity within the uncertainty, therefore the evaluation of uncertainty seems to be still correct, while the Birge ratio of ^{7}Li is still larger than unity, but much smaller than in the case of linear interpolation.

Figure 4.10 shows the individual deviations from the literature values. The weighted average, including systematic uncertainty in δt_0, is represented by the green band. In all cases, the results were in agreement with the literature values. The weighted average deviation of ^{8}Li was found to be $\Delta m = -0.04(267)(341)$ keV, corresponding to a relative mass uncertainty of $\delta m/m_{\mathrm{stat}}$=3.6×10^{-7}. The weighted average deviations of ^{7}Li and ^{9}Be were similarly evaluated and found to be $\Delta m = 2.3(12)(41)$ keV and $\Delta m = 2.5(31)(26)$ keV, respectively. Note that scaling of the uncertainties by the Birge ratios results in the mass value for ^{7}Li having a deviation of less than 1-σ_{stat}.

From these online mass measurements and many offline developments, the performance of MRTOF and the new analysis method were confirmed. It is found that the conventional linear interpolation approach may not be the most appropriate analysis method for current MRTOF measurements due the ToF drift. The constant assumption approach, which takes the magnitude of drift into account when calculating the uncertainties, looks rather better for estimating the uncertainties. It produces a smaller deviation from literature values and Birge ratios closer to unity. However, in all cases the Birge ratio scaled results were accurate for both analysis methods.

Based on these results, the measurement time, t_{meas}, for ions up to 250 u/q with the achieved mass resolving power of $R_{\mathrm{m}} \approx 170,000$ was calculated as shown in Fig. 4.11 and compared with existing Penning trap mass spectrometers (PTMS). The measurement times for PTMS were calculated by

Table 4.7: All measured ToFs of $^{8}Li^{+}$, $^{7}Li^{+}$ and $^{9}Be^{+}$, effective $^{12}C^{+}$ ToFs calculated by the constant assumption approach, and ρ^2 values.

Species	Time of flight (ns)	Effective ToF (ns)	ρ^2
$^{8}Li^{+}$	7 996 962.1(12)	9 780 615.2(68)	0.668 525 12(95)
	7 996 966.0(32)	9 780 606.9(28)	0.668 526 91(66)
	7 996 964.5(14)	9 780 619.0(14)	0.668 524 98(31)
	7 996 965.1(17)	9 780 615.5(33)	0.668 525 56(53)
$^{7}Li^{+}$	7 478 481.3(21)	9 780 617.6(15)	0.584 647 73(37)
	7 478 476.6(17)	9 780 617.6(15)	0.584 647 00(32)
	7 478 475.1(16)	9 780 617.1(29)	0.584 646 83(43)
	7 478 479.6(15)	9 780 610.88(22)	0.584 648 26(24)
	7 478 477.75(82)	9 780 609.0(43)	0.584 648 20(52)
	7 478 480.9(18)	9 780 604.9(34)	0.584 649 17(50)
	7 478 488.3(14)	9 780 615.31(92)	0.584 649 09(24)
$^{9}Be^{+}$	8 475 927.2(25)	9 780 610.4(42)	0.751 004 47(78)
	8 475 930.1(13)	9 780 616.5(12)	0.751 004 04(29)

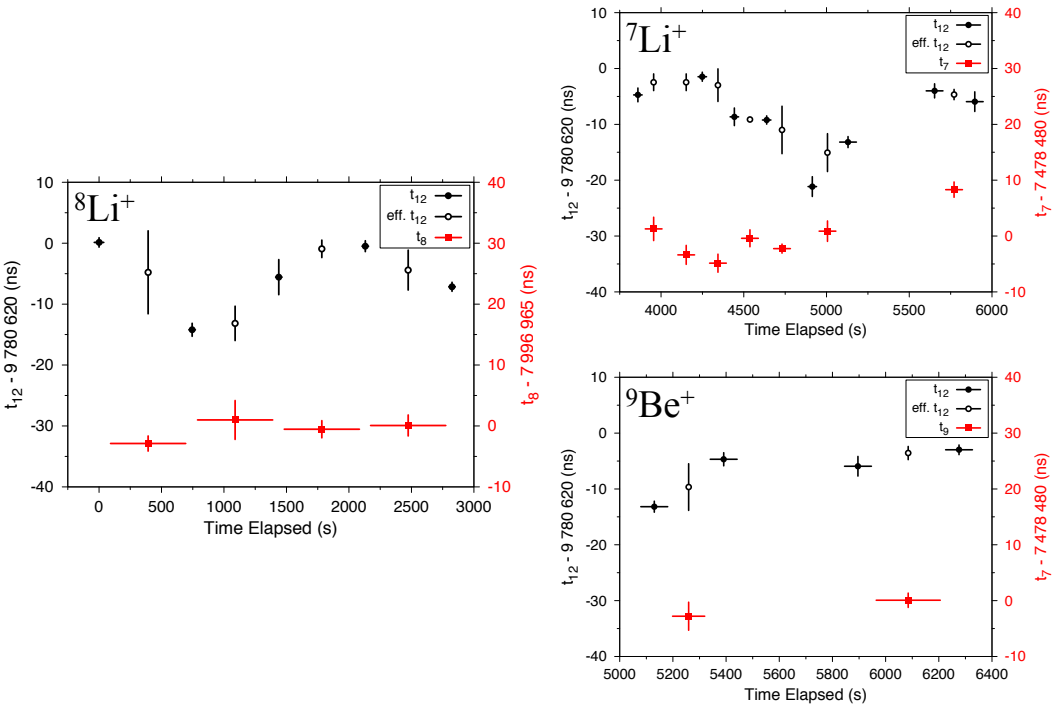

Figure 4.9: All measured ToFs and effective ToFs of $^{12}C^{+}$ calculated by constant assumption approach as a function of the time elapsed. Vertical error bars represent calculable uncertainties in ToF, while horizontal error bars indicate measurement time durations.

Table 4.8: Weighted-average, literature value mass excesses and the deviations with Birge ratios for constant assumption approach

Species	Δ_{MRTOF} (keV)	Δ_{Lit} (keV)	Deviation (keV)	R
^{8}Li	20 945.8(27)(34)	20 945.80(5)	-0.04(267)(341)	0.95(28)
^{7}Li	14 909.4(14)(41)	14 907.105(4)	2.3(12)(41)	2.70(19)
^{9}Be	11 350.9(31)(26)	11 348.45(8)	2.5(31)(26)	N/A

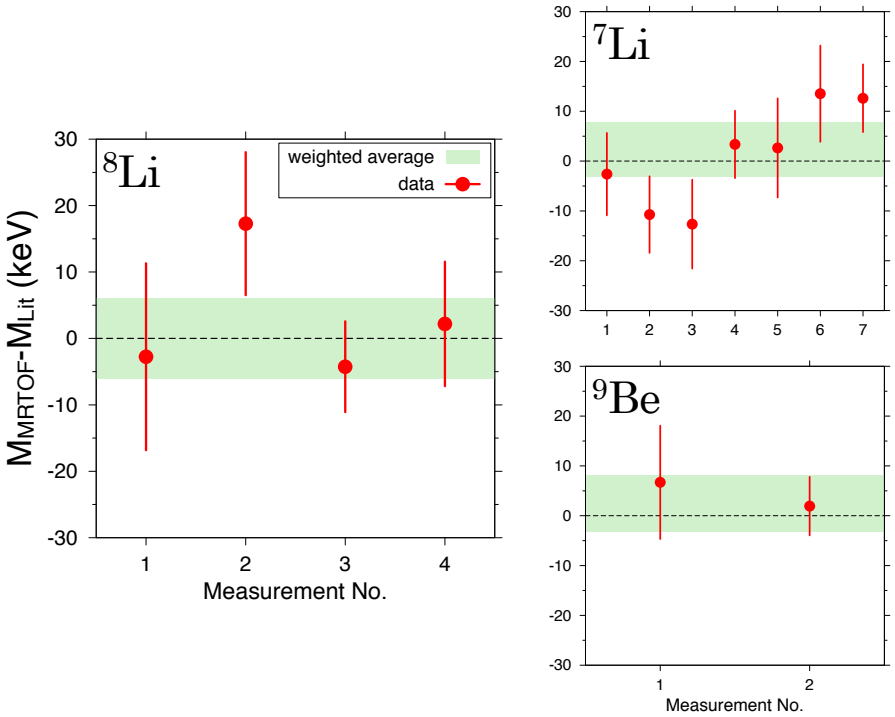

Figure 4.10: Deviations of each measurements from AME2012 values [89] for constant assumption approach. The systematic uncertainties are included. The weighted averages with the systematic uncertainties are also shown by the green band.

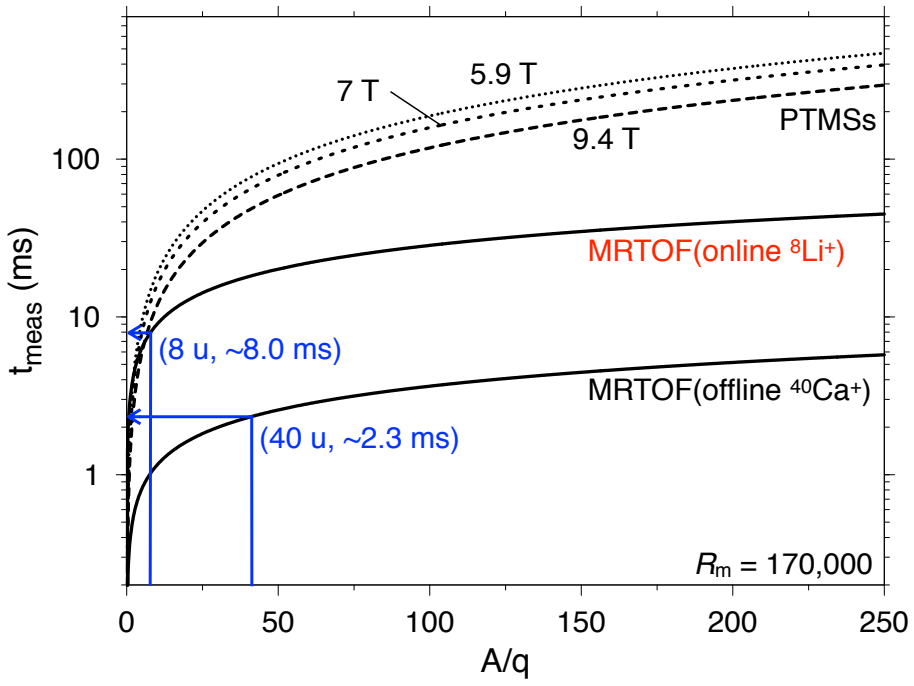

Figure 4.11: Dependence between the measurement time and mass. The magnetic strengths correspond to existing Penning trap mass spectrometers: 5.9 T for ISOLTRAP, 7 T for SHIPTRAP and JYFLTRAP, and 9.4 T for LEBIT. The curve for the MRTOF with $^{40}Ca^{+}$ is the most recent tuning of the MRTOF and not described in this thesis (see Ref. [91]).

$t_{\mathrm{meas}}^{\mathrm{PTMS}} = mR_{\mathrm{m}}/qB$, while those for the MRTOF were calculated by $t_{\mathrm{meas}}^{\mathrm{MRTOF}} = 2\alpha R_{\mathrm{m}}\sqrt{m/q}$, where m is the mass of ion of interest, R_{m} is the mass resolving power, q is the charge, B is the magnetic field and α is the normalized coefficient at the measurement point. Using the coefficient calculated from the online result of ^{8}Li ($A/q = 8$ and $t_{\mathrm{meas}} = 8$ ms), the t_{meas} of the MRTOF does not gain so much compared to the PTMS in the light region such as ^{8}Li due to the cyclotron frequency being high enough to precisely measure in a short time. While, as it is scaled $\sqrt{m}$ in the case of the MRTOF, there is about an order of magnitude difference between them at $A/q > 100$. For $A/q > 100$, the PTMS already takes $t_{\mathrm{meas}} > 100$ ms while the MRTOF takes only $t_{\mathrm{meas}} \sim 20$ ms.

Additionally, the MRTOF was recently tuned better and can achieve the same mass resolving power with much shorter t_{meas}. In this fast tuning with $^{40}Ca^{+}$, the t_{meas} was only 2.3 ms. The curve in Fig. 4.11 is even below the one of $^{8}Li^{+}$, and the t_{meas} of the MRTOF is about two order of magnitude less than that of PTMS – the t_{meas} is below 10 ms over full range.

5 Discussion and possible improvements

As seen above, it is succeeded in online mass measurement with the precision of less than 10^{-6} and good accuracy. However, the performances of current system is not comparable to the designed one: the mass resolving power of 10^6 and the trapping efficiency of almost unity.

Here, some possible improvements are proposed with discussions of some issues, especially for the trapping efficiency, the MRTOF measurement.

5.1 Trapping efficiency

In Sec. 3.3.1, trapping efficiencies of 5.1% for $^7Li^+$ and 27% for Na^+ were described. As already mentioned, the difference in efficiency between Na^+ and $^7Li^+$ is caused by the mass difference from the helium. It is a well-understood and well-known effect in the buffer-gas cooling technique.

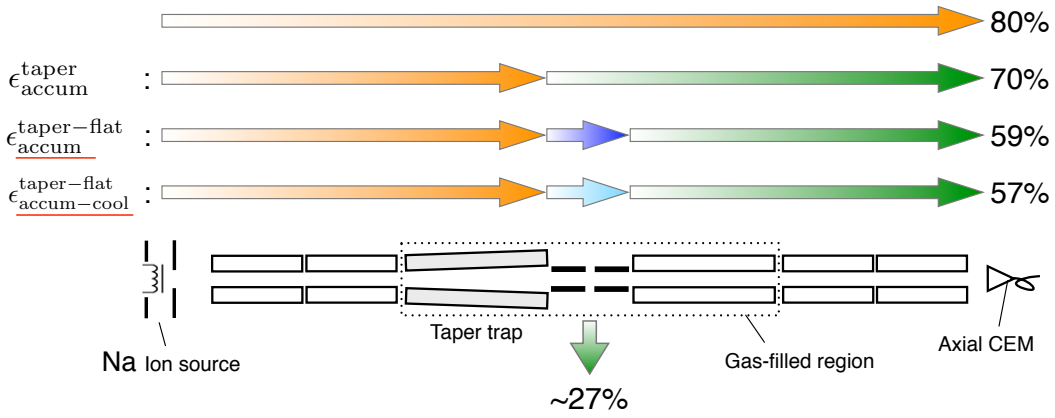

Figure 5.1: Efficiencies measured at various places

Here, it is discussed where the efficiency bottlenecks are. In order to find the bottlenecks, various efficiencies were measured using Na^+ ions as described in Fig. 5.1. The same setup and conditions as Fig 3.2 was used and the ion counts were measured at the axial CEM. As it was already described in Sec. 3.2.3, the transmission efficiency through the flat trap is $\epsilon_{straight} \approx 80\%$. The measured efficiency after accumulating in the taper trap for 10 ms, ϵ^{taper}_{accum}, was determined to be ~70%. The measured efficiency after accumulating in the taper trap for 10 ms, transporting to and accumulating for 7 ms in the flat trap, $\epsilon^{taper-flat}_{accum}$, was determined to be ~59%. The measured efficiency after accumulating in the taper trap for 10 ms, transporting to and accumulating for 7 ms and cooling for 3 ms in the flat trap, $\epsilon^{taper-flat}_{accum-cool}$, was determined to be ~57%.

From $\epsilon^{taper-flat}_{accum}/\epsilon^{taper}_{accum}$, the transport efficiency from the taper trap to the flat trap, $\epsilon^{taper-trap}_{trans}$, was calculated to be ~84%. From $\epsilon^{taper-flat}_{accum-cool}/\epsilon^{taper-flat}_{accum}$, the transition efficiency by the dc potential change, $\epsilon^{accum-cool}_{trans}$, was calculated to be ~97%, which means almost no loss during the process. From the trapping efficiency of 27% for Na^+ divided by $\epsilon^{taper-flat}_{accum-cool} = 57\%$, the transport efficiency during trap ejection process was obtained to be ~47%, which is the largest part of the efficiency loss.

For the efficiency loss during trap ejection, the possible reasons include:

1. scattering in poor vacuum region in and after the trap
2. larger transverse beam size than the trap ejection hole (0.8 mm in diameter)

The pressure in the flat trap is estimated to be on the order of 10^{-3} mbar and the pressure in the trap chamber is measured to be about 1×10^{-5} mbar. The mean free path, λ, corresponding to a He pressures of 10^{-3} mbar and 10^{-5} mbar are calculated as $\lambda \sim 200$ mm and 20 m, respectively. The pressure along ion flight path in the poor vacuum region is expected to be in between. For such long mean free path, it is difficult to explain the efficiency reduction above.

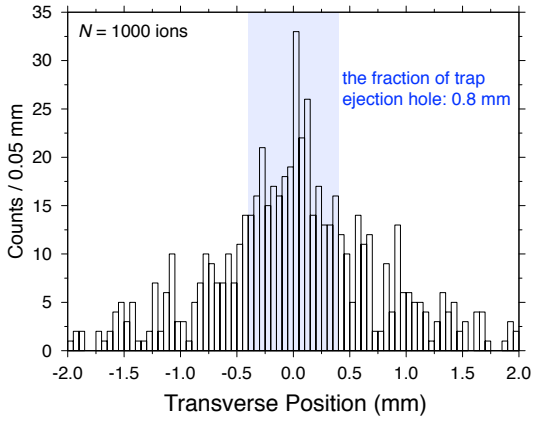

Figure 5.2: Simulated transverse size of ion bunch in the flat trap

The transverse beam size after cooling is determined by the ion energy and the axial potential well. It was simulated by SIMION and the distribution is shown in Fig. 5.2. The simulation was performed under the same trap condition as experiment ($f_{\mathrm{rf}} = 5$ MHz, $V_{\mathrm{rf}} = 400$ V_{pp} and the estimated He pressure of 1×10^{-3} mbar). The fraction within ± 0.4 mm is evaluated to be $\sim$43% which agree well with the experimental efficiency of $\sim$47%. Therefore, the major efficiency bottleneck is considered to be due to the transverse beam size.

The second bottleneck is the transfer to the flat trap from the taper trap, $\epsilon_{\mathrm{accum}}^{\mathrm{taper}}$, which was $\sim$70%. It is caused by

1. rf mismatching between the taper trap and the flat trap
2. field imperfection
3. insufficient radial cooling in the taper trap

From the simulation described in Sec. 3.3.1, the effects of the rf mismatching between the traps and the field imperfection are not so much to make ion motion unstable.

The insufficient radial cooling could occur in the taper trap. The pressure in the taper trap is not measurable, so the pressure is estimated from the gas flow conductance and the pressure in the trap chamber. Actually, the conductance of the trap ejection holes (2×0.5 mm^2) is negligibly small compared to the apertures before the taper traps (2×10 mm^2), therefore a pressure gradient along the taper trap can be created. In that case, the radial cooling in the taper trap would be smaller than expected, which causes the transverse beam size to become larger and reduce the transmission efficiency at the boundary.

5.2 Possible improvements for trapping efficiency

To overcome the problems associated with the trapping efficiency discussed above, we are developing several solutions.

5.2.1 Enhancement of the cooling effect

The current gas pressure in the traps, estimated as $\sim 10^{-3}$ mbar, is limited by the gas pressure in the MRTOF chamber. For ion-optical purposes, and to minimize the overall size of the MRTOF

system, the distance between the flat trap and the MRTOF entrance was designed to be ∼200 mm. By extended the distance up to ∼400 mm, additional pumps can be mounted and the pressure in the traps can be increased.

Additionally, by cryogenic cooling to the flat trap mount, the temperature of the gas can be reduced by a factor of about three, which corresponds to be about three times larger gas density with the same gas pressure. In addition, the final ion equilibrium temperature can be smaller.

By these improvements, the cooling effect can be enhanced and the bottlenecks described in Sec. 5.1 can be solved. These are undergoing design and simulat, and will be installed in the SHE-Mass setup (see Sec. 6.1).

5.2.2 Multi-step potential switching

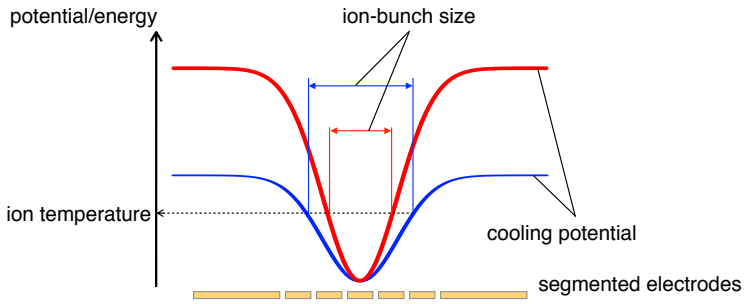

Figure 5.3: Schematic view of the potential shape for cooling phase. The blue line shows a shallower potential case and the red line shows a deeper potential case.

At given ion temperature, the trapped ion-bunch size is determined by the trapping potential well depth. To make a small ion bunch at given ion temperature, the trapping potential must be steeper as shown in Fig. 5.3. In the present setup, the potential is changed deeper from the accumulation phase to the cooling phase by single step. Therefore, if the potential difference is too large, *i.e.*, the cooling potential is too deep, the ions are lost due to the ions get energies by sudden potential changes.

In order to make the cooling potential deeper, the potential must be changed adiabatically. A multi-step potential switching from the accumulation phase to the cooling phase can be helpful.

5.2.3 New precooler trap coated by resistive material

The taper trap has worked well despite the much simpler structure than the conventional segmented structure. To make an effective axial drag force, however, the inter-rod radius of the exit side must be larger than the entrance side as explained in Sec. 3.1. This causes the pseudo-potential well to become shallower and the beam size to become larger.

Another way to make an axial drag force without any segmentations is to use ceramic rods painted by resistive material instead of conventional metal rods. Figure 5.4 shows a photograph of a prototype resistive rod which was made recently and the schematic cross-sectional view. At the edges of the rod, a conductive material is painted, while a resistive material is painted in the middle. The resistive material slightly overlaps with the conductive material to make good electrical contacts. The resistance of the paint material is ∼100 kΩ/seg.

Using the resistive rods, it is possible to make a precooler without tapered structure. The parallel structure can create a deeper pseudo-potential and a well-shaped quadrupole field. Therefore, a smaller beam size, better cooling effect and more stable trapping can be achieved.

5.3 Advanced ToF measurement

To improve the accuracy of the single-reference method and overcome the problems associated with ToF drift seen above, we are developing several solutions.

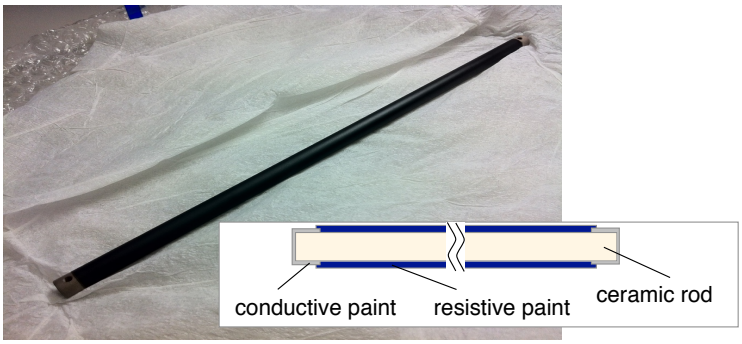

Figure 5.4: Photograph of a prototype resistive rod. At the edges of the rod, a conductive material is painted, while a resistive material is painted in the middle. The resistive material slightly overlaps with the conductive region to make good electrical contacts.

5.3.1 Use of closer references

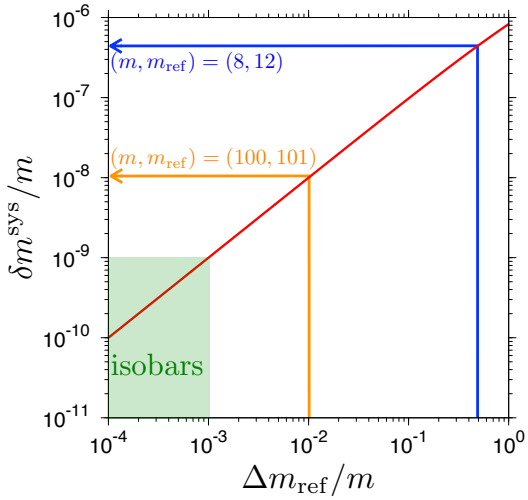

Figure 5.5: The effect of $\delta t_0^{\rm sys}$ for relative mass uncertainty as a function of relative mass difference. $t_{\rm ref} = 10$ ms and $\delta t_0^{\rm sys} = 10$ ns are assumed in this case.

In the online ^{8}Li measurements, $^{12}C^{+}$ was used as a reference because there are no stable $A = 8$ elements and $^{12}C^{+}$ was the lightest stable ion obtained with sufficient intensity. In the single-reference analysis of ^{8}Li, a systematic uncertainty of 3.4 keV, corresponding to $\delta t_0^{\rm sys} = 10$ ns, was added. The contribution of $\delta t_0^{\rm sys}$ to the systematic uncertainty is given by

$$\frac{\delta m^{\rm sys}}{m} = \frac{2m_{\rm ref}}{m}\frac{t(t-t_{\rm ref})}{t_{\rm ref}^3}\delta t_0^{\rm sys} \tag{5.1}$$

$$= \frac{2}{t_{\rm ref}}\left(1 - \sqrt{\frac{m+\Delta m_{\rm ref}}{m}}\right)\delta t_0^{\rm sys} \tag{5.2}$$

where $\delta m^{\rm sys}/m$ is the relative systematic uncertainty, $m_{\rm ref}$ and $t_{\rm ref}$ are the mass and ToF of the reference ion, and m and t are the mass and ToF of the ion of interest. The effect of $\delta t_0^{\rm sys}$ with $t_{\rm ref} = 10$ ms and $\delta t_0^{\rm sys} = 10$ ns to the relative systematic mass uncertainty $\delta m_{\rm sys}/m$ as a function of relative mass difference $\Delta m_{\rm ref}/m$ is shown in Fig. 5.5. For the combination of $(m, m_{\rm ref}) = (8, 12)$

as was the case in our ^{8}Li measurement, the relative systematic uncertainty is rather large because the relative mass difference is large. While for the case of $(m, m_{\mathrm{ref}}) = (100, 101)$ corresponding to $\delta m_{\mathrm{sys}}/m = 1$ %, the contribution of $\delta m_{\mathrm{sys}}/m$ is quite small; in the case of isobaric species it becomes negligibly small. In the any case of mass heavier than Carbon, $A \geq 12$, isobaric molecular reference ions can be easily provided from the rf-carpet ESI ion source or another stable ion source; simultaneous isobars are also available through the fragmentation process. Therefore, with better reference species, the final uncertainty could be determined from only statistical uncertainty and could be $\delta m/m \approx 10^{-7}$–$10^{-8}$.

5.3.2 Cycle-by-cycle measurements

In the measurement procedure employed above, each measurement is continuously performed for a fixed duration to accumulate sufficient statistics to reliably perform peak fitting. If the ion rate is sufficiently high, then each measurement could by short enough to follow macro and micro ToF drifts. When long durations between reference measurements are needed, however, the uncertainty in the reference ion's time-of-flight could be underestimated, as seen above, and the error analysis will become complicated, which could lead to overly high precision with inaccurate results.

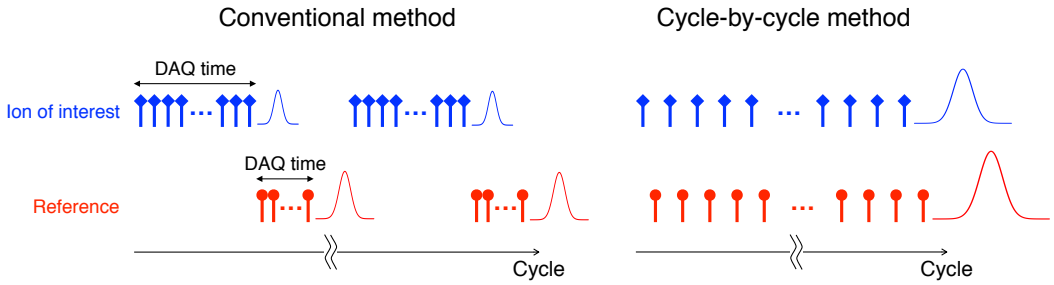

Figure 5.6: Comparison of the cycle-by-cycle method with the conventional method. Bars colored blue for ions of interest and red for reference ions indicate each cycle. In the conventional method, counts are accumulated during each DAQ time and peaks are obtained after each measurement, while in the "cycle-by-cycle (CbC)" method the measurement is switched cycle by cycle and a peak is obtained after enough cycles.

Because excessive numbers of ions per cycle lead to lost counts from detector dead time, even maximally intense ions require N$\gg$100 cycles before sufficient statistics exist for reliable peak fitting. In principle, we could make minimum duration reference measurements interleaved with similar durations of accumulation of data for the unknown species. The data for unknown species could be aggregated in some way taking account of longterm drifts seen in the references. However, such would result in 50% loss from duty cycle and may not guarantee overcoming the problem of not knowing the nature of the drift. To avoid such difficulties and improve the accuracy of the measurements, a "cycle-by-cycle (CbC)" method as shown in Fig. 5.6 should be used.

In the CbC method, such uncertainties in the drift can be minimized. Each measurement of reference species and unknown RIs would be switched cycle by cycle, *i.e.*, durations of 20 ms each at 50 Hz operation. It allows a measurement nature nearly equivalent to the isobaric simultaneous measurement, therefore the drifts would be reflected in each measurement and a better final precision and accuracy could be expected. Additionally, using this method with the flat trap, the reference ions and unknown RIs can be introduced into the flat trap from opposing sides. While the reference measurement is being made, unknown RI can be allowed to simply accumulate in the taper trap, thereby allowing operation with no duty cycle losses.

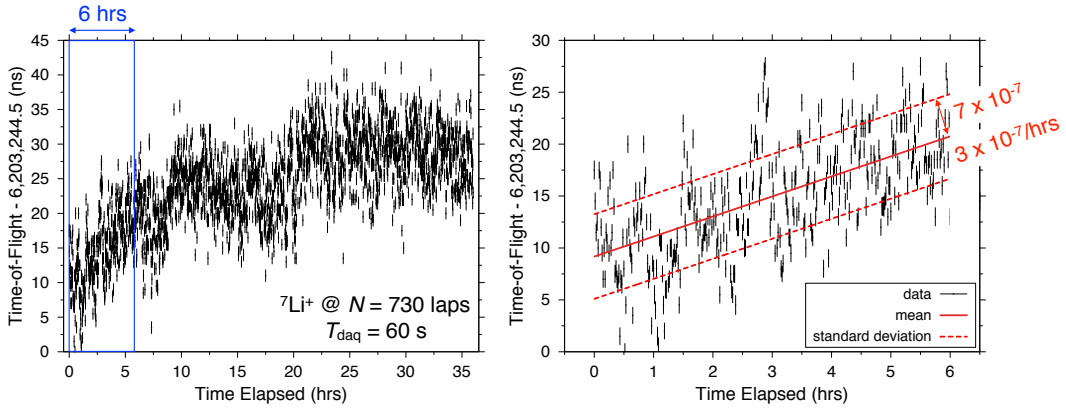

Figure 5.7: Macro ToF drift (left) and micro ToF drift (right). The right figure is enlarged figure for the first 6 hrs in the left figure.

5.3.3 Drift reduction

The precision and accuracy of the measurements could further be improved by reducing the ToF drift. The ToF drift has two components: macro and micro ToF drifts. Fig. 5.7(left) shows a typical macro ToF drift over 36 hrs with the DAQ time of 60 s for each measurements, while Fig. 5.7(right) shows a micro drift for first 6 hours of the macro drift. The macro ToF drift is caused predominately by thermal expansion and contraction of the Titanium structures as shown in Fig. 3.26, while the micro and nano drift is assumed to be due to longterm and shortterm voltage instabilities of the MRTOF.

The macro drift is usually non-linear but is enough slow, $\sim 3 \times 10^{-7}$ /hrs in Fig. 3.26, to compensate by reference measurements. However, the micro and nano drift is so quick that it is not so trustworthy to compensate. The standard deviation from the average caused by the micro drift is $\sim 7 \times 10^{-7}$ which dominantly limits mass precision and accuracy.

The temperature of the Titanium structures are presently uncontrolled. By laying a water pipe around the MRTOF chamber or the Titanium support itself and flowing water with a well-controlled temperature, the macro drift would be suppressed.

The MRTOF voltages are now well-controlled by a PID system, and mirror voltages are biased by voltages that are provided by a resistive divider chain built from high-resistance resistors. The resistive-divider voltage supply allows to be less relative voltage drift, while it is difficult to change the mirror voltages remotely and to find an optimum mirror voltage setting experimentally. Therefore, to find even better potential configurations, full utilization of individual power supplies could be useful. It costs more and will require slightly more complicated cabling, but it will be worthwhile to develop.

6 Ongoing MRTOF projects

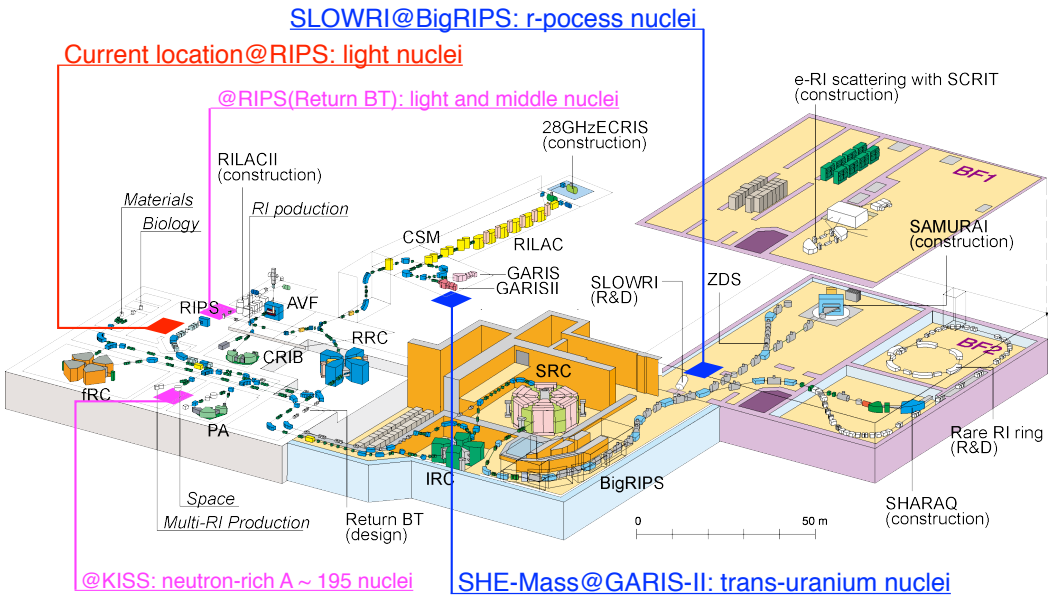

Figure 6.1: A bird's-eye view of the RIBF accelerator facility. Current MRTOF location is indicated by a red square behind RIPS second dipole magnet, ongoing-project locations are indicated by blue squares below GARIS-II separator [92] (SHE-Mass project) and nearby BigRIPS separator [25] (SLOWRI project), and possible future locations are indicated by pink squares at KISS system [93] and at RIPS with return-beam transport line from IRC [94]. The MRTOF can be moved to these locations and brought into operation within a few days.

At present, direct mass measurements of radioactive nuclei are primarily performed in four ways: single-pass time-of-flight, storage rings, Penning traps, and MRTOF. Of these, the Penning trap is currently considered the gold standard for precision and accuracy. However, the MRTOF is capable of comparable precision and accuracy in the case of $T_{1/2} \ll 1$ s. In principle, the MRTOF can make a meaningful mass measurement with even a single ion, making it competitive with storage rings as well.

In addition to having capabilities comparable to both Penning traps and storage rings, the MRTOF is reasonably portable. The RIKEN MRTOF was initially assembled and tested offline in the 3rd basement (below BigRIPS in Fig. 6.1), and moved to its current location at RIPS while mounted on the frame, then recovered within a few days.

Having demonstrated the functionality of the MRTOF, we will now discuss plans for its utilization at RIKEN. For now, there are two ongoing mass measurement projects: SHE-Mass project at GARIS separator for nuclei created via fusion-evaporation and SLOWRI project at BigRIPS separator for nuclei created via in-flight fission and fragmentation. Other possible future locations are expected at KISS system for neutron-rich nuclei near $A \sim 195$ and at RIPS with return-beam transport line for light and medium mass nuclei.

6.1 Mass measurements of trans-uranium nuclei

One of most importance subjects in nuclear physics is whether or not the so-called "island of stability" exists. The existence of an island of stability is theoretically predicted around $N = 184, Z = 114$. Within a classical framework, nuclei heavier than uranium cannot exist due to the very strong coulomb repulsive force. In the 1960's, however, Glenn T. Seaborg proposed the possibility of islands of stability within a quantum framework.

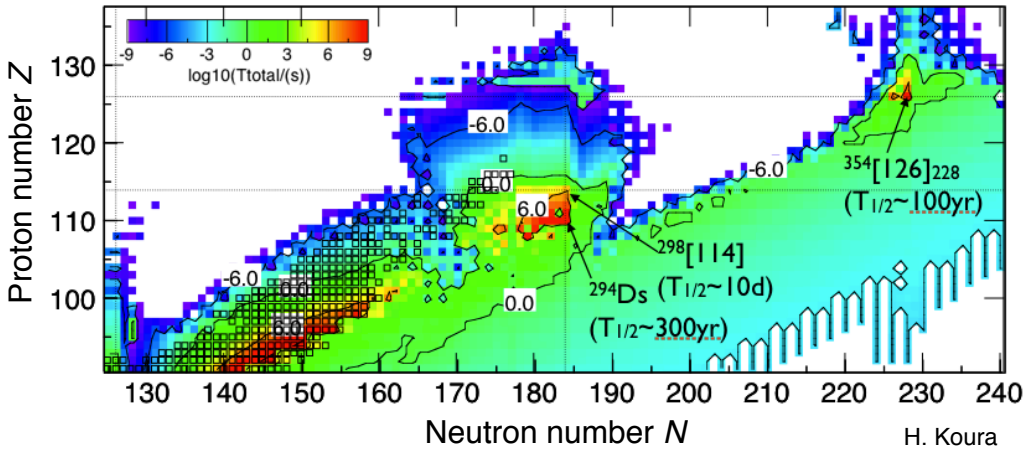

Figure 6.2: A section of the nuclear chart showing the region of superheavy nuclei with half-lives calculated by KUTY mass formula. Open squares indicate known nuclei. Half-lives are indicated by log-scaled color. According to KUTY mass formula, the region whose half-life can reach about 300 years will exist around spherical shell closure, $Z = 114$ and $N = 184$.

A campaign of mass measurements of trans-uranium nuclei with the MRTOF, which is named "SHE-Mass" project, is now under development. Trans-uranium nuclei will be provided from a compact gas catcher and transport system coupled with the gas-filled recoil separator GARIS-II. Figure 6.4 shows a schematic view of the system. In a compact 20-cm gas cell installed at the focal plane of GARIS-II, high-energy beam will be decelerated and thermalized by 100 mbar helium gas. The ions will be efficiently extracted as a low-energy beam by an RF-carpet and transported through a differential pumping section by an octupole ion guide. Continuous ion beam will first be trapped in a flat trap, then ejected perpendicularly and sent to the flat trap of MRTOF via a 3 m long transport line; rough mass separation will be performed by time of flight using a pair of steering electrodes which can be pulsed. The transported ions can then be recaptured in the taper trap and the flat trap for final preparation before performing time-of-flight measurements with the MRTOF. Current preparation traps and MRTOF will be utilized for this project.

In the first SHE-Mass campaign, the masses of elements up to Lawrencium will be measured directly. The candidate nuclei are shown in Fig. 6.5. These nuclei are produced with fusion-evaporation reactions, therefore the primary beam and target must be changed depending on compound nuclei and evaporation process.

For Einsteinium isotopes, a primary beam of ^{48}Ca will be used with a Gold target. For Fermium isotopes, a primary beam of ^{40}Ar will be used with a Lead target. For Mendelevium isotopes, a primary beam of ^{48}Ca will be used with Thallium target. For Nobelium isotopes, primary beams of ^{48}Ca and ^{22}Ne will be used with Lead and Uranium targets, respectively. For Lawrencium isotopes, primary beams of ^{48}Ca and ^{14,15}N will be used with Bismuth and Curium targets, respectively. Six nuclei, $^{252-255}$No and $^{255-256}$Lr, have been already measured directly with the Penning trap mass spectrometer SHIPTRAP, therefore these nuclei will be used to cross-check the accuracy of the system.

To perform these measurements, the system efficiency will be an important parameter because the cross section of candidate nuclei is typically on the order of nanobarns. Prior to construct of the system, the system efficiency has been estimated as listed in Table 6.1. The total efficiency, including

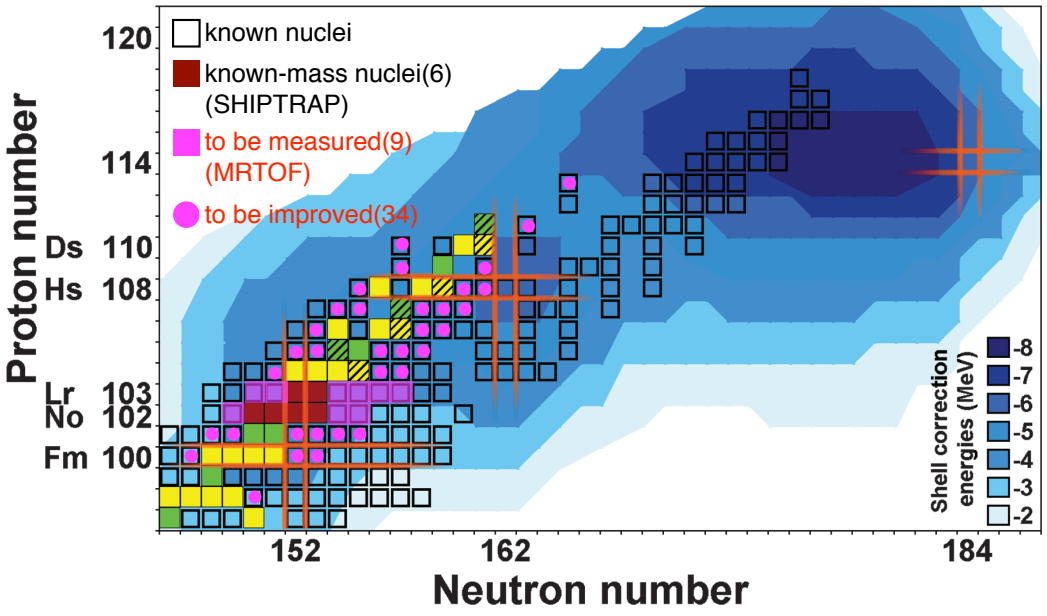

Figure 6.3: A section of the nuclear chart showing the region of superheavy nuclei candidates of the SHE-Mass project. Open squares indicate known nuclei. Red squares indicate nuclei whose masses have been measured directly by the Penning trap mass spectrometer SHIPTRAP. Pink squares indicate nuclei to be measured directly with MRTOF and pink circles indicate nuclei whose masses will be indirectly improved by direct mass measurements with MRTOF in the first SHE-Mass campaign.

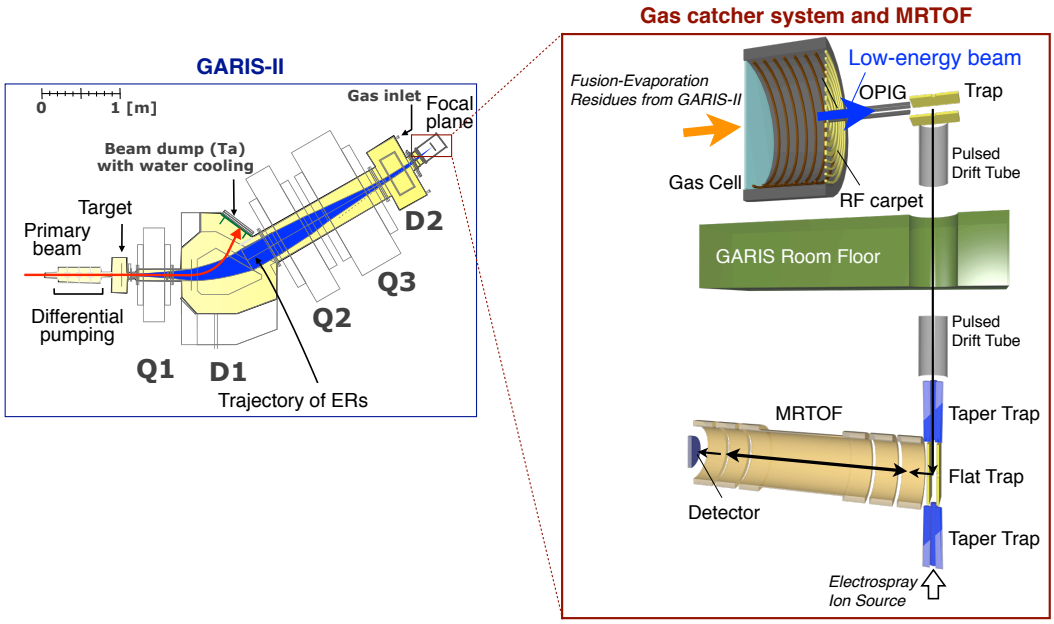

Figure 6.4: Schematic view of the SHE-Mass setup. The MRTOF and the preparation traps will be the same ones used in the current setup. Trans-uranium nuclei produced by fusion-evaporation reactions will be separated and transported by GARIS-II. High-energy beam from GARIS-II will be converted to a low-energy beam by a compact gas catcher system. The ions will initially be trapped in a flat trap after passing through an OPIG, then will be ejected perpendicularly and transported to the flat trap of the MRTOF. Expanded region shows orthogonal view.

that of GARIS-II, has been estimated to be 0.5-30%. The wide range is mostly a result of the efficiency of GARIS-II having a strong dependence on the reaction symmetry.

Table 6.1: Efficiency estimation for each section in the SHE-Mass setup. The total efficiency is estimated as 0.5-30% corresponding to two order of magnitude higher than SHIPTRAP efficiency. Sections which have been already constructed or experimentally evaluated are indicated by stars.

section	efficiency	
GARIS-II*	10 - 80%	depending on the reaction asymmetricity
Gas cell		
Degrader transmission	>80%	depending on the range in the degrader
Stopping fraction	>80%	depending on the energy loss in the degrader
Transport (in 4 ms)	>80%	
Extraction by rf-carpet*	∼100%	
Charge states*	>30%	assuming 1+, 2+ and neutral
Molecular sidebands*	>70%	based on gas cell experiments at MSU
OPIG*	∼100%	
Flat trap*	∼75%	gain for heavier ions
4-m transport	∼100%	with rough mass separation by time of flight
Taper trap and Flat trap*	∼75%	gain for heavier ions
MRTOF*	∼100%	
Detector*	∼85%	assuming MagneTOF detector
Total	0.5-30%	

Sections indicated with an asterisk in Table 6.1 have already been constructed or experimentally evaluated. Sections which which still require development and evaluation include the compact gas cell and 4-m transport section. A prototype of the compact gas cell is now being tested offline. The simulation of 4-m transport line is now ongoing.

6.2 Mass measurements of r-process nuclei

The origin of elements heavier than Iron is not trivial to answer. Since the famous B^2FH paper of 1957 [95], it has been assumed that heavy elements were synthesized in astrophysical processes featuring cycles of neutron capture followed by β-decay; details remain uncertain.

In low neutron flux environments, such as AGB stars, the slow neutron capture process (s-process) occurs over timescales of millennia. Subsequent neutron captures occur on timescale of decades to centuries, confining the process to a path very near the valley of nuclear stability. Due to the near-to-stable participant nuclei, the s-process is very well understood. It accounts for roughly half of the observed heavy element abundances, though it is unable to produce Thorium and Uranium.

A second process, referred to as the rapid neutron capture process (r-process), occurs under momentary, violent conditions of intense neutron flux. Several scenarios for the synthesis of such heavy elements have been developed; more than half of these elements are considered to be due to the rapid neutron capture process (r-process) which could occur during super novae explosions or neutron star mergers [96]. Under high-temperature and -pressure conditions, the high neutron flux results in sequential neutron captures on sub-millisecond timescales, driving the process far from the valley of stability. As the neutron-rich nuclei beta-decay, the number of protons increases toward superheavy elements. Though such an explosive reaction chain cannot be reproduced in the laboratory, one can simulate the process if relevant nuclear data are known. Unfortunately, little is known about the nuclei around the supposed r-process pathway, and the accuracies of present nuclear theory are far inadequate. The pathway of the r-process is a function of nuclear masses that determines the isotope of each element where equilibrium between neutron capture and photon-induced neutron emission occurs.

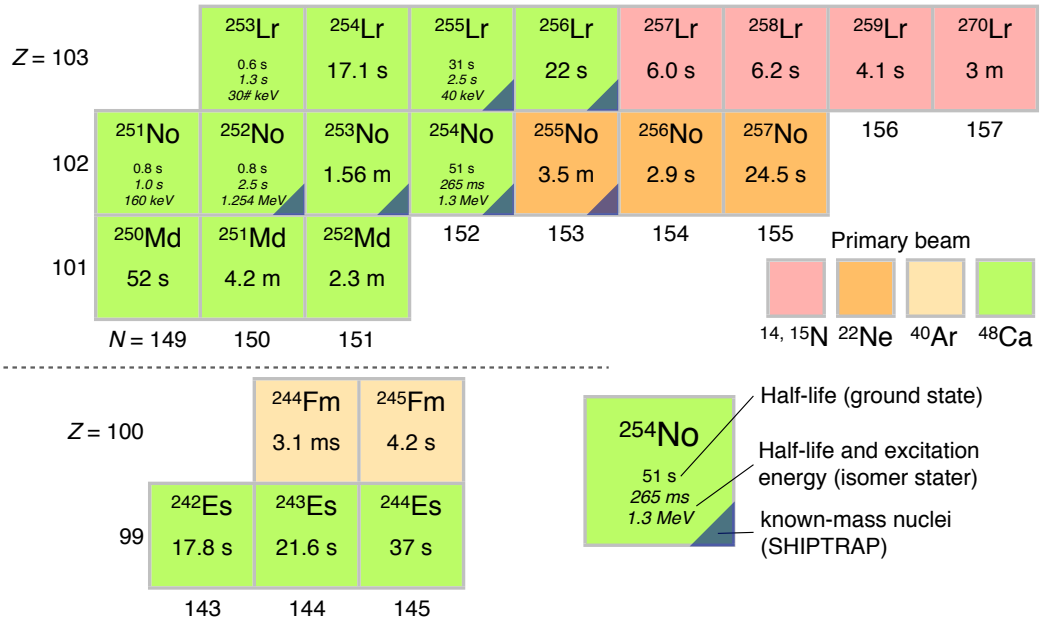

Figure 6.5: Candidates for first SHE-Mass campaign. In the initial campaign 23 nuclei, from Einsteinium to Lawrencium, will be measured directly. Six nuclei, indicated with a blue corner, have previously been measured by the Penning trap mass spectrometer SHIPTRAP and will serve as an accuracy cross-check.

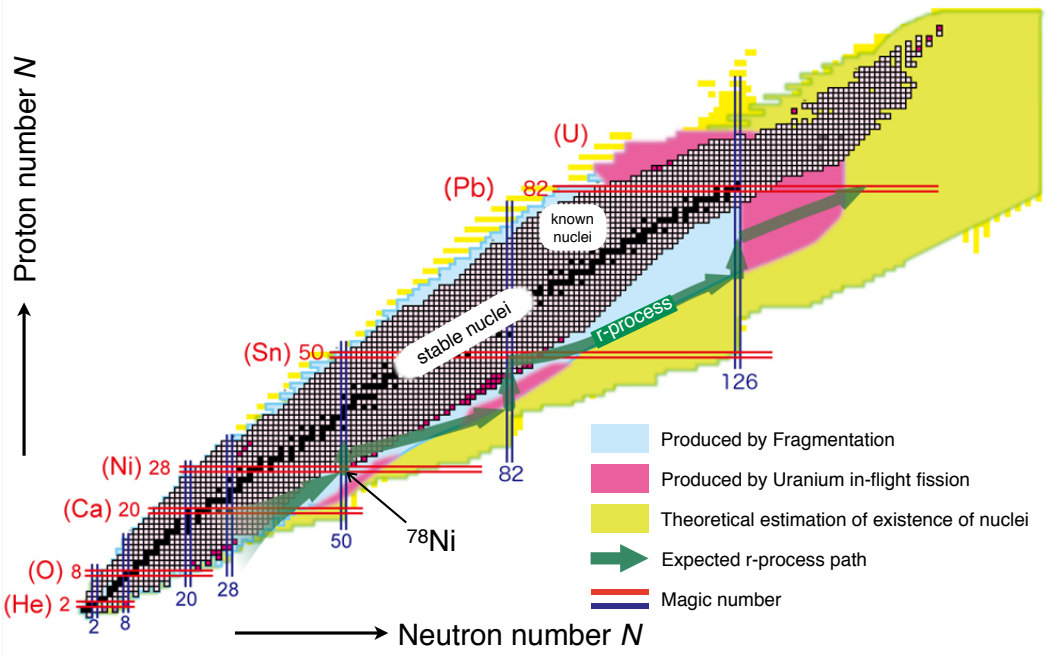

Figure 6.6: Nuclear chart with an expected r-process path (green line). Closed squares indicate stable nuclei, open squares indicate known nuclei, areas colored by light blue and pink are regions expected to be provided by fragmentation and Uranium in-flight fission reactions at RIBF.

Understanding this pathway is vital to understanding its contribution to elemental abundances.

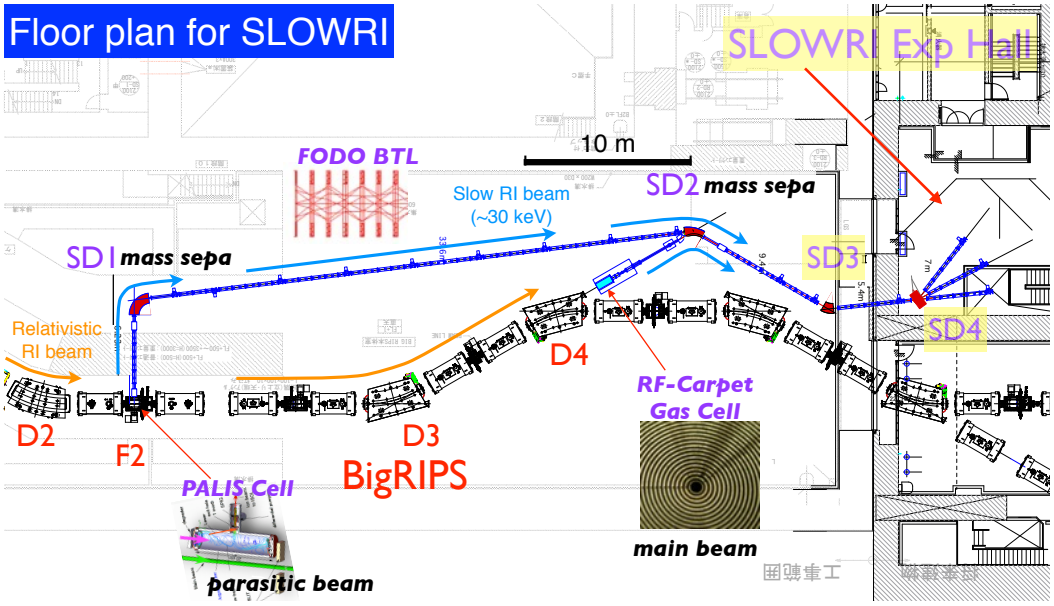

Figure 6.7: The floor plan for SLOWRI at RIBF/BigRIPS. The relativistic RI-beam provided from BigRIPS is converted to a low-energy beam via two gas cells; one is an Argon-filled gas cell featuring laser ionization (PALIS gas cell), another is an Helium-filled gas cell utilizing ion-guide techniques (RF-carpet gas cell). Beam lines connected to each gas cell are merged at the SD2 magnet and lead to an experimental hall.

RIKEN RIBF can produce many (but not all) r-process nuclides, and provide them as a relativistic RI-beam. The soon-to-be-completed SLOWRI facility, which builds on more than a decade of work in the development of Helium-filled gas cells, will convert the relativistic RI-beam to a low-energy beam which is well-suited for precision spectroscopy. There are many important nuclei, of which ^{78}Ni ($Z = 28$, $N = 50$) – expected to be a doubly-magic nuclide and the first r-process waiting point – is one of most important. Recently, RIBF has produced ^{78}Ni and nearby nuclei along the presumed r-process pathway with sufficient intensity to precisely measure their half-lives. We will start precise mass measurements of these nuclei, in the region where the r-process begins, using our newly developed multi-reflection time-of-flight mass spectrograph which is well-suited for short-lived, low-yield rare isotopes.

We have developed a new precision mass measurement method, multi-reflection time-of-flight mass spectrograph (MRTOF) as described above. Ions accumulate and cool in an ion trap, then are transferred to a pair of electrostatic ion mirrors, between which they reflect for some time before being released to travel to a detector. Comparing the time of flight of an unknown ion with that of a well-known reference, the mass of the unknown can be determined with high-precision and accuracy. An initial online mass measurement of ^{8}Li, shown in Sec. 4.3, achieved an accurate relative precision of $\ll 10^{-6}$ with less than 200 detected ions, while offline studies of the ^{40}Ca/^{40}K doublet indicate that a relative precision and accuracy of 10^{-8} can be achieved with short flight times of $\approx$2.3 ms – ideal for mass measurements of short-lived nuclei.

We have recently devised a means to perform wide-band mass measurements with the MRTOF. Figure 6.8 shows a cocktail beam that can be delivered by RIBF/BigRIPS and a calculated spectrum for it, with the MRTOF centered on ^{70}Fe^{+}. While unusually ordered due to ions of varying mass number making different numbers of reflections, the various isobaric multiplets do not intermingle; such is a general feature. Using a single tune of BigRIPS, we should be able to measure 32 nuclei simultaneously. Of those nuclei, 13 could be of interest for the r-process but have mass uncertainties exceeding 100 keV: $^{67-68}$Mn, $^{67-70}$Fe, $^{68-72}$Co, and ^{75}Ni. By making a 2^{nd} measurement with the MRTOF centered on ^{74}Ni^{+}, we can add $^{73-74}$Ni and ^{74}Co without retuning BigRIPS.

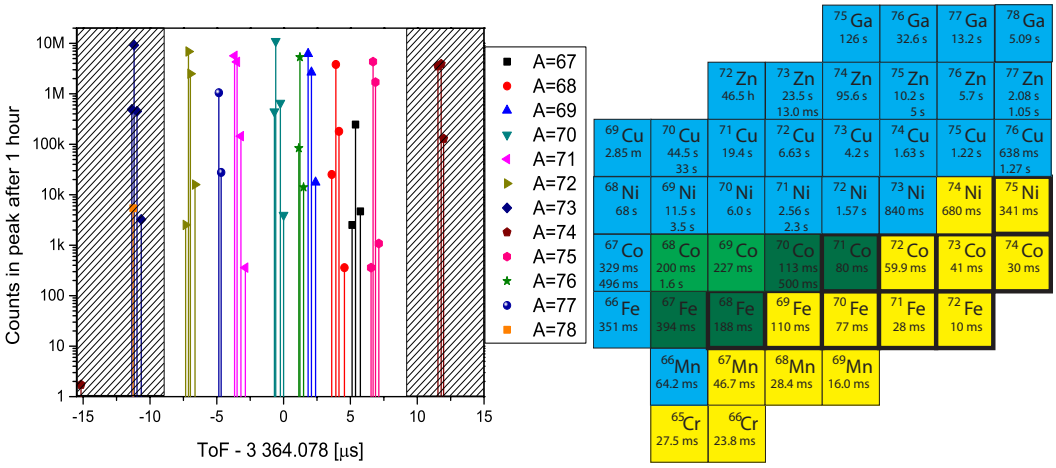

Figure 6.8: (left) Anticipated spectra from a single tune of BigRIPS centered on $^{70}Fe^{+}$, based on in-flight fission of a 10 pnA beam of ^{238}U. The hashed region indicates ions in the vicinity of a switched electrode resulting in reduced mass accuracy. (right) Cocktail beam from produced by a single tune of BigRIPS. Colors indicate present mass precision: (blue) $\delta m < 100$ keV, (green) $\delta m > 100$ keV, (yellow) no data. Bold frames indicate r-process nuclei.

We hope to eventually measure the masses of all r-process nuclei. At present, however, RIBF can provide sufficient intensities for us to measure nearly all candidate r-process nuclei between ^{78}Ni and ^{132}Sn, by making a small number of wide-band mass measurements. These precision mass measurements will allow models to focus on the secondary effects of the r-process site conditions. This will hopefully lead to better determination of the r-process site.

In FY2014 we hope to install the MRTOF directly after the large gas cell as shown in Fig. 6.9. In this time we will be able to use the MRTOF to study the cleanliness of the gas cell – are significant amounts of stable molecular ions extracted? In what charges states are radioactive ions extracted? Are radioactive ions extracted as atomic or molecular ions? In FY2014 we would also hope to perform first offline testing of the large gas cell. By using a spark-gap or fission source in the gas cell, we will be able to probe the cleanliness of the system by ionizing the gas and extracting the ions. Stable molecular ions extracted with too high intensity could potentially fill the ion trap used to prepare ions for the MRTOF, while a low intensity yield of stable molecular ions may be useful as reference species for mass measurements. In such tests, we would be able to make use of the MRTOF initially for identification of extracted ions.

The MRTOF will be vital to the initial commissioning efforts. By enabling us to definitively identify molecular ions, the MRTOF will allow us to differentiate between, *e.g.*, air leaks, water contamination and oil contaminations in the gas cell, the correction of which will be vital to achieving highest possible efficiency. The MRTOF will, furthermore, allow us to definitively determine the molecular state of any extracted radioactive ions. This will be particularly important in the initial commissioning, as active chemistry could limit the ability to perform wide-band mass measurements.

By the end of FY2014 we should make a "Day-Zero" commissioning with ^{72}Ni beam to study gas cell efficiency and behavior in online conditions. For such a Day-Zero test, the MRTOF will provide primary analysis of the gas cell's chemical behavior with the transition metals Fe, Co, and Ni.

In FY2015 we would have first online tests of the gas cell and MRTOF. Using a Uranium primary beam we could produce rather intense beams in the vicinity of ^{78}Ni. As masses of Ni isotopes more stability than ^{78}Ni are unknown, we would start with a cocktail beam as shown in Fig. 6.6(right) before adjusting BigRIPS to provide a cocktail beam as shown in Fig. 6.10(left). Continuing in this fashion, we will measure r-process nuclei from ^{78}Ni to ^{132}Sn. This could, in principle, be accomplished with as few as 6 different settings of the BigRIPS fragment separator and 2 weeks of mass measurements. The technique can then be used to study other portions of the nuclear chart as well.

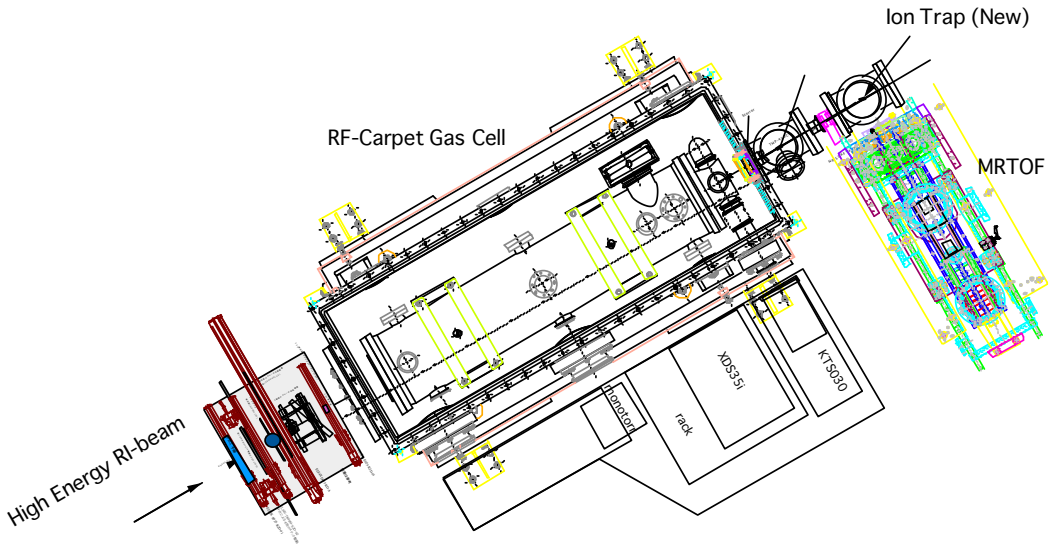

Figure 6.9: Experimental setup with MRTOF mass spectrograph directly connected to the rf-carpet gas cell via an ion trap. The setup will accept ions passing straight through the D4 magnet at BigRIPS.

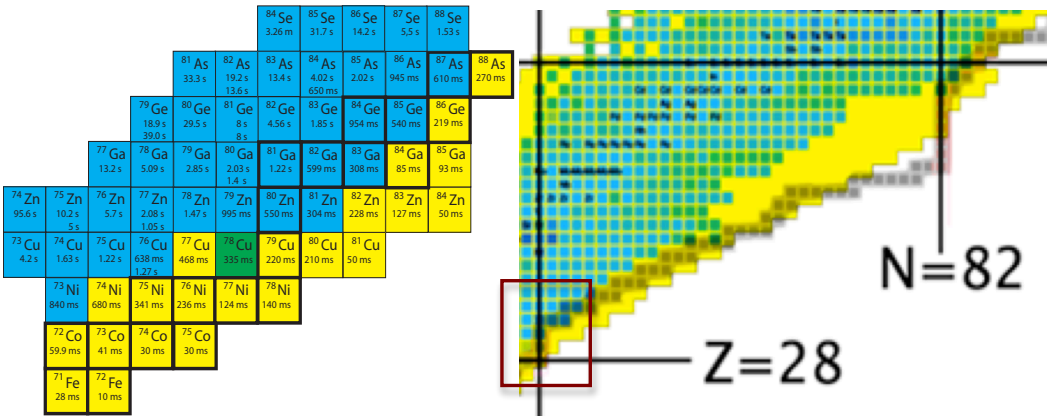

Figure 6.10: (Left) Isotope mixture that can be delivered to the MRTOF with BigRIPS centered on ^{78}Ni. Masses of all isotopes could be measured in less than 1 day. Colors indicate present mass precision: (blue) $\delta m < 100$ keV, (green) $\delta m > 100$ keV, (yellow) no data. Bold frames indicate r-process nuclei. (Right) Accessible region between ^{78}Ni and ^{132}Sn. The black pathway represents the likely r-process pathway. The red box indicates the area shown at left.

Comprehensive mass measurements of short-lived neutron-rich nuclei contribute significantly to solve the origin of heavy elements, especially for determining the r-process pathway. It will ignite more precise studies of r-process and nuclides related to the r-process. When nuclear masses and half-lives of relevant nuclei are provided, the r-process can be calculated mainly from the experimental data. One can find real physics in the discrepancy between the calculation and the abundance. For example, what effect is missing in the present r-process model? The demand for more precise data, such as the branching ratio of delayed-neutron emission will be emphasized. The combination of RIBF/BigRIPS, SLOWRI and MRTOF is also suitable for such precise nuclear data measurements.

7 Summary and outlook

The atomic mass is a global property that reflects the net result of all interactions at work in the atom. Information concerning nuclear structure can be derived from examination of the binding energies and such information is particularly important for nuclear structure studies and as an input to solve the pathway of the nucleosynthesis. At present, for direct mass measurements of radioactive nuclei, the Penning trap is widely used and considered the gold standard for precision and accuracy. However, the MRTOF is capable of comparable precision and accuracy in the case of $T_{1/2} \ll 100$ ms. In principle, the MRTOF can make a meaningful mass measurement with even a single ion, making it competitive with storage rings as well.

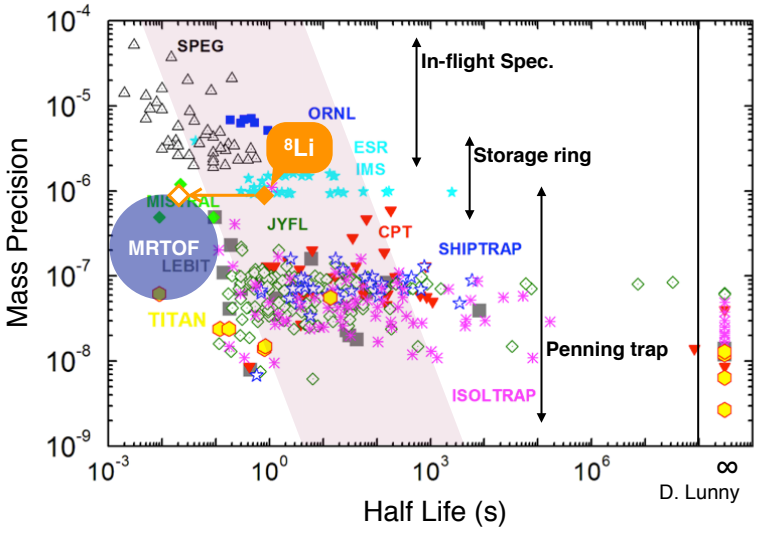

Figure 7.1: Map of the mass precision vs. the half life for various mass measurements in the last decades. The ranges of the mass precision for three measurement techniques are indicated by arrows and the target area of the MRTOF is also indicated by circle: the mass precision from below 10^{-6} to the order of 10^{-8} and the half life of <100 ms. The closed orange diamond indicates the position of the current online mass measurement of ^{8}Li, and the opened one indicates the actual time required for the measurement: ∼18 ms (7 ms for accumulation, 3 ms for cooling and ∼8 ms for ToF)

Through offline developments and online measurements using radioactive ^{8}Li, we achieved sub-ppm mass precision with <10 ms measurements, competitive with Penning traps. In the analysis to derive the mass, we employed a single-reference analysis which allows to compensate the ToF drift and derive the mass simply. The result is compared with various measurements in the last decades in Fig. 7.1. The ranges of the mass precision for three measurement techniques are indicated by arrows. Obviously, there is a general trend so far: the shorter the life-time, the poorer the mass precision. It is difficult to achieve the mass precision of $<10^{-6}$ for the half-life of <10 ms except for a few data of very light nuclei. The target area of the MRTOF is indicated by circle: the mass precision from below 10^{-6} to the order of 10^{-8} and the half life of <100 ms. The closed orange diamond indicates the position of the current online mass measurement of ^{8}Li, and the opened one indicates the actual time required for the measurement: ∼18 ms (7 ms for accumulation, 3 ms for cooling and ∼8 ms for ToF).

For future masss measurements, especially for trans-Uranium nuclei, an electrospray ionization (ESI) ion source combined with an rf-carpet was developed. The ESI ion source can be a powerful reference source, especially for mass measurements of trans-Uranium nuclei which have no stable elements. By

combining with the MRTOF, molecular ions up to 245 u were identified and most of them have isobaric molecules.

For now, there are two ongoing mass measurement projects: SHE-Mass project at GARIS separator for investigation of superheavy elements and SLOWRI project at BigRIPS separator for investigation of r-process nuclei. Other possible future locations are expected at KISS system and at RIPS without constructing new MRTOF, since the MRTOF is reasonably portable and easily moved from place to place; disassembling, moving and recovering are done within a few days.

We strongly believe knowledge of nuclear physics coming from mass measurements of short-lived nuclei could be dramatically expanded by mass measurements with the MRTOF.

Acknowledgements

The results in this thesis are certainly not the result of my efforts alone, nor are they derived solely from the efforts of the research group which I have been lucky enough to have been a part of. Without the many supports at the RIKEN Nishina Center and the RIBF accelerator crew who provided the accelerated beams for us to work with. I want to thank everyone at the RIKEN Nishina Center for being such great team players.

First I would like to express heartfelt gratitude my supervisor Dr. Michiharu Wada who always gave me the teaching of an innumerable amount of physics, experimental techniques, insightful advice and guidances, encouragements with lots of patience, and the opportunity for me to join SLOWRI team. I would also like to express immense gratitude to Dr. Peter Schury who taught me a lot of physics and experimental techniques, and provided a lot of helpful suggestions and discussions with my bad English. I also learned a lot of American cultures without leaving the U.S. at all. My special thanks belong to the core members of our experiments and SLOWRI team, Dr. Sarah Naimi, Dr. Tetsu Sonoda, Dr. Aiko Takamine, Dr. Kunihiro Okada and Prof. Hermann Wollnik. I am also very grateful to all other collaborators of the experiments. I appreciate Prof. Akira Ozawa who was my supervisor in master course and gave me useful discussions and advices for research and thesis. I would also like to thank the graduated students in SLOWRI team and Univ. of Tsukuba, and the staff belong to the low-energy nuclear physics group at Univ. of Tsukuba.

On a more personal note, I would like to express my cordial gratitude to my parents for encouraging my curiosity when I was young and instilling me with a desire for education and a strong work ethic. And also for never asking me when I would get a real job. Especially I would like to say grace to my father, who passed away in May 2011. Ifll never forget his love and kindness.

Especially I would like to say grace to my father, who passed away in May 2011. I'll never forget his love and kindness.

Bibliography

[1] K. Blaum, High-accuracy mass spectrometry with stored ions, Physics Reports 425 (2006) 1.

[2] E. Kugler, The isolde facility, Hyperfine Interactions 129 (1-4) (2000) 23–42. doi:10.1023/A:1012603025802.

[3] P. Bricault, R. Baartman, M. Dombsky, A. Hurst, C. Mark, G. Stanford, P. Schmor, Triumf-isac target station and mass separator commissioning, Nuclear Physics A 701 (1–4) (2002) 49 – 53. doi:http://dx.doi.org/10.1016/S0375-9474(01)01546-9.

[4] C. Davids, B. Back, K. Bindra, D. Henderson, W. Kutschera, T. Lauritsen, Y. Nagame, P. Sugathan, A. Ramayya, W. Walters, Startup of the fragment mass analyzer at ATLAS, Nuclear Instruments and Methods in Physics Research Section B: Beam Interactions with Materials and Atoms 70 (1–4) (1992) 358 – 365.

[5] S. Hofmann, G. Münzenberg, The discovery of the heaviest elements, Rev. Mod. Phys. 72 (2000) 733–767. doi:10.1103/RevModPhys.72.733.

[6] Y. T. Oganessian, V. K. Utyonkoy, Y. V. Lobanov, F. S. Abdullin, A. N. Polyakov, I. V. Shirokovsky, Y. S. Tsyganov, G. G. Gulbekian, S. L. Bogomolov, A. N. Mezentsev, S. Iliev, V. G. Subbotin, A. M. Sukhov, A. A. Voinov, G. V. Buklanov, K. Subotic, V. I. Zagrebaev, M. G. Itkis, J. B. Patin, K. J. Moody, J. F. Wild, M. A. Stoyer, N. J. Stoyer, D. A. Shaughnessy, J. M. Kenneally, R. W. Lougheed, Experiments on the synthesis of element 115 in the reaction ^{243}Am(^{48}Ca, xn)$^{291-x}$115, Phys. Rev. C 69 (2004) 021601. doi:10.1103/PhysRevC.69.021601.

[7] V. Ninov, K. E. Gregorich, C. A. McGrath, The berkeley gas-filled separator, AIP Conference Proceedings 455 (1998) 704.

[8] K. Morita, K. Morimoto, D. Kaji, T. Akiyama, S. ichi Goto, H. Haba, E. Ideguchi, R. Kanungo, K. Katori, H. Koura, H. Kudo, T. Ohnishi, A. Ozawa, T. Suda, K. Sueki, H. Xu, T. Yamaguchi, A. Yoneda, A. Yoshida, Y. Zhao, Experiment on the synthesis of element 113 in the reaction ^{209}bi(^{70}zn,n)^{278}113, Journal of the Physical Society of Japan 73 (10) (2004) 2593–2596.

[9] H. Geissel, P. Armbruster, K. Behr, A. Brünle, K. Burkard, M. Chen, H. Folger, B. Franczak, H. Keller, O. Klepper, B. Langenbeck, F. Nickel, E. Pfeng, M. Pfützner, E. Roeckl, K. Rykaczewski, I. Schall, D. Schardt, C. Scheidenberger, K.-H. Schmidt, A. Schröter, T. Schwab, K. Sümmerer, M. Weber, G. Münzenberg, T. Brohm, H.-G. Clerc, M. Fauerbach, J.-J. Gaimard, A. Grewe, E. Hanelt, B. Knödler, M. Steiner, B. Voss, J. Weckenmann, C. Ziegler, A. Magel, H. Wollnik, J. Dufour, Y. Fujita, D. Vieira, B. Sherrill, The {GSI} projectile fragment separator (frs): a versatile magnetic system for relativistic heavy ions, Nuclear Instruments and Methods in Physics Research Section B: Beam Interactions with Materials and Atoms 70 (1992) 286.

[10] D. Morrissey, B. Sherrill, M. Steiner, A. Stolz, I. Wiedenhoever, Commissioning the a1900 projectile fragment separator, Nuclear Instruments and Methods in Physics Research Section B: Beam Interactions with Materials and Atoms 204 (0) (2003) 90 – 96.

[11] T. Kubo, M. Ishihara, N. Inabe, H. Kumagai, I. Tanihata, K. Yoshida, T. Nakamura, H. Okuno, S. Shimoura, K. Asahi, The {RIKEN} radioactive beam facility, Nuclear Instruments and Methods in Physics Research Section B: Beam Interactions with Materials and Atoms 70 (1–4) (1992) 309 – 319. doi:http://dx.doi.org/10.1016/0168-583X(92)95947-P.

[12] A. Lépine-Szily, Experimental overview of mass measurements, Hyperfine Interactions 132 (1-4) (2001) 35–57. doi:10.1023/A:1011940932323.

[13] W. Mittig, A. Lépine-Szily, N. A. Orr, Mass measurement far from stability, Annual Review of Nuclear and Particle Science 47 (1) (1997) 27–66. doi:10.1146/annurev.nucl.47.1.27.

[14] H. Ravn, P. Bricault, G. Ciavola, P. Drumm, B. Fogelberg, E. Hagebø, M. Huyse, R. Kirchner, W. Mittig, A. Mueller, H. Nifenecker, E. Roeckl, Comparison of radioactive ion-beam intensities produced by means of thick targets bombarded with neutrons, protons and heavy ions, Nuclear Instruments and Methods in Physics Research Section B: Beam Interactions with Materials and Atoms 88 (4) (1994) 441 – 461. doi:http://dx.doi.org/10.1016/0168-583X(94)95397-X.

[15] B. Jonson, A. Richter, More than three decades of isolde physics, Hyperfine Interactions 129 (1-4) (2000) 1–22. doi:10.1023/A:1012689128103.

[16] R. Kirchner, Review of isol target–ion-source systems, Nuclear Instruments and Methods in Physics Research Section B: Beam Interactions with Materials and Atoms 204 (0) (2003) 179 – 190.

[17] U. Koster, Intense radioactive-ion beams produced with the isol method, European Physcal Journal A 15 (2002) 255.

[18] M. Lindroos, Future plans at isolde, Nuclear Instruments and Methods in Physics Research Section B: Beam Interactions with Materials and Atoms 204 (0) (2003) 730.

[19] J. Aysto, Development and applications of the IGISOL technique, Nuclear Physics A 693 (2001) 477.

[20] A. Semchenkov, W. Brüchle, E. Jäger, E. Schimpf, M. Schädel, C. Mühle, F. Klos, A. Türler, A. Yakushev, A. Belov, T. Belyakova, M. Kaparkova, V. Kukhtin, E. Lamzin, S. Sytchevsky, The transactinide separator and chemistry apparatus (tasca) at gsi – optimization of ion-optical structures and magnet designs, Nuclear Instruments and Methods in Physics Research Section B: Beam Interactions with Materials and Atoms 266 (2008) 4153.

[21] A. Yeremin, A. Andreyev, D. Bogdanov, G. Ter-Akopian, V. Chepigin, V. Gorshkov, A. Kabachenko, O. Malyshev, A. Popeko, R. Sagaidak, S. Sharo, E. Voronkov, A. Taranenko, A. Lavrentjev, The kinematic separator vassilissa performance and experimental results, Nuclear Instruments and Methods in Physics Research Section A: Accelerators, Spectrometers, Detectors and Associated Equipment 350 (1994) 608.

[22] J. Knoll, J. Hüfner, A. Bouyssy, Nuclear Physics A 308 (1978) 500.

[23] T. Kubo, In-flight ri beam separator bigrips at riken and elsewhere in japan, Nuclear Instruments and Methods in Physics Research Section B: Beam Interactions with Materials and Atoms 204 (2003) 97.

[24] P. Dendooven, Nucl. Instr. and Meth. in Phys. Res. B 126 (1997) 182.

[25] M. Wada, Y. Ishida, T. Nakamura, Y. Yamazaki, T. Kambara, H. Ohyama, Y. Kanai, T. M. Kojima, Y. Nakai, N. Ohshima, A. Yoshida, T. Kubo, Y. Matsuo, Y. Fukuyama, K. Okada, T. Sonoda, S. Ohtani, K. Noda, H. Kawakami, I. Katayama, Slow ri-beams from projectile fragment separators, Nuclear Instruments and Methods in Physics Research Section B: Beam Interactions with Materials and Atoms 204 (2003) 570.

[26] A. Takamine, Precision laser spectroscopy of unstable beryllium isotopes using an rf ion guide system, PhD thesis.

[27] P. H. Dawson, Quadrupole mass spectrometry and its applications, AIP Press.

[28] H. J. Xu, M. Wada, J. Tanaka, H. Kawakami, I. Katayama, S. Ohtani, A new cooling and focusing device for ion guide, Nuclear Instruments and Methods in Physics Research Section A: Accelerators, Spectrometers, Detectors and Associated Equipment 333 (1993) 274.

[29] G. Audi, A. Wapstra, C. Thibault, The AME2003 atomic mass evaluation: (II). Tables, graphs and references, Nuclear Physics A 729 (2003) 337.

[30] P. Schury, G. Bollen, D. A. Davies, A. Doemer, D. Lawton, D. J. Morrissey, J. Ottarson, A. Prinke, R. Ringle, T. Sun, S. Schwarz, L. Weissman, Precision experiments with rare isotopes with lebit at msu, Eur. Phys. J. A 25 (2005) 51.

[31] P. Delahaye, G. Audi, K. Blaum, F. Carrel, S. George, F. Herfurth, A. Herlert, A. Kellerbauer, H. J. Kluge, D. Lunney, L. Schweikhard, C. Yazidjian, High-accuracy mass measurements of neutron-rich kr isotopes, Phys. Rev. C 74 (2006) 034331.

[32] J. J. Thomson, Bakerian lecture- rays of positive electricity, Proc. R. Soc. Lond. A 89 (1913) 1.

[33] G. Audi, The history of nuclidic masses and of their evaluation, International Journal of Mass Spectrometry 251 (2006) 85.

[34] R. Klapisch, R. Prieels, C. Thibault, A. M. Poskanzer, C. Rigaud, E. Roechl, Phys. Rev. Lett. 31 (1973) 118.

[35] D. M. Moltz, K. S. Toth, R. E. Tribble, R. E. Neese, J. P. Sullivan, Phys. Rev. C 26 (1982) 1914.

[36] H. Stolzenberg, S. Becker, G. Bollen, F. Kern, H. J. Kluge, T. Otto, G. Savard, L. Schweikhard, G. Audi, R. B. Moore, Accurate mass determination of short-lived isotopes by a tandem penning-trap mass spectrometer, Phys. Rev. Lett. 65 (1990) 3104.

[37] H. Savajols, Hyperfine Int. 132 (2001) 243.

[38] J. M. Wouters, D. J. Vieira, H. Wollnik, G. W. Butler, R. H. Kraus, K. Vaziri, Nucl. Instr. and Meth. in Phys. Res. B 26 (1987) 286.

[39] D. Bazin, J. Caggiano, B. Sherrill, J. Yurkon, A. Zeller, The S800 spectrograph, Nuclear Instruments and Methods in Physics Research Section B: Beam Interactions with Materials and Atoms 204 (2003) 629.

[40] A. S. Lalleman, G. Auger, W. Mittig, M. Chabert, M. Chartier, J. Fermé, A. Gillibert, A. Lṕine-Szily, M. Lewitowicz, M. H. Moscatello, N. A. Orr, G. Politi, F. Sarazin, H. Savajols, P. V. Isacker, A. C. C. Villari, Hyperfine Int. 132 (2001) 313.

[41] S. Issmer, M. Fruneau, J. A. Pinston, M. Asghar, D. Barnéoud, J. Genevey, T. Kerscher, K. E. G. Löbner, Eur. Phys. J. A 2 (1998) 173.

[42] J. Stadlmann, M. Hausmann, F. Attallah, K. Beckert, P. Beller, F. Bosch, H. Eickhoff, M. Falch, B. Franczak, B. Franzke, H. Geissel, T. Kerscher, O. Klepper, H. -J. Kluge, C. Kozhuharov, Yu. A. Litvinov, K. E. G. Löbner, M. Matoš, G. Müzenberg, N. Nankov, F. Nolden, Yu. N. Novikov, T. Ohtsubo, T. Radon, H. Schatz, C. Scheidenberger, M. Steck, H. Weick, H. Wollnik, Phys. Lett. B 586 (2004) 27.

[43] B. Schlitt, K. Beckert, T. Beha, H. Eickhoff, B. Franzke, H. Geissel, H. Irnich, H. C. Jung, T. F. Kerscher, O. Klepper, K. E. G. Löbner, G. Münzenberg, F. Nolden, Y. Novikov, T. Radon, H. Reich, A. Schwinn, M. Steck, K. Sümmerer, T. Winkler, H. Wollnik, Hyperfine Int. 99 (1996) 117.

[44] D. Lunney, C. Monsanglant, G. Audi, G. Bollen, C. Borcea, H. Doubre, C. Gaulard, S. Henry, M. deSaintSimon, C. Thibault, C. Toader, N. Vieira, Recent results on ne and mg from the mistral mass measurement program at isolde, Hyperfine Interactions 132 (2001) 297.

[45] P. M. Bradley, J. V. Porto, S. Rainville, J. K. Thompson, D. E. Pritchard, Penning trap measurements of the masses of ^{133}cs, $^{87,85}rb$, and ^{23}na with uncertainties $le0.2$ ppb, Phys. Rev. Lett. 83 (1999) 4510.

[46] G. Bollen, D. Davies, M. Facina, J. Huikari, E. Kwan, P. Lofy, D. Morrissey, A. Prinke, R. Ringle, J. Savory, P. Schury, S. Schwarz, C. Sumithrarachchi, T. Sun, L. Weissman, Experiments with thermalized rare isotope beams from projectile fragmentation: A precision mass measurement of the superallowed *beta* emitter $^{38}mathrmCa$, Phys. Rev. Lett. 96 (2006) 152501.

[47] M. Smith, M. Brodeur, T. Brunner, S. Ettenauer, A. Lapierre, R. Ringle, V. L. Ryjkov, F. Ames, P. Bricault, G. W. F. Drake, P. Delheij, D. Lunney, F. Sarazin, J. Dilling, First penning-trap mass measurement of the exotic halo nucleus ^{11}Li, Phys. Rev. Lett. 101 (2008) 202501.

[48] G. Bollen, S. Becker, H.-J. Kluge, M. K"onig, R. Moore, T. Otto, H. Raimbault-Hartmann, G. Savard, L. Schweikhard, H. Stolzenberg, ISOLTRAP: a tandem penning trap system for accurate on-line mass determination of short-lived isotopes, Nuclear Instruments and Methods in Physics Research Section A: Accelerators, Spectrometers, Detectors and Associated Equipment 368 (1996) 675.

[49] V. S. Kolhinen, T. Eronen, J. Hakala, A. Jokinen, S. Kopecky, S. Rinta-Antila, J. Szerypo, J. Äystö, Nucl. Instr. and Meth. in Phys. Res. B 204 (2003) 502.

[50] G. Savard, R. C. Barber, D. Beeching, F. Buchinger, J. E. Crawford, S. Gulick, X. Feng, E. Hagberg, J. C. Hardy, V. T. Koslowsky, J. K. P. Lee, R. B. Moore, K. S. Sharma, M. Watson, Nucl. Phys. A 626 (1997) 353.

[51] G. Sikler, D. Ackermann, F. Attallah, D. Beck, J. Dilling, S. A. Elisseev, H. Geissel, D. Habs, S. Heinz, F. Herfurth, F. Heßberger, S. Hofmann, H. -J. Kluge, C. Kozhuharov, G. Marx, M. Mukherjee, J. Neumayr, W. Plaß, W. Quint, S. Rahaman, D. Rodrŕguez, C. Scheidenberger, M. Tarisien, P. Thirolf, V. Varentsov, C. Weber, Z. Zhou, Nucl. Instr. and Meth. in Phys. Res. B 204 (2003) 482.

[52] R. Ringle, G. Bollen, D. Lawton, P. Schury, S. Schwarz, T. Sun, The lebit 9.4 t penning trap system, in: The 4th International Conference on Exotic Nuclei and Atomic Masses, 2005, p. 59.

[53] H. Wollnik, M. Przewloka, Time-of-flight mass spectrometers with multiply reflected ion trajectories, Int. J. Mass Spectrom. Ion Proc. 96 (1990) 267.

[54] Y. Ishida, M. Wada, Y. Matsuo, I. Tanihata, A. Casares, H. Wollnik, A time-of-flight mass spectrometer to resolve isobars, Nuclear Instruments and Methods in Physics Research Section B: Beam Interactions with Materials and Atoms 219 (2004) 468.

[55] R. Wolf, F. Wienholtz, D. Atanasov, D. Beck, K. Blaum, C. Borgmann, F. Herfurth, M. Kowalska, S. Kreim, Y. A. Litvinov, D. Lunney, V. Manea, D. Neidherr, M. Rosenbusch, L. Schweikhard, J. Stanja, K. Zuber, Isoltrap's multi-reflection time-of-flight mass separator/spectrometer, International Journal of Mass Spectrometry 349–350 (2013) 123.

[56] W. R. Plass, T. Dickel, C. Scheidenberger, Multiple-reflection time-of-flight mass spectrometry, International Journal of Mass Spectrometry 349–350 (2013) 134.

[57] Y. Ito, P. Schury, M. Wada, S. Naimi, T. Sonoda, H. Mita, F. Arai, A. Takamine, K. Okada, A. Ozawa, H. Wollnik, Single-reference high-precision mass measurement with a multireflection time-of-flight mass spectrograph, Phys. Rev. C 88 (2013) 011306(R).

[58] M. Dahan, R. Fishman, O. Heber, M. Rappaport, N. Altstein, D. Zajfman, W. J. van der Zande, A new type of electrostatic ion trap for storage of fast ion beams, Review of Scientific Instruments 69 (1998) 76.

[59] A. Piechaczek, V. Shchepunov, H. Carter, J. Batchelder, E. Zganjar, S. Liddick, H. Wollnik, Y. Hu, B. Griffith, Development of a high resolution isobar separator for study of exotic decays, Nuclear Instruments and Methods in Physics Research Section B: Beam Interactions with Materials and Atoms 266 (2008) 4510.

[60] F. Wienholtz, D. Beck, K. Blaum, C. Borgmann, M. Breitenfeldt, R. B. Cakirli, S. George, F. Herfurth, J. D. Holt, M. Kowalska, S. Kreim, D. Lunney, V. Manea, J. Mene'ndez, D. Neidherr, M. Rosenbusch, L. Schweikhard, A. Schwenk, J. Simonis, J. Stanja, R. N. Wolf, K. Zuber, Masses of exotic calcium isotopes pin down nuclear forces, Nature 498 (2013) 346.

[61] T. Ohnishi, T. Kubo, K. Kusaka, A. Yoshida, K. Yoshida, M. Ohtake, N. Fukuda, H. Takeda, D. Kameda, K. Tanaka, N. Inabe, Y. Yanagisawa, Y. Gono, H. Watanabe, H. Otsu, H. Baba, T. Ichihara, Y. Yamaguchi, M. Takechi, S. Nishimura, H. Ueno, A. Yoshimi, H. Sakurai, T. Motobayashi, T. Nakao, Y. Mizoi, M. Matsushita, K. Ieki, N. Kobayashi, K. Tanaka, Y. Kawada, N. Tanaka, S. Deguchi, Y. Satou, Y. Kondo, T. Nakamura, K. Yoshinaga, C. Ishii, H. Yoshii, Y. Miyashita, N. Uematsu, Y. Shiraki, T. Sumikama, J. Chiba, E. Ideguchi, A. Saito, T. Yamaguchi, I. Hachiuma, T. Suzuki, T. Moriguchi, A. Ozawa, T. Ohtsubo, M. A. Famiano, H. Geissel, A. S. Nettleton, O. B. Tarasov, D. P. Bazin, B. M. Sherrill, S. L. Manikonda, J. A. Nolen, Identification of 45 new neutron-rich isotopes produced by in-flight fission of a 238u beam at 345 mev/nucleon, J. Phys. Soc. Jpn. 79 (2010) 073201.

[62] A. Takamine, M. Wada, Y. Ishida, T. Nakamura, K. Okada, Y. Yamazaki, T. Kambara, Y. Kanai, T. M. Kojima, Y. Nakai, N. Oshima, A. Yoshida, T. Kubo, S. Ohtani, K. Noda, I. Katayama, P. Hostain, V. Varentsov, H. Wollnik, Space-charge effects in the catcher gas cell of a rf ion guide, Review of Scientific Instruments 76 (2005) 103503.

[63] K. Okada, M. Wada, T. Nakamura, A. Takamine, V. Lioubimov, P. Schury, Y. Ishida, T. Sonoda, M. Ogawa, Y. Yamazaki, Y. Kanai, T. M. Kojima, A. Yoshida, T. Kubo, I. Katayama, S. Ohtani, H. Wollnik, H. A. Schuessler, Precision measurement of the hyperfine structure of laser-cooled radioactive $^{7}Be^{+}$ ions produced by projectile fragmentation, Phys. Rev. Lett. 101 (2008) 212502.

[64] P. Schury, K. Okada, S. Shchepunov, T. Sonoda, A. Takamine, M. Wada, H. Wollnik, Y. Yamazaki, Multi-reflection time-of-flight mass spectrograph for short-lived radioactive ions, Eur. Phys. J. A 42 (2009) 343.

[65] J. Dufour, R. D. Moral, H. Emmermann, F. Hubert, D. Jean, C. Poinot, M. Pravikoff, A. Fleury, H. Delagrange, K.-H. Schmidt, Projectile fragments isotopic separation: Application to the lise spectrometer at ganil, Nucl. Instr. and Meth. in Phys. Res. A 248 (1986) 267.

[66] LISE++, available at http://lise.nscl.msu.edu/lise.

[67] F. Herfurth, J. Dilling, A. Kellerbauer, G. Bollen, S. Henry, H.-J. Kluge, E. Lamour, D. Lunney, R. Moore, C. Scheidenberger, S. Schwarz, G. Sikler, J. Szerypo, A linear radiofrequency ion trap for accumulation, bunching, and emittance improvement of radioactive ion beams, Nuclear Instruments and Methods in Physics Research Section A: Accelerators, Spectrometers, Detectors and Associated Equipment 469 (2001) 254.

[68] A. Kellerbauer, T. Kim, R. Moore, P. Varfalvy, Buffer gas cooling of ion beams, Nuclear Instruments and Methods in Physics Research Section A: Accelerators, Spectrometers, Detectors and Associated Equipment 469 (2001) 276.

[69] A. Nieminen, J. Huikari, A. Jokinen, J. Äystö, P. Campbell, E. Cochrane, Beam cooler for low-energy radioactive ions, Nuclear Instruments and Methods in Physics Research Section A: Accelerators, Spectrometers, Detectors and Associated Equipment 469 (2001) 244.

[70] Y. Ito, P. Schury, M. Wada, S. Naimi, C. Smorra, T. Sonoda, H. Mita, A. Takamine, K. Okada, A. Ozawa, H. Wollnik, A novel ion cooling trap for multi-reflection time-of-flight mass spectrograph, Nuclear Instruments and Methods in Physics Research Section B: Beam Interactions with Materials and Atoms 317, Part B (2013) 544.

[71] B. A. Mansoori, E. W. Dyer, C. M. Lock, K. Bateman, R. K. Boyd, B. A. Thomson, Analytical performance of a high-pressure radio frequency-only quadrupole collision cell with an axial field applied by using conical rods, J. Am. Soc. Mass Spectrom. 9 (1998) 775.

[72] SIMION8.0, available at http://www.simion.com.

[73] HeatWave Labs, available at http://www.cathode.com/.

[74] S. Naimi, S. Nakamura, Y. Ito, H. Mita, K. Okada, A. Ozawa, P. Schury, T. Sonoda, A. Takamine, M. Wada, H. Wollnik, An rf-carpet electrospray ion source to provide isobaric mass calibrants for trans-uranium elements, International Journal of Mass Spectrometry 337 (2013) 24.

[75] Dr. Gary Eiceman's group, http://web.nmsu.edu/ ionsrus/.

[76] K. Morimoto, K. Morita, D. Kaji, S. Goto, H. Haba, E. Ideguchi, R. Kanungo, K. Katori, H. Koura, H. Kudo, T. Ohnishi, A. Ozawa, J. Peter, T. Suda, K. Sueki, I. Tanihata, F. Tokanai, H. Xu, A. Yeremin, A. Yoneda, A. Yoshida, T.-L. Zhao, T. Zheng, Status of super heavy element research using garis at riken, Nuclear Physics A 738 (2004) 129.

[77] K. Morita, K. Morimoto, D. Kaji, H. Haba, K. Ozeki, Y. Kudou, T. Sumita, Y. Wakabayashi, A. Yoneda, K. Tanaka, S. Yamaki, R. Sakai, T. Akiyama, S. Goto, H. Hasebe, M. Huang, T. Huang, E. Ideguchi, Y. Kasamatsu, K. Katori, Y. Kariya, H. Kikunaga, H. Koura, H. Kudo, A. Mashiko, K. Mayama, S. Mitsuoka, T. Moriya, M. Murakami, H. Murayama, S. Namai, A. Ozawa, N. Sato, K. Sueki, M. Takeyama, F. Tokanai, T. Yamaguchi, , A. Yoshida, New result in the production and decay of an isotope, ^{278}113, of the 113th element, J. Phys. Soc. Jpn. 81 (2012) 103201.

[78] B. Mamyrin, Time-of-flight mass spectrometry (concepts, achievements, and prospects), International Journal of Mass Spectrometry 206 (2001) 251.

[79] M. Berz, Differential algebraic description of beam dynamics to very high orders differential algebraic description of beam dynamics to very high orders, Particle Accelerators 24 (1989) 109.

[80] S. Schwarz, G. Bollen, D. Lawton, A. Neudert, R. Ringle, P. Schury, T. Sun, A second-generation ion beam buncher and cooler, Nuclear Instruments and Methods in Physics Research Section B: Beam Interactions with Materials and Atoms 204 (2003) 474.

[81] S. Schwarz, Ioncool—a versatile code to characterize gas-filled ion bunchers and coolers (not only) for nuclear physics applications, Nuclear Instruments and Methods in Physics Research Section A: Accelerators, Spectrometers, Detectors and Associated Equipment 566 (2006) 233.

[82] M. Wada, P. Schury, RIKEN Accel. Prog. Rep. 44.

[83] G. Taylor, A. D. McEwan, The stability of a horizontal fluid interface in a vertical electric field, Journal of Fluid Mechanics 22 (1965) 1.

[84] J. Fern'andez, I. G. Loscertales, The current emitted by highly conducting taylor cones, Journal of Fluid Mechanics 260 (1994) 155.

[85] L. Rayleigh, On the equilibrium of liquid conducting masses charged with electricity, Philosophical Magazine 14 (1882) 184.

[86] A. Gomez, K. Tang, Charge and fission of droplets in electrostatic sprays, Physics of Fluids 6 (1994) 404.

[87] J. V. Iribarne, B. A. Thomson, On the evaporation of small ions from charged droplets, The Journal of Chemical Physics 64 (1976) 2287.

[88] M. J. Koskelo, P. A. Aarnio, J. T. Routti, Sampo80: Minicomputerprogram for gamma spectrum analysis withnuclide identification, Comp. Phys. Commun. 24 (1981) 11.

[89] G. Audi, F. G. Kondev, M. Wang, B. Pfeiffer, X. Sun, J. Blachot, M. MacCormick, The NUBASE2012 evaluation of nuclear properties, Chin. Phys. C 36 (2012) 1157.

[90] R. Birge, The calculation of errors by the method of least squares, Phys. Rev. 40 (1932) 207.

[91] P. Schury, M. Wada, Y. Ito, F. Arai, S. Naimi, T. Sonoda, H. Wollnik, V. Shchepunov, C. Smorra, A high-resolution multi-reflection time-of-flight mass spectrograph at riken/slowri (2013).

[92] D. Kaji, K. Morimoto, N. Sato, A. Yoneda, K. Morita, Gas-filled recoil ion separator garis-ii, Nuclear Instruments and Methods in Physics Research Section B: Beam Interactions with Materials and Atoms.

[93] Y. Hirayama, Y. Watanabe, N. Imai, H. Ishiyama, S.-C. Jeong, H. Miyatake, M. Oyaizu, Y. H. Kim, M. Mukai, Y. Matsuo, T. Sonoda, M. Wada, M. Huyse, Y. Kudryavtsev, P. V. Duppen, Off-line test of the {KISS} gas cell (2013). doi:http://dx.doi.org/10.1016/j.nimb.2013.06.032.

[94] N. Fukunishi, M. Kase, Y. Yano, Design study on beam transport system from irc to rarf, RIKEN Accel. Prog. Rep. 35 (2002) 283.

[95] E. M. Burbidge, G. R. Burbidge, W. A. Fowler, F. Hoyle, Synthesis of the elements in stars, Rev. Mod. Phys. 29 (1957) 547.

[96] M. Arnould, S. Goriely, K. Takahashi, The r-process of stellar nucleosynthesis: Astrophysics and nuclear physics achievements and mysteries, Physics Reports 450 (2007) 97.